学位論文

Non-equilibrium tidal heating of Enceladus and compositional diapirism of Ceres, their roles in exoplanets

(エンセラダスの非平衡状態の潮汐加熱とケレスの組成プルーム、および系外惑星におけるそれらの役割について)

平成２６年１２月博士　(理学)　申請

東京大学大学院理学系研究科
地球惑星科学専攻
庄司　大悟

Abstract

Endogenic activities on the Earth such as plate tectonics and volcanic eruptions largely affect our environment. In our solar system, except for the Earth, Io and Enceladus have been recognized to have endogenic activity. In addition, some bodies such as Triton and Ceres exhibit vaporization, which may be induced by their endogenic process. Out of our solar system, there should be many active planets. Although analysis of their activity is important in planetary science and understanding our environment, detailed activity mechanism in each body is not known well. In this work, I focus such activities on Enceladus, Ceres and extrasolar rocky planets.

From the surface of Enceladus, plumes mainly composed of water vapor and ice grain emanate into the space, which implies a subsurface ocean in Enceladus. However, the mechanism that maintains liquid water in Enceladus remains unsolved enigma because conventional radiogenic and tidal heating processes cannot maintain the ocean for a long time if Enceladus has equilibrium orbital state. From the surface state, Enceladus has large probability that heating is not in steady state. I considered the interaction of tidal heating with interior structure and orbital evolutions. Although depending on the rheological parameters, the interior ocean can be maintained by the oscillatory variation of ice thickness and eccentricity if melting temperature decreases and core radius is less than 161 km. Our calculation results show that ocean thickness is no more than a few kilometers and that interior temperature has to be lower than 175 K, which is smaller than the estimated values by gravity and thermal measurements. Heat generated by chemical process may be an additional heat sources in order to keep Enceladus warm, which can be a future study to be considered.

At the dwarf planet in asteroid belt Ceres, it has been observed that water vapor emanated from the surface. Although vaporization of Ceres is not continuous emission,

which is different from the plume of Enceladus, endogenic activity is suspected for the origin of the vaporization in Ceres. While Enceladus has tidal heating, Ceres does not have strong tide due to the large distance from the Sun. As for the origin of Ceres ' vaporization, I suggest the compositional diapirism in which less dense pure ice goes up to the surface by the buoyancy through dense rock-ice crust. If the curst density is around 2700 kg m^{-3} and temperature is less than 180 K, the crust is maintained for a few billion years. Surface temperature is estimated for 180 K at the equatorial region, and thus all the crust should have sunk to the interior. However, at the mid-latitude and the polar areas, surface temperature is less than 180 K. Thus, the crust may be maintained, and diapirism can be induced. By the numerical calculations, I found that induced diapir could appear at the surface within the solar system age if the surface temperature is around 170 K. On the other hand, if the surface temperature is 150 K, diapir cannot reach the surface because of high viscosity near the surface regioin. Observation showed that vaporization of Ceres came from mid-latitude of Ceres. The localization of vaporization results from the moderate temperature enough to induce diapir and transfer the pure ice to the surface.

Enceladus and Ceres are the celestial bodies in our solar system. In the following section, extrasolar terrestrial planets are considered. One important topic for exoplanets is searching for habitable planets out of the solar system. Recently, special attentions have been paid for exoplanets around M type stars as observational targets because a lot of M stars exist. Due to low temperature, habitable zone of M star is near the central star, which results in the large effect of tide. In this work, applying the Enceladus research, I conduct numerical calculations for tidal evolution of Martian-sized planets around M stars. By thermal-orbital coupled calculations, planets which orbit in the habitable zone of M stars can stay their habitable zone even though eccentricity is large. This is because the mantle melts by tidal heating and the magnitude of dissipation decreases, which results in the

small orbital change. If the initial eccentricity is more than 0.2 and central star mass is less than 0.2 times of the solar mass, heat flux by tidal heating is suitable for habitability.

Although the distance from the central star is an important factor for the habitability of the planets, endogenic activity also plays an important role in habitability because interior activity largely affects the surface environment. As a next step, I consider the delamination process in super-Earths. Extrapolating the Earth model, magnitude of delamination is estimated at heavy rocky planets. In the model used in this work, Rayleigh number decreases with increasing the mass of the planets due to high pressure. Thus, the magnitude of the delamination process decreases at large planets even though it occurs. Delamination process depends on the local convection in asthenosphere, which is affected by the modeling condition. In addition, interior structure of terrestrial planet is not always the same to the structure of the Earth. More work is needed for more detailed study of delamination process in super-Earth.

Contents

1 Introduction

1.1 Active solid bodies in our solar system

Of many solid celestial bodies in our solar system, only six bodies (the Earth, Io, Enceladus, Triton, Ceres and Europa) are observed to have endogenic current activity. The Earth, Io and Enceladus have been proved that their activity is endogenic. Many earthquakes and volcanic eruptions occur in the Earth, which is induced by plate tectonics and interior convection. Io also has many volcanos which erupt sulfur and silicate (e.g., McEwen et al., 2000). Volcanic eruptions of Io are caused by the tidal heating (Segatz et al., 1988). On the Saturnian icy satellite, Enceladus, plumes mainly composed of water vapor and ice emanate from the surface (e.g., Porco et al., 2006). Although detailed mechanism is not known well, the plume emissions are considered to be generated by boiling of the interior liquid water (Postberg et al., 2009, 2011; Spencer and Nimmo, 2013).

In addition to these three bodies, although they are not proved so far, Triton, Ceres and Europa may have endogenic activity. It is observed that Triton has cryovolcanism (e.g., Soderblom et al., 1990). As for the origin, two ideas are suggested. One is the insolate heating, in which surface nitrogen is sublimated by the heat of the Sun (Brown et al., 1990). The other heat source is the tidal heating (e.g., Gaeman et al., 2012). Recently, water vapor emissions are observed for Ceres (Küppers et al., 2014) and Europa (Roth et al., 2014). By the lack of detailed observational constraints, we cannot completely say that their vaporizations are endogenic. However, it is probable that endogenic mechanism induces the vaporizations, and thus Ceres and Europa are current active bodies along with Io and Enceladus. Especially, many researches indicate that Europa has a subsurface ocean (e.g., Kivelson et al., 2000). Although current activities are not observed, Titan and Charon have the traits of cryovolcanism (Sotin et al., 2005; Lopes et al., 2007; Cook et al., 2007). In the future, they may be recognized as the current active satellites.

Endogenic activity is completely different from exogenic event because endogenic activity is the ”self-producing” event. Self-producing activity is interesting because non-living objects (satellites and planets) induce their activity spontaneously. In addition to the physical process, endogenic activity attracts us for the consideration of environment suitable for lives (habitability). Habitability is not a simple word, and contains complicated meanings from the aspect of biology, chemistry and physics. However, many researchers think that liquid water plays an important role. Moreover, liquid should be maintained relatively for a long time. In other words, longevity as well as existence of liquid water also affects the habitability. Some active bodies should have stabilized water as a ocean. Thus, research of activity mechanism contributes to understanding of habitability.

1.2 Outside the solar system

Since the first planet is discovered out of our solar system (Mayor and Queloz, 1995), many observations have been conducted to resolve the planetary system comprehensively. Due to many efforts, it has been proved that many rocky planets also exist outside of the solar system (e.g., Léger et al., 2011), which means that there should be Earth-like (with surface ocean, moderate temperature and even lives) planets in other planetary system. Of course, extrasolar planet is interesting and important topic for itself because some planets have environment which cannot be seen in our solar system. Comprehensive history (formation and evolution) of planets and planetary systems is one goal of planetary science. However, in addition to planetary science, extrasolar planets are important to consider the Earth and our environment.

For example, only the Earth has tectonic type convection so far, and the detailed mechanism for the plate tectonics is not known regardless of many researches. One problem for the plate tectonics research is that other celestial bodies do not have plate tectonics. If

interior has viscosity contrast, stagnant lid type convection is induced typically as a heat transfer (e.g. Solomatov and Moresi, 2000). For the tectonic type convection, weakening of surface layer is required for the onset of the plate tectonics. Because other rocky planets do not show tectonics, additional factor (size? water?) should affect the weakening on the Earth. Regardless of very interesting topic for the Earth, this factor is not solved. If there were at least one other body which has plate tectonics, we could compare it to the Earth, which would drastically constrain the mechanism on the onset of tectonics. Unfortunately, we do not have comparable target in our solar system because plate tectonics exists only on the Earth (Although Europa may have tectonic activity (Kattenhorn and Prockter, 2014), it is not confirmed so far).

However, due to the extrasolar terrestrial planets, we may be able to compare the tectonic activity of the Earth with other bodies. Actually determination of the key factor for the plate tectonics has begun (e.g., Valencia et al., 2007). Of course, observation of the endogenic activity on exoplanets is not an easy task. However, progress of instrument and technic keeps going forward, which results in the detection of the trait of activities even though direct measurement is difficult. Thus, understanding of the extrasolar planets is directly related to the understanding of the Earth.

1.3 Why are current active bodies "active"?

Regardless of many effective suggestions, detailed mechanism of the current activities is not known well. In order to induce the endogenic activities, interior dynamics has to work. For example, many researches suggest that tidal heating plays an important role in icy satellites. However, it is still unresolved how and where the tidal heat is generated. In addition, Ceres does not have strong tide due to the long orbital distance from the Sun. Thus, if the Ceres' vaporization is endogenic, different mechanism works.

Although many planets and satellites have the traits of the past activity, they are inactive now. What is the difference between current active and inactive bodies. In order to answer this question, it is insufficient solely to suggest the heat sources. We need to know the system activated by the heat source, which is not simple. One example is the convection in the planets. Although convection is induced for the heat transfer to the surface, style of convection depends on interior structure and temperature distributions. Thus, even though the heat source is the same, different style of convection may occur at each celestial body.

Tidal heating is considered as the heat source of some active satellites. However, in order to generate endogenic activity, heat transfer is very important. Even though heat is generated by tidal dissipation, interior dynamics depends on the amount and time scale of heat transfer. In the case of Europa, sufficient heat is generated by tides and subsurface ocean is maintained. On the other hand, Enceladus is the annoying object. Due to the small size, the ratio of transferred heat to generated heat is larger than Europa. Thus, although many researches indicate that tidal heating maintains the ocean and plume emissions, a subsurface ocean freezes soon. Because environment generated by tidal heat can be different among these satellites, we need to analyze each satellites. Of course, tidal and orbital theory estimated for other satellites can be applied to each satellites.

One interesting exception is Ceres. Ceres does not have tidal heating process. Although it is not ruled out that Ceres' vaporization is induced by exogenic origin, Ceres' endogenic activity should be analyzed once. If Charon is currently active, Ceres can be a comparable body because Charon's eccentricity is zero and tidal heat is not induced now.

1.4 Purpose of this work

In this thesis, mainly with numerical calculations, I consider interior dynamics which can be the origin of the observed endogenic activities, and discuss the interaction between interior and the observed surface activity.

As mentioned above, each body has unique complex system for its activity. Thus we should consider individual body carefully. In Section 2, as a satellite under control of the tidal heating, I focus on Enceladus based on the work by Shoji et al. (2014). Typically, main heat sources in icy satellites are radioactive decay in the rocky material and tidal heating. However, in the case of Enceladus, the current magnitude of radiogenic heat is only 0.3 GW (Roberts and Nimmo, 2008). For the maintenance of the ocean, a few giga watt of heat is required even though melting point is lowered by the existence of impurities. Thus, effect of tidal heating is important for Enceladus. The most simple assumption on the tidal heating of Enceladus is that the current eccentricity (0.0045-0.0047) is in equilibrium state between tidal dissipation and resonance with Dione. However, contrast to Europa, tidal heat in Enceladus generated by current state is not sufficient to maintain the global ocean (Roberts and Nimmo, 2008). Global ocean freezes with in 30 Myr even though ocean exist in Enceladus. Thus, as a next step, we have to take into account the time evolution of tidal heating, which requires the interaction among heating rate, interior structure and orbit (non-steady state). Assuming the Burgers rheology model, we consider the condition for the ocean to be maintained for a long time by tidal heating and resonance. As an active body without tide, Ceres' vaporization is discussed in Section 3, which is written based on the work by Shoji and Kurita (2014 b). Due to the lack of the detailed observation, origin of the vaporization is not known. As the hypotheses, cryovolcano and comet-type sublimation are suggested by Kuppers et al. (2014), which are largely probable. As an alternative idea, considering the future probe observation by

Dawn, I suggest that diapirism by pure ice can be the source to supply fresh ice to the surface. This work can be the additional hypothesis for the origin of the vaporization of Ceres. We estimated whether undifferentiated crust cam be preserved now at the Ceres' surface considering different rock density between 2700 and 3440 kg m^{-3}. If the crust is maintained for a long time, underlying pure ice can reach the surface by buoyancy. As a next estimation, we calculate time scale for the generated diapir to reach the surface. We would like to propose estimated latitude dependence of the crustal age as one of the exploration guidelines of Dawn mission. In Section 4 and 5, based on basic theories derived from the bodies in our solar system, extrasolar planets are taken into account. In Section 4, I analyze the tidal evolution of extrasolar planet around M type star (M dwarf) based on Shoji and Kurita (2014 a). Recently, many exoplanets have been observed. One of the most interesting topics on exoplanet is searching for the habitable planet out of our solar system. Due to the large number, M type stars are expected to be attractive observation targets (Scalo et al., 2007). Although planets around M stars should be tidally locked due to the small orbital distance, moderate climate may be sustained (Joshi et al., 1997). If so, we have a lot of target stars which may have habitable planets. One important point for the habitable planets around M stars is they are strongly affected by tide. Applying the method for the tidal evolution of Enceladus, orbital and thermal evolutions of exoplanets around M stars are estimated considering their habitability (Barns et al., 2008, 2009). In this work, we assume that the size of the planet is the same to Mars, and estimated the thermal and orbital evolutions with different initial eccentricity between 0.1 and 0.5. The mass of the central star is changed from 0.1 to 0.5 times of the mass of the Earth. In Section 5, as an activity induced in relatively shallow area of the planets, delamination process in large terrestrial planets (super-Earths) is considered based on Shoji and Kurita (2015), which is the extrapolation of Rayleigh-Taylor instability theory. In addition to

the orbital distance (habitable zone), activity of the plate is very important for the habitability. Although conclusions are controversial, plate tectonics on super-Earths has been analyzed by some works (e.g., Valencia et al., 2007). Thus, in this paper, I estimate the magnitude of the delamination process at heavy solid planets. Delamination is the peeling of mantle lithosphere by localized small scale convection of asthenosphere. Like the Earth, it is valuable for exoplanet research to consider this process in addition to plate tectonics. Referencing the model by Valera et al. (2011), we estimated the delaminated area by changing the mass of the planet and the thickness of the mantle lithosphere.

After showing the detailed results on each topic, comprehensive topics and problems are discussed in Section 6. Conclusions of each topic and future studies are given in Section 7.

2 Non-equilibrium tidal heating of Enceladus

2.1 Enigma of Enceladus' activity

Enceladus is one of the most interesting and enigmatic satellites in our solar system. Despite its small radius of around 250 km, at least 4.2 GW of heat is radiated and water plumes are emanated from the south polar terrain (Porco et al., 2006; Spencer et al., 2006, 2013; Howett et al., 2011). Although the origin of the large heat flux and plume emissions is not known, many studies indicate that liquid water in Enceladus plays an important role (e.g., Postberg et al., 2009). Liquid water as a subsurface ocean is considered to exist in some icy satellites such as Europa (e.g., Kivelson et al., 2000). Thus it may be conceivable that Enceladus also has a subsurface ocean. In order to maintain the subsurface ocean, heat sources are required. For icy satellites, radiogenic and tidal dissipation are the most effective heat sources. However, in case of Enceladus, the current magnitude of radiogenic heat is around 0.3 GW (Roberts and Nimmo, 2008), which is not sufficient to maintain a subsurface ocean. Thus tidal heating is important to analyze with respect to Enceladus' activity.

Roberts and Nimmo (2008) estimate whether a global ocean can be maintained by tidal heating. Their calculation reveals that tidal heating is insufficient to maintain a global subsurface ocean at the current eccentricity. Even though a global ocean is impossible, Enceladus may have a regionally confined ocean. Enceladus shows diverse surface features (Spencer et al., 2009). Around the south polar terrain, the surface is relatively smooth and young, whereas many craters are observed around the north polar region (Porco et al., 2006). Plume emissions are concentrated at the south polar terrain. Because of this heterogeneous surface state, it has been suggested that the subsurface ocean in Enceladus may be localized (Collins and Goodman, 2007). Běhounková et al. (2012) conducted detailed calculations of tidal heating assuming that a melting zone exists only

at the southern hemisphere. By their calculation, a partial ocean is easier to freeze compared to a global ocean at the current eccentricity since heat production decreases faster than the cooling rate when the ocean is localized. However, if the eccentricity was larger in the past, they conclude that a partial ocean could have been maintained.

In a previous paper, we calculated tidal heating rates of Enceladus focusing on ice rheology (Shoji et al., 2013). In the case of Burgers rheology and assuming a conductive ice model, the generated heat is greater than the cooling rate. Thus an ocean can be maintained. However, there is an important constraint on the generated heat by tides. Meyer and Wisdom (2007) calculated the magnitude of tidal heat assuming a steady state. Currently Enceladus is locked in resonance with Dione. This resonance forces Enceladus' eccentricity. On the other hand, by dissipation of energy, tidal heating has the effect to reduce its eccentricity. Thus a steady state in which the eccentricity does not change could exist. By their calculation, around 1.1 GW of tidal heat is generated in the steady state. An important aspect of this model is that the heating rate is independent from the interior structure of Enceladus. Thus, Enceladus can generate only 1.1 GW of tidal heat in the steady state, which is smaller than the cooling rate of the ice shell (Shoji et al., 2013).

2.2 Non-equilibrium tidal heating

If current Enceladus is in steady state, it is difficult to maintain a subsurface ocean. One hypothesis to explain Enceladus' current state is that heating is not steady state implying that the eccentricity and heat production rate are changing. As Běhounková et al. (2012) suggest, larger heat could be generated if the eccentricity was greater in the past. The presence of a localized ocean may be a remnant of the large heating rate in the past. Non-steady state heating is consistent with the surface state of Enceladus. As mentioned above, the surface state is diverse and the currently active area is concentrated around the south

polar terrain. However, around the equatorial and northern regions, there are topographic depressions which may imply large heating in the past (Bland et al., 2007; Giese et al., 2008, 2010). Crater relaxations on Enceladus also imply large heating in the past (Bland et al., 2012).

In order to analyze non-steady state heating, thermal-orbital coupling is needed because the thermal and orbital states affect each other. The tidal heating rate strongly depends on eccentricity, temperature and ice thickness, and the latter are affected in turn by the heating rates. Dissipation causes the temperature in the ice to increases, which results in even further heat production. Thus, temperature and tidal heating rate can be in a state of positive feedback. However, dissipation of tidal energy also causes the eccentricity to decrease, reducing the heating rate. Moreover, the ice thickness changes with the temperature gradient of the ice, and the heat production is also affected by the ice layer thickness. If the ice layer is relatively thin, the magnitude of deformation becomes large. However, the volume of the ice in which heat is generated decreases. Because of these complex mechanisms, we have to calculate the heating rate by coupling the thermal and orbital states of Enceladus.

For the Galilean satellites and Titan, coupled calculations have been conducted (Ojakangas and Stevenson, 1986; Fischer and Spohn, 1990; Hussmann and Spohn, 2004; Tobie et al., 2005 a; Bland et al., 2009). For Enceladus, Meyer and Wisdom (2008) estimated the heating state based on a homogeneous model proposed by Ojakangas and Stevenson (1986). This simple model cannot induce episodic heating and Enceladus rapidly evolves into steady state. Zhang and Nimmo (2009) performed a detailed analysis imposing constraints on the orbit and interior structure of Enceladus locked in resonance with Dione. However, they assume that the magnitude of dissipation (k_2/Q) is constant.

In this section, we perform coupled calculations among ice thickness, temperature,

tidal heating and eccentricity using a layered structure. Enceladus is likely to be differentiated into a rocky core and an icy mantle (Schubert et al., 2007). Thus, coupled calculation with a layered structure can provide more accurate heating states of Enceladus. Based on the orbital model by Ojakangas and Stevenson (1986), we combine tidal dissipation and eccentricity of Enceladus at each time step. In this coupled calculation, we assume a Burgers rheology. The Burgers model can represent anelastic behavior by using two material parameters (transient shear modulus and viscosity). Since these parameters are less well constrained, we perform the calculations varying the parameter range analogous to Iapetus (Robuchon et al., 2010).

In this work, we assume that tidal heating is concentrated only in the icy layer. This assumption is reasonable if dissipation in the core and the ocean is much smaller than that in the ice. We assume that core is composed of dry rock whose viscosity is sufficiently higher than the ice viscosity. Frictional heating between ocean and upper/lower boundaries is also assumed to be smaller than the heating in the ice. Thermal state in the ocean and the core is assumed to be equilibrium. Diffusion of the heat in the ocean is much faster than the ice. Without the tidal heating, only heat source in the core is radiogenic heat. Time scale of the change of the radiogenic heat is much longer than the time scale of tidal heating change. Thus, equilibrium state in the core is reasonable in this work. Based on these assumptions, 0.3 GW of radiogenic heat enters the base of the ice layer.

2.3 Time evolution of each process

2.3.1 Transfer and generation of heat

The thermal state in an ice layer is affected by its heat balance. In this work, we consider a thermally conductive ice layer. It is also possible that convection occurs in the ice shell if it is thick enough. Coupled calculation by a convective model has been performed (Shoji

et al., 2012), in which a convective layer with homogeneous temperature and stagnant lid layer are assumed based on the model by Hussmann and Spohn (2004). For the scaling law between Nusselt number Nu and Rayleigh number Ra, we used the estimation by Reese et al. (1999), which is given by

$$Nu = 2.51\theta^{-1.2}Ra^{0.2} \tag{1}$$

where θ is is the Frank-Kamenetskii parameter. The heating rate by tides is calculated by the method by Roberts and Nimmo (2008). In the case of a convective ice shell, the heat loss is large compared to a conductive ice shell. If the dissipation factor (Q-value) of Saturn is on the order of a few thousand, episodic large heating might be induced although additional conditions such as slush ice with low viscosity is needed. Saturn's Q-value is not known and estimates range from a few thousand (Lainey et al., 2012) to a few tens of thousand (Meyer and Wisdom, 2007). Because a small Q-value is controversial, we consider the conventional range of Q-values in this paper, which is more than 18,000 (Meyer and Wisdom, 2007). For this range, the generated heat is much smaller than the convective heat loss, the ocean freezes rapidly, and remelting of the ice does not occur.

As a next step we analyze conductive ice shells. In addition to the conductive ice shell, we assume low melting temperatures of the ice by impurities such as ammonia. If the base of the ice layer contains ammonia, the melting temperature of the ice decreases to 176 K (Durham et al., 1993). Observations of the water plume strongly suggest the existence of ammonia in Enceladus (Waite et al., 2009).

We divide the ice mantle into 50 thin spherical shells of equal thickness. The changing rate of the ice temperature T in each shell is given by the thermal transfer equation as follows

$$\rho_i c_p \frac{\partial T(r,t)}{\partial t} = \frac{d}{dr}\left(k\frac{dT}{dr}\right) + \frac{2k}{r}\frac{dT}{dr} + \psi(r,t), \tag{2}$$

where r is the radial distance from the center of Enceladus. Although heat is transferred laterally as well, we consider only the radial heat transfer for simplicity. k is the thermal conductivity. For pure ice, the thermal conductivity depends on the ice temperature, and thus it changes with radius. In this work, we consider the ammonia content of the ice. Lorenz and Shandera (2001) observed that the thermal conductivity of water-ammonia ice is lower than that of pure ice and only slightly dependent on temperature. Thus, we use a constant value of $k = 2.0$ W m^{-1} K^{-1}. This value is consistent with the results by Lorenz and Shandera (2001). c_p is the specific heat of ice, which is given as (Hillier and Squyres, 1991)

$$c_p = 7.037T + 185 \ \ \mathrm{Jkg^{-1}K^{-1}}. \tag{3}$$

ψ is the tidal heating rate per unit volume in each shell. Tobie et al. (2005 b) derive an equation about the volumetric tidal heating rate $h(r,\theta,\phi)$, which depends on the radial distance r, colatitude θ and longitude ϕ. We calculate ψ as averaged volumetric tidal heat in each ice shell as

$$\psi(r,t) = \frac{1}{V}\int h(r,\theta,\phi)dV, \tag{4}$$

where V is the volume of each thin ice shell. The volumetric tidal heating rate $h(r,\theta,\phi)$ is determined by stress and strain at each point (Tobie et al., 2005 b; Roberts and Nimmo, 2008). Strain and stress in the spherical shell structure model are derived by the tidal potential (Kaula 1964) and radial functions (e.g., Alterman et al., 1959; Takeuchi and Saito, 1972). Tidal potential can be written as

$$\Phi = R_s^2\omega^2 e\Bigg[-\frac{3}{2}P_2^0(\cos\theta)\cos\omega t + \frac{1}{4}P_2^2(\cos\theta) \times [3\cos\omega t\cos 2\phi + 4\sin\omega t\sin 2\phi]\Bigg] \tag{5}$$

where θ and ϕ are colatitude and longitude of the Enceladus (Kaula, 1964). t is time passed from Enceladus' passing the pericenter. Sabadini and Vermeersen (2004) proposed six radial functions $y_i(r)$ (i=1$-$6) by using matrix as follows:

$$y_i = Y_{ij}C_j \tag{6}$$

where C_j is constant value. Matrix Y_{ij} can be written as

$$\begin{pmatrix} \frac{lr^{l+1}}{2(2l+3)} & r^{l-1} & 0 & \\ \frac{(l+3)r^{l+1}}{2(2l+3)(l+1)} & \frac{r^{l-1}}{l} & 0 & \\ \frac{(l\rho gr+2(l^2-l-3)\mu)r^l}{2(2l+3)} & (\rho gr+2(l-1)\mu)r^{l-2} & -\rho r^l & \\ \frac{l(l+2)\mu r^l}{(2l+3)(l+1)} & \frac{2(l-1)\mu r^{l-2}}{l} & 0 & \cdots \\ 0 & 0 & -r^l & \\ \frac{2\pi G\rho l r^{l+1}}{2l+3} & 4\pi G\rho r^{l-1} & -(2l+1)r^{l-1} & \end{pmatrix}$$

$$\begin{pmatrix} \frac{(l+1)r^{-l}}{2(2l-1)} & r^{-l-2} & 0 \\ \frac{(2-l)r^{-l}}{2l(2l-1)} & -\frac{r^{-l-2}}{l+1} & 0 \\ \frac{(l+1)\rho gr-2(l^2+3l-1)\mu}{2(2l-1)r^{l+1}} & \frac{\rho gr-2(l+2)\mu}{r^{l+3}} & -\frac{\rho}{r^{l+1}} \\ \frac{(l^2-1)\mu}{l(2l-1)r^{l+1}} & \frac{2(l+2)\mu}{(l+1)r^{l+3}} & 0 \\ 0 & 0 & -\frac{1}{r^{l+1}} \\ \frac{2\pi G\rho(l+1)}{(2l-1)r^l} & \frac{4\pi G\rho}{r^{l+2}} & 0 \end{pmatrix} \tag{7}$$

where r is radial distance from the center. ρ and μ are density and rigidity at r. g shows $4\pi G\rho r/3$. In this work, we calculate $h(r,\theta,\phi)$ using the radial functions given by Sabadini and Vermeersen (2004). This method can be applied to viscoelastic rheologies by using the corresponding principle (Biot, 1954). h can be given by

$$h = \frac{\omega}{2}[\mathrm{Im}(\tilde{\sigma}_{ij})\mathrm{Re}(\tilde{\epsilon}_{ij}) - \mathrm{Re}(\tilde{\sigma}_{ij})\mathrm{Im}(\tilde{\epsilon}_{ij})]. \tag{8}$$

At spheroidal coordinates, complex strain tensor of viscoelastic material $\tilde{\epsilon}_{ij}$ can be written (Tobie et al., 2005) as

$$
\begin{aligned}
\tilde{\epsilon}_{rr} &= \frac{\partial \tilde{y}_1}{\partial r}\tilde{\Phi} \\
\tilde{\epsilon}_{\theta\theta} &= \frac{\tilde{y}_2}{r}\frac{\partial^2 \tilde{\Phi}}{\partial \theta^2} + \frac{\tilde{y}_1}{r}\tilde{\Phi} \\
\tilde{\epsilon}_{\phi\phi} &= \frac{\tilde{y}_2}{r\sin^2\theta}\frac{\partial^2 \tilde{\Phi}}{\partial \phi^2} + \frac{\tilde{y}_1}{r}\tilde{\Phi} + \cot\theta\frac{\tilde{y}_2}{r}\frac{\partial \tilde{\Phi}}{\partial \theta} \\
\tilde{\epsilon}_{r\theta} &= \frac{\tilde{y}_4}{\tilde{\mu}}\frac{\partial \tilde{\Phi}}{\partial \theta} \\
\tilde{\epsilon}_{r\phi} &= \frac{\tilde{y}_4}{\tilde{\mu}}\frac{1}{\sin\theta}\frac{\partial \tilde{\Phi}}{\partial \phi} \\
\tilde{\epsilon}_{\theta\phi} &= \frac{2\tilde{y}_2}{r\sin\theta}\frac{\partial^2 \tilde{\Phi}}{\partial \theta \partial \phi} - \frac{\tilde{y}_2\cot\theta}{r\sin\theta}\frac{\partial \tilde{\Phi}}{\partial \phi}.
\end{aligned}
\tag{9}
$$

Stress can be calculated from the corresponding principle. The reason why ψ is a function of time t is that $h(r, \theta, \phi)$ depends on the ice layer thickness, temperature distribution and eccentricity, and all of them change with time. The volume of each shell V also changes with ice layer thickness.

By Eqs. (2)-(4), the temperature evolution of each ice shell can be calculated. For the surface and base of the ice layer, we assume that the temperature is fixed at 80 K (Spencer et al., 2006) and 175 K (Durham et al., 1993), respectively.

2.3.2 Structure and rheology model

In the case of Enceladus, only mass and mean radius can be used to constrain the internal structure. We assume a three layered spherical structure composed of a silicate core, water and ice layers. Although a subsurface ocean in Enceladus may be localized, we assume a spherical layer. Assumed densities of the layers are summarized in Table 1. We conduct the calculations with different sizes of the core. In order to be consistent with the mean density of Enceladus (Porco et al., 2006) and the estimation by Schubert et al. (2007), we

consider a core radius between 155 km and 165 km.

Table 1: Rheological parameters of each layer.

layer	density (kg/m^3)	shear modulus (GPa)	viscosity (Pa s)
core	3500	50	10^{20}
ocean	1000	0.4	10^6
ice	960	3.3	

The time rate of change of the ice layer thickness D is calculated by a heat balance equation at the bottom of the ice (Gaeman et al., 2012) as

$$\rho_i L \frac{dD}{dt} = -k \left(\frac{\partial T}{\partial r} \right)_{r=R_e-D} - \frac{Q_{rad}}{4\pi (R_e - D)^2}, \tag{10}$$

where L = 132 kJ kg^{-1} is the latent heat of ice (Chan and Giauque, 1964). R_e = 252.1 km is the mean radius of Enceladus. Q_{rad} is the radiogenic heating rate. The first term shows the heat transferred to the surface while the second term is the heat which enters from the base of the ice layer. Radiogenic heat changes slowly with time. However, in this work, we consider the recent evolution of Enceladus. Thus, we use the current magnitude of heat of Q_{rad} = 0.3 GW (Roberts and Nimmo, 2008). The number of layers is constant at 50. The thickness of each layer changes with the thickness of the entire ice mantle. In our structure model, the entire ice mantle is less than 100 km thick. Thus, the thickness of each ice layer is less than 2 km at every condition.

The rheology of the ice has a large effect on tidal heating. Conventionally, the Maxwell body has been widely used for tidal heating calculations (e.g., Tobie et al., 2005 b). One deficit of the Maxwell body is that it cannot show the anelastic behavior of ice. As well as the viscoelastic response, ice has an anelastic response caused by transient creep (McCarthy and Castillo-Rogez, 2013). The effect of an anelastic response becomes large for low temperatures and large viscosities. In the case of Enceladus' ice, the Maxwell model is insufficient as a rheology for viscosities greater than 4×10^{14} Pa s (Rambaux et al.,

2010). Because we take into account a low melting temperature of the ice, the viscosity is much larger than that critical value. Thus, rheologies which include also the anelastic response are required. Recently, in order to consider the anelasticity, Burgers and Andrade bodies were suggested as rheologies for ice (Robuchon et al., 2010; Castillo-Rogez et al., 2011). In this paper, we use the Burgers model as the ice rheology. Shoji et al. (2013) have calculated the tidal heating rate assuming three rheology models (Maxwell, Burgers and Andrade models). The Burgers body can generate relatively large heat in some parameter ranges compared with the other rheology models (Shoji et al., 2013).

The Burgers body combines two rheology models, the Kelvin-Voigt and the Maxwell models (Fig. 1).

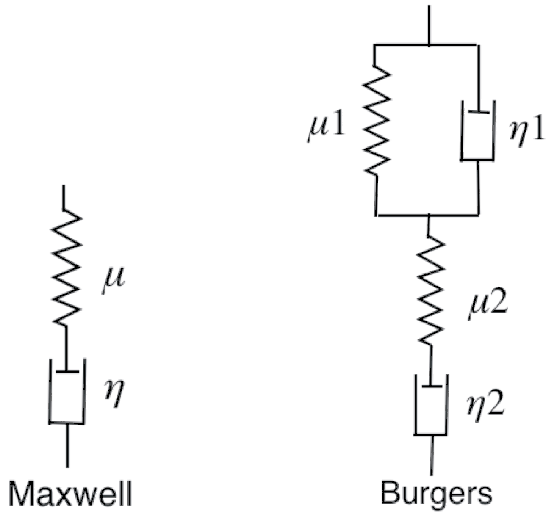

Figure 1: Two rheology models, Maxwell and Burgers bodies. The maxwell model is a typical rheology model. The Burgers model can show the effect of transient creep. In the case of high viscosity material, Maxwell time becomes large, and thus Maxwell model cannot fit the response of the material.

Both Kelvin-Voigt and Maxwell units contain shear modulus and viscosity as material parameters. Thus four parameters need to be determined for the Burgers body. Shear modulus and viscosity of the Kelvin-Voigt unit (defined as μ_1 and η_1, respectively) represent the transient creep caused mainly by the anelastic behavior. On the other hand, shear modulus and viscosity of the Maxwell unit (μ_2 and η_2) show the steady state (long term) creep. By connecting the transient creep (Kelvin-Voigt) unit and the steady state (Maxwell) unit, the Burgers body can represent viscoelastic and anelastic responses. As for the shear modulus of the Maxwell unit μ_2 (long term shear modulus), we assume a constant value of 3.3 GPa, which is consistent with the value of ice-I. Although the strain rate of the ammonia content ice depends on stress (e.g., Durham et al., 1993), we consider the effective viscosity for simplicity. The effective viscosity of the Maxwell unit η_2 (long term viscosity) is calculated using the Arrhenius function (Arakawa and Maeno, 1994) by

$$\eta_2 = \eta_0 \exp\left(\frac{E_a}{RT_m}\left(\frac{T_m}{T} - 1\right)\right), \tag{11}$$

where $\eta_0 = 10^{17}$ Pa s and T_m = 176 K are the reference viscosity and melting point of the ice, respectively. These values are consistent with water-ammonia ice below the melting point (Durham et al., 1993). E_a is the activation energy of ice, which changes with the concentration of ammonia in the ice. For a large amount of ammonia, E_a becomes around 35 kJ mol^{-1} (Kargel et al., 1991), which is smaller than the typical value of pure water ice (around 60 kJ mol^{-1}). R is the gas constant. The temperature of each ice shell T can be calculated by Eq. (2). Transient shear modulus μ_1 and viscosity η_1 are not known. Robuchon et al. (2010) assume equal transient and long-term shear moduli (μ_1=μ_2), which is consistent with terrestrial glacier ice (Reeh et al., 2003). In the case of transient viscosity, these authors use a wide range of viscosity ratios (η_2/η_1) and analyze the evolution of Iapetus. In their calculation, a wide range of viscosity ratios up to 10^8

is taken into account. They found that a viscosity ratio greater than 50 was required to reduce Iapetus' spinning rate sufficiently. In this work, we follow the approach of Robuchon et al. (2010) by using a wide range of viscosity ratios to analyze the thermal state of Enceladus. In addition, we change the shear modulus ratio (μ_2/μ_1) up to a value of 50 because it is not ruled out that μ_1 and μ_2 are different for Enceladus' ice.

In the case of the core we use the Maxwell model with shear modulus and viscosity shown in Table 1. Anelasticity may be important for the core as well. However, the effect of core rheology is beyond the scope of this study. For the ocean, we approximate liquid water by the Maxwell body with low viscosity so that the Maxwell time is much smaller than the orbital period of Enceladus (Roberts and Nimmo, 2008).

2.3.3 Orbital change

The current eccentricity of Enceladus is forced by the resonance with Dione. Běhounková et al. (2012) give a time rate of change of eccentricity based on the calculation by Ojakangas and Stevenson (1986) as

$$\frac{de}{dt} = \left[\frac{0.49 M_s c_e}{M_d \alpha C_a}\right] e^2 (1 - 30.69 D_e e^2), \tag{12}$$

where M_s and M_d are the masses of Saturn and Dione, respectively. The first and second terms show the effete of resonance and dissipation, respectively. If the eccentricity equals $1/\sqrt{30.69 D_e}$, the eccentricity does not change, and thus Enceladus becomes steady state. D_e shows the ratio of the dissipation in Enceladus to the dissipation in Saturn. Eccentricity changes in order to reach the equilibrium state by dissipation and resonance. This equation ignores the change of mean motion. The evolution of the mean motion is slow compared with eccentricity. Because we consider relatively recent evolution of Enceladus, this approximated equation is used for simplicity. α is the ratio between the semi-major

axis of Enceladus a_e and Dione a_d ($\alpha = a_e/a_d$). C_a=1.19 is a constant value applicable to the 2:1 mean motion resonance. Eq. (12) is derived by the forced eccentricity caused by 2:1 resonance, which is given by

$$e = \frac{M_d \alpha C_a n_e}{M_s \nu_{11}} \tag{13}$$

where $\nu_{11} = n_e - 2n_d + \dot{\bar{\omega}}$. n_e, n_d and $\dot{\bar{\omega}}$ are mean motion of Enceladus, Dione and secular rate of change of Enceladus' argument of pericenter (Ojakangas and Stevenson, 1986). Běhounková et al. (2012) calculate that $\dot{\nu_{11}} = 0.49 c_e n_e (1 - 30.69 D_e e^2)$.

Orbital distance also changes by the resonance with Dione. The ration of the change of orbital distance $\delta a/a$ is given by (Murray and Dermott, 1999)

$$\frac{\delta a}{a} = \left(\frac{16}{3} \frac{M_d}{M_s} |\alpha f_d(\alpha)| e \right)^{1/2}. \tag{14}$$

In the case of 2:1 resonance, $|\alpha f_d(\alpha)|$=0.749964 (Murray and Dermott, 1999). Thus, even though e is relatively larger at around 0.006, $\delta a/a \sim 2.15 \times 10^{-4}$. Because tidal heating rate depends on a^5, change of heating rate by the change of the orbital distance is very small (around 0.9989 times of the heating rate at the current orbital distance). Thus, changing of orbital distance by the resonance can be negligible in the case of Enceladus heating. c_e is given by

$$c_e = \frac{9}{2} \left(\frac{R_s}{a_e} \right)^5 \left(\frac{M_e}{M_s} \right) n_e \frac{k_{2s}}{Q_s}, \tag{15}$$

where R_s and M_e are radius of Saturn and mass of Enceladus, respectively. n_e is the mean motion of Enceladus and the second term is the effect of mean motion change. k_{2s} and Q_s are Love number and Q-value of Saturn, respectively. The Love number of Saturn is estimated as 0.341 (Gavrilov and Zharkov, 1977). We use this value in all calculations. One large uncertainty is the Q-value of Saturn. The value of Q_s is controversial and is

not well constrained. In our calculation, we take into account Q_s greater than 18,000. This minimum value is consistent with the estimation by Meyer and Wisdom (2007). As mentioned in Section 2.3.1, a smaller value of Q_s is also suggested (Lainey et al., 2012). However, we do not consider this range in this work. D_e is the ratio of dissipation between Enceladus and Saturn, which is given by

$$D_e = \left(\frac{R_e}{R_s}\right)^5 \left(\frac{M_s}{M_e}\right)^2 \left(\frac{Q_s}{k_{2s}}\right) \left(\frac{k_{2e}}{Q_e}\right). \tag{16}$$

k_{2e} and Q_e are Love number and Q-value of Enceladus, respectively. In the case of a viscoelastic body, the Q-value is given by the ratio between real and imaginary part of the complex Love number as

$$Q_e = \frac{\mathrm{Re}(\tilde{k}_{2e})}{\mathrm{Im}(\tilde{k}_{2e})} \approx \frac{|\tilde{k}_{2e}|}{\mathrm{Im}(\tilde{k}_{2e})}. \tag{17}$$

Thus k_{2e}/Q_e can be replaced by Im($\tilde{k}_{2e}$). The heating rate dissipated in the entire satellite is given as

$$\dot{E} = -\frac{21}{2}\mathrm{Im}(\tilde{k}_{2e})\frac{(n_e R_e)^5}{G}e^2, \tag{18}$$

where G is the gravitational constant (Segatz et al., 1988). Most of the tidal heat is generated in the ice layer and tidal heating in the core and ocean is assumed to be negligible. Thus, $\dot{E}$ is approximated as

$$\dot{E} = \int_0^{2\pi}\int_0^{\pi}\int_{R_e-D}^{R_e} h(r,\theta,\phi) r^2 \sin\theta dr d\theta d\phi. \tag{19}$$

From Eqs. (16)-(19), the volumetric tidal heating rate $h(r,\theta,\phi)$ can be related to the eccentricity change as

$$D_e = \left(\frac{R_e}{R_s}\right)^5 \left(\frac{M_s}{M_e}\right)^2 \left(\frac{Q_s}{k_{2s}}\right) |\mathrm{Im}(\tilde{k}_{2e})| \tag{20}$$

$$\mathrm{Im}(\tilde{k}_{2e}) = -\frac{2}{21}\frac{G}{(n_e R_e)^5 e^2} \int_0^{2\pi}\int_0^{\pi}\int_{R_e-D}^{R_e} h(r,\theta,\phi) r^2 \sin\theta dr d\theta d\phi. \tag{21}$$

This time rate of change of eccentricity is an approximation valid only for short timescales. Shifts in the mean motion towards or away from the exact 2:1 resonance with Dione could alter the changing rate of the eccentricity, thereby affecting the state of internal heating. However, since we consider the recent heating state of Enceladus, the usage of a simplified orbital evolution model is justified.

2.4 Calculation procedure

Using the equations in the previous subsection, we can calculate the thermal and orbital evolution of Enceladus. First we set the temperature of the ice shell increasing linearly from 80 K at the surface to 175 K at the bottom. The ice thickness and eccentricity at the beginning of the resonance with Dione are uncertain. Therefore, we perform the calculations with different initial values. In case of the mean motion, the current value (5.308×10^{-5} rad s^{-1}) is used. Although the mean motion also changes with time, the time rate of change is extremely small. Thus the current value is reasonable for our coupled calculation. By these initial values, we can calculate the heating rate $h(r,\theta,\phi)$ by radial functions. From Eq. (4), the averaged heating rate is given in each ice shell. Using this averaged heating rate and $h(r,\theta,\phi)$, a new temperature distribution and eccentricity are obtained. By continuing this process, we can calculate evolutions of Enceladus' thermal and orbital state. The changing rates of each parameter value are calculated by a Runge-Kutta method.

2.5 Episodic heating mode

Fig. 2 shows one example of episodic heating of Enceladus as a function of time assuming Q_s = 18,000, μ_2/μ_1 = 30 and $\eta_2/\eta_1 = 6 \times 10^4$.

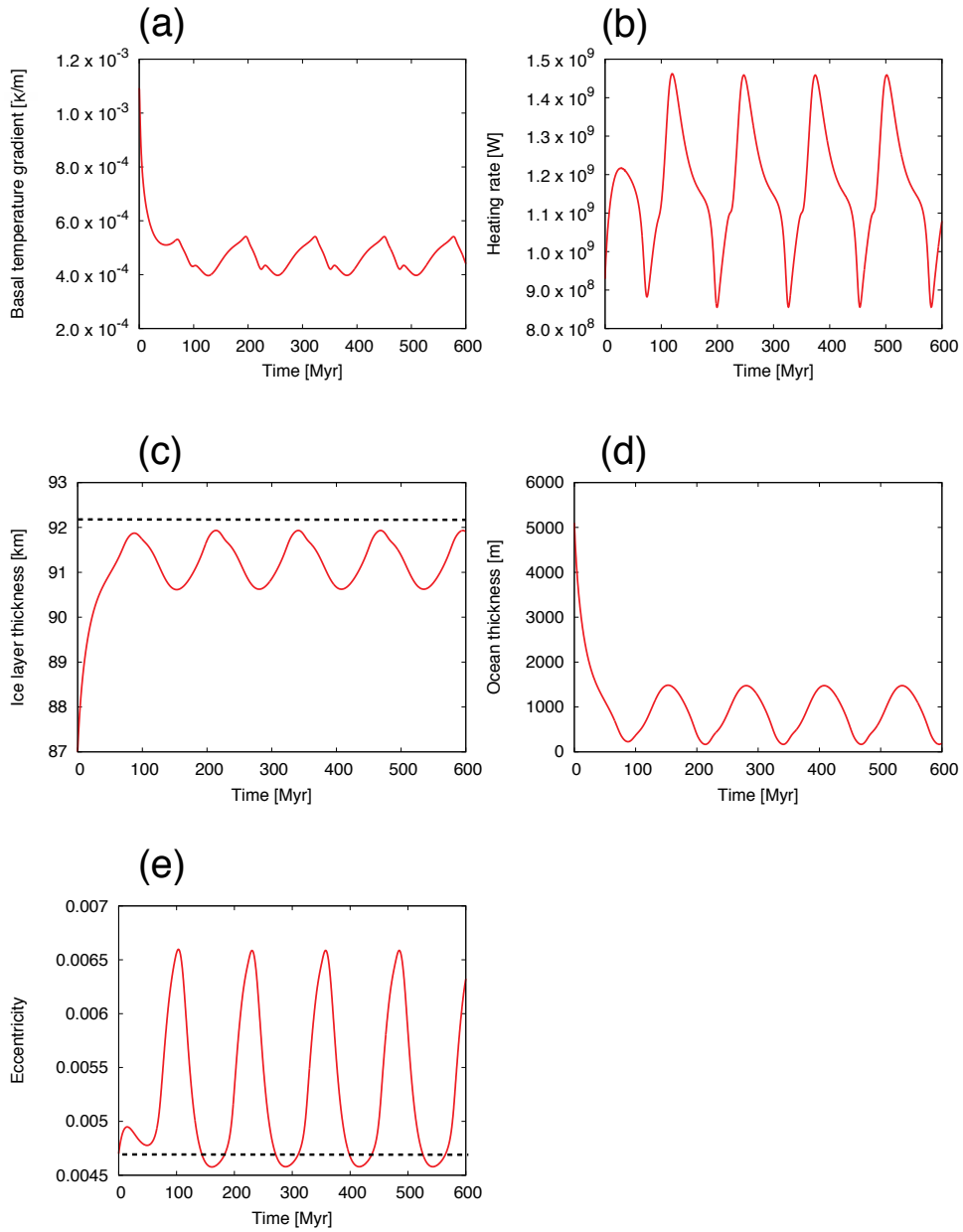

Figure 2: Evolution of (a): temperature gradient at the bottom of the ice, (b): tidal heating rate, (c): ice layer thickness, (d): ocean thickness, and (e): eccentricity assuming $\mu_2/\mu_1 = 30$, $\eta_2/\eta_1 = 6 \times 10^4$ and $Q_s = 18,000$. The radius of the core is 160 km. Initial values of the ice thickness and the eccentricity are 87 km and 0.0047, respectively. The line in (c) is the ice+ocean thickness (depth to the core). The dashed line in (e) shows the current values of the eccentricity.

We can regard the time span as the time from the beginning of the resonance with Dione until today. The radius of the core is 160 km. The tidal heating rate and eccentricity change cyclically and a heat pulse is generated at each cycle (Fig. 2 b). As initial condition, the temperature is distributed linearly and the temperature gradient is large, and thus the ice thickness increases. When the ocean freezes, the heating rate is reduced by the coupling with the core. However, the eccentricity increases rapidly until it reaches the equilibrium heating rate ($\sim$1.1 GW). Due to the large eccentricity, a relatively large amount of heat is produced and the temperature gradient decreases, which results in melting of the ice before the ocean freezes completely. If the ice mantle is decoupled from the core by an ocean, the tidal heating rate increases significantly. The heat pulse is generated by the relatively large eccentricity and decoupling of the ice from the core. This pulsed heating stops soon because the eccentricity decreases and the heating rate reaches its equilibrium value. The temperature gradient also increases and the ocean begins to freeze again. This is one cycle of the episodic heating.

The duration of one cycle of episodic heating is around 120 million years in our calculation. The generated tidal heat ranges from 0.85 GW to 1.5 GW, which is insufficient to explain the observed heat flux of several giga watt. This range of heating rate does not change much even though a broad range of rheological parameters is considered. The ice thickness oscillates from 90.5 km to 92 km (Fig. 2 c). Because the radius of Enceladus and the core radius are fixed at 252.1 km and 160 km in this calculation, the ocean thickness also oscillates between 0.1 km and 1.6 km. This result is important because Enceladus has diverse surface states. For simplicity, we use a one dimensional heat transfer model and averaged heating rates. However, tidal heating and transfer of the heat is not homogeneous (Tobie et al., 2005 b). Thus this oscillatory changes in ice thickness is consistent with a partial ocean in Enceladus. The eccentricity changes between 0.0045

and 0.0065. This range includes the current observed eccentricity (0.0047). The oscillatory changes in eccentricity allow an ocean to be maintained for a long time. The results shown in Fig. 2 are started assuming the current value of eccentricity as initial value. We conducted the calculations with different initial eccentricity or ice thickness, and confirmed that this episodic heating state is induced even for different initial values. We used a relatively low activation energy at 35 kJ mol^{-1}, which is the case for a large ammonia content in the ice. For comparison we conducted the calculations with the activation near the typical value of pure ice (around 60 kJ mol^{-1}). In that case, the minimum value of eccentricity became around 0.0055 because the viscosity increases and the heating rate is reduced. In addition, if the bottom temperature of the ice is assumed at 200 K, melting of the ice is not induced and the ocean freezes completely. For the low melting temperature and activation energy, around 30 % of ammonia concentration is required (Kargel et al., 1991; Durham et al., 1993). Early in the evolution of Enceladus, pure ice begins to freeze and impurities are concentrated at the unfrozen area. Thus, the concentration of ammonia at the bottom of the ice may be large. Ice thickness change of our calculation is less than 2 km. Due to the small ice thickness change, large concentration of ammonia is maintained. In the shallow area of the ice, low activation energy is not reasonable because ammonia concentration is relatively low. However, due to the low temperature, the shallow area of the ice is less dissipative and the effect of different activation energy is small. Thus we can expect that the heating state does not change even though depth-dependent activation energy is considered.

Oscillatory heating in which the eccentricity is consistent with the observed value is induced by the Burgers model. The Burgers model can generate relatively large heating rates at high viscosity. Heating states calculated from a Maxwell model are shown in Fig. 3.

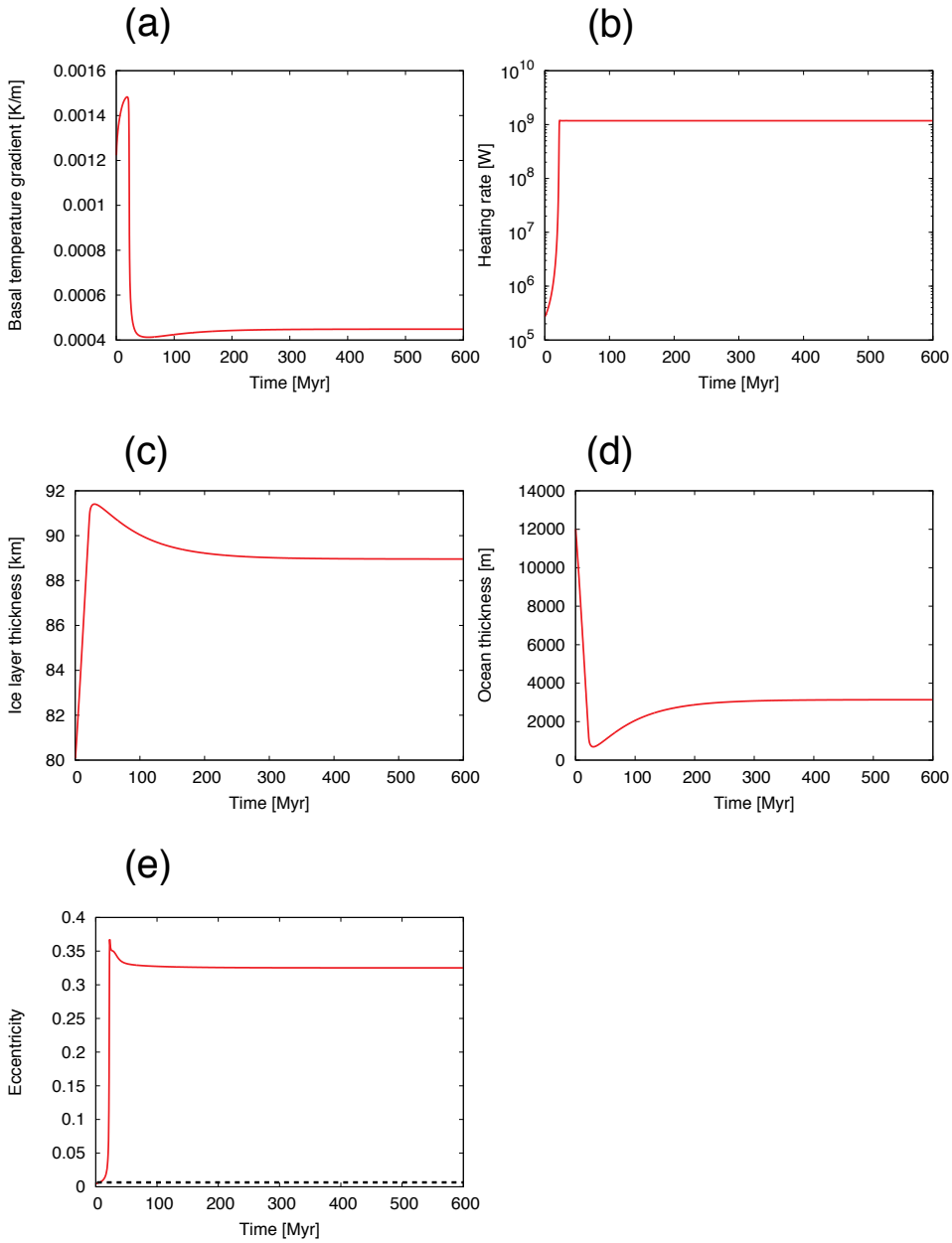

Figure 3: Evolution of (a): temperature gradient at the bottom of the ice, (b): tidal heating rate, (c): ice layer thickness, (d): ocean thickness, and (e): eccentricity of Maxwell body. $Q_s = 18,000$. The radius of the core is 160 km. Initial values of the ice thickness and the eccentricity are 80 km and 0.0047, respectively. The dashed line in (e) shows the current values of the eccentricity. By the Maxwell model, because dissipation is very low, eccentricity increases drastically in order to reach the equilibrium heating rate. Even though the ocean is maintained, this magnitude of eccentricity is largely different from the current observed eccentricity of Enceladus.

Because of the small heating rate, the eccentricity increases significantly. When the heating rate reaches its equilibrium value, a steady state is obtained. In the case of the Maxwell model, an eccentricity of 0.32 is needed for the ocean to survive, which is much larger than the observed value. Roberts and Nimmo (2008) estimated that an orbital eccentricity of at least 0.015 is needed to maintain a global ocean. This difference from our result is due to the viscosity of ice resulting in lower dissipation rates and larger eccentricities in order to sustain a subsurface ocean.

2.6 Effect of rheological parameter

Figs. 4 and 5 show results with $\eta_2/\eta_1 = 5 \times 10^4$ and 8×10^4. Other parameter sets such as Q_s and μ_2/μ_1 are the same as in Fig. 2.

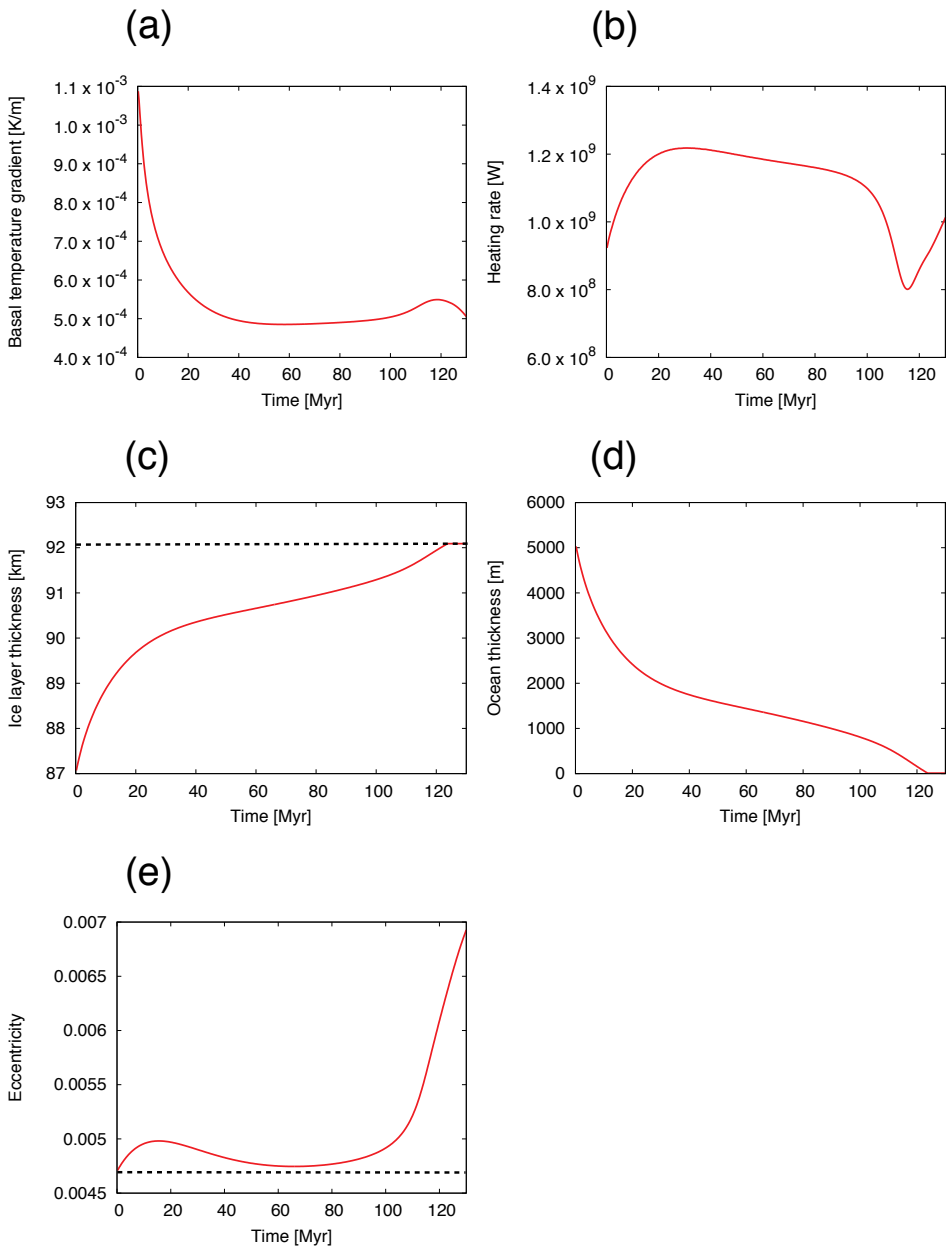

Figure 4: Evolution of (a): temperature gradient at the bottom of the ice, (b): tidal heating rate, (c): ice layer thickness, (d): ocean thickness, and (e): eccentricity assuming $\mu_2/\mu_1 = 30$, $\eta_2/\eta_1 = 5 \times 10^4$ and $Q_s = 18,000$. The radius of the core is 160 km. Initial values of the ice thickness and the eccentricity are 87 km and 0.0047, respectively. The line in (c) is the ice+ocean thickness (depth to the core). The dashed line in (e) shows the current values of the eccentricity. Calculation results are shown until the ocean freezes completely. In this parameter range, ocean cannot be maintained.

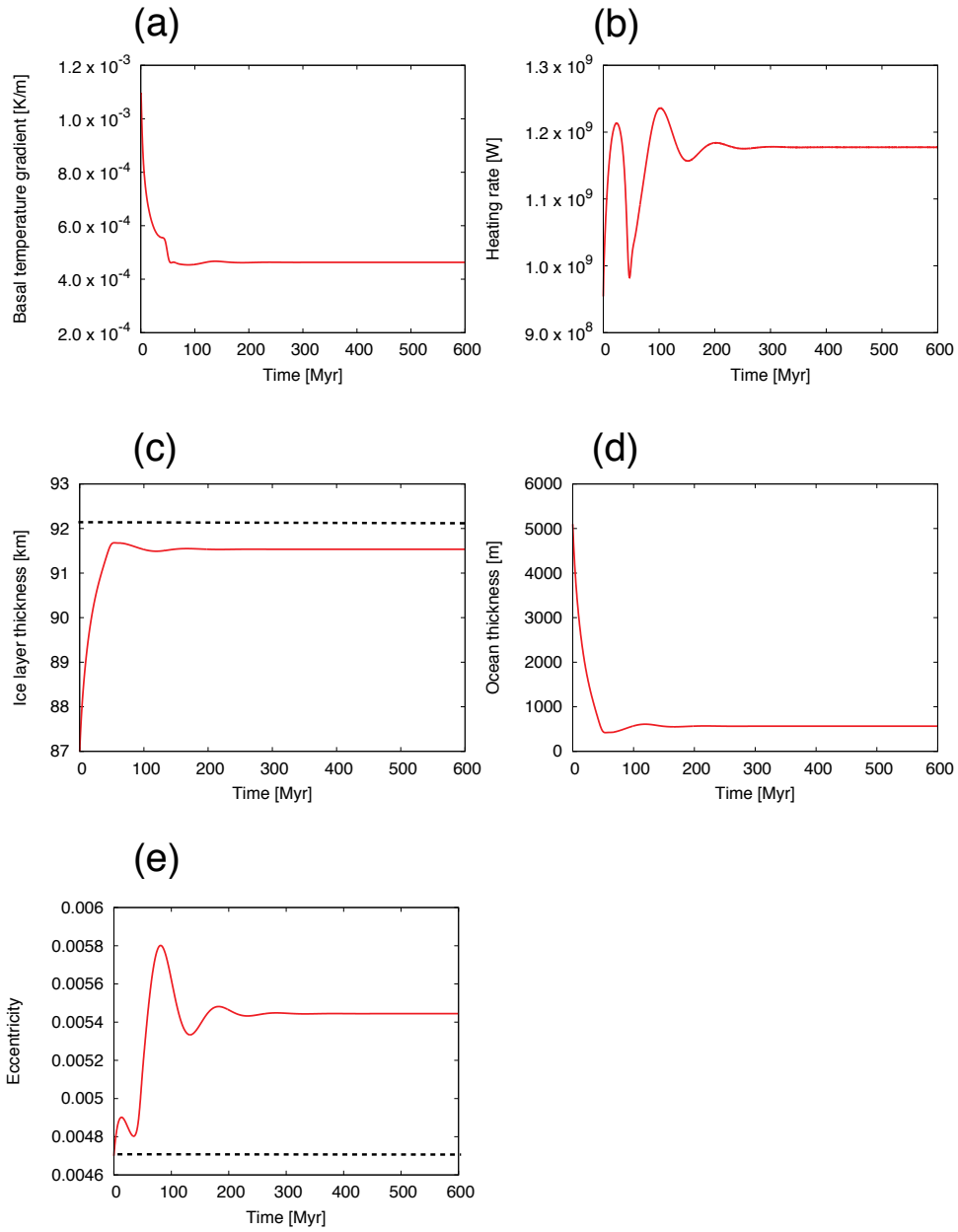

Figure 5: Evolution of (a): temperature gradient at the bottom of the ice, (b): tidal heating rate, (c): ice layer thickness, (d): ocean thickness, and (e): eccentricity assuming $\mu_2/\mu_1 = 30$, $\eta_2/\eta_1 = 8 \times 10^4$ and $Q_s = 18,000$. The radius of the core is 160 km. Initial values of the ice thickness and the eccentricity are 87 km and 0.0047, respectively. The line in (c) is the ice+ocean thickness (depth to the core). The dashed line in (e) shows the current values of the eccentricity. In this parameter values, ocean can be maintained. However, eccentricity is not consistent with the observed value.

At a viscosity ratio of 5×10^4, the ocean freezes completely. This result does not depend on the initial value of the ice thickness. For the small viscosity ratios, a large amount of heat is generated in the small viscosity range (Shoji et al., 2013). In the case of conductive ice, the temperature is high at the bottom of the ice, thus the heating is concentrated at the base of the ice layer and the temperature gradient becomes large. Because of this, the thickness increases and the ocean freezes. Fig. 5 shows the heating state at $\eta_2/\eta_1 = 8 \times 10^4$. In this case, the heating rate reaches the equilibrium value rapidly and the ice layer is stable. Although a 500 m thick ocean can be maintained, the eccentricity increases to value of around 0.0054, which is not consistent with the current value. In order to maintain the ocean achieving consistency with Enceladus' eccentricity, episodic heating is the suitable model.

Heating states with different shear modulus ratios as well as different viscosity ratios are shown in Fig. 6 (c). For a small shear moduli ratio, the ocean freezes for every viscosity ratio because sufficient heat, enough to induce remelting of the ice, cannot be generated (Shoji et al., 2013). In our calculations, a shear modulus ratio greater than 20 is needed to induce the episodic heating state.

2.7 Effect of core radius and Saturnian Q-value

The calculations shown above are conducted with Q_s=18,000 and 160 km core radius. As a next step, we analyze the heating modes for different core sizes and Q-values of Saturn. Fig. 6 shows the heating modes at Q_s=18,000 with different core radii.

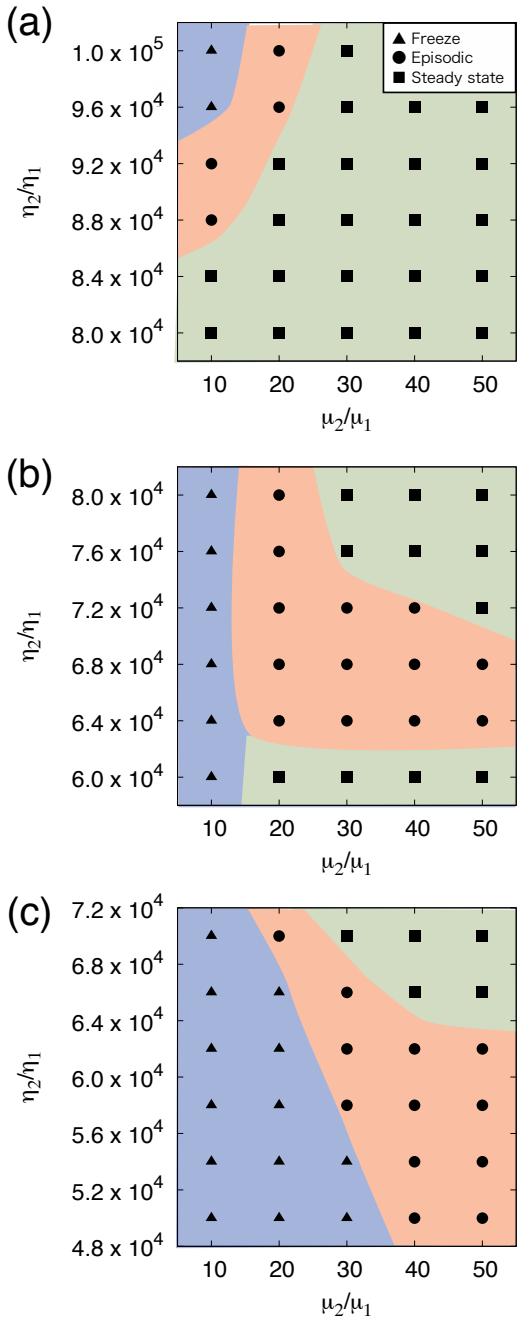

Figure 6: Possible heating states as functions of shear modulus and viscosity ratios at Q_s=18,000. Core radius is (a): 156 km, (b): 158 km, and (c): 160km, respectively. Triangle means that ocean freezes completely. Areas shown by squares are steady state, in which the ice thickness, the eccentricity and the heating rate become equilibrium values and do not change after that. When parameters are in the circle area, the episodic heating is induced.

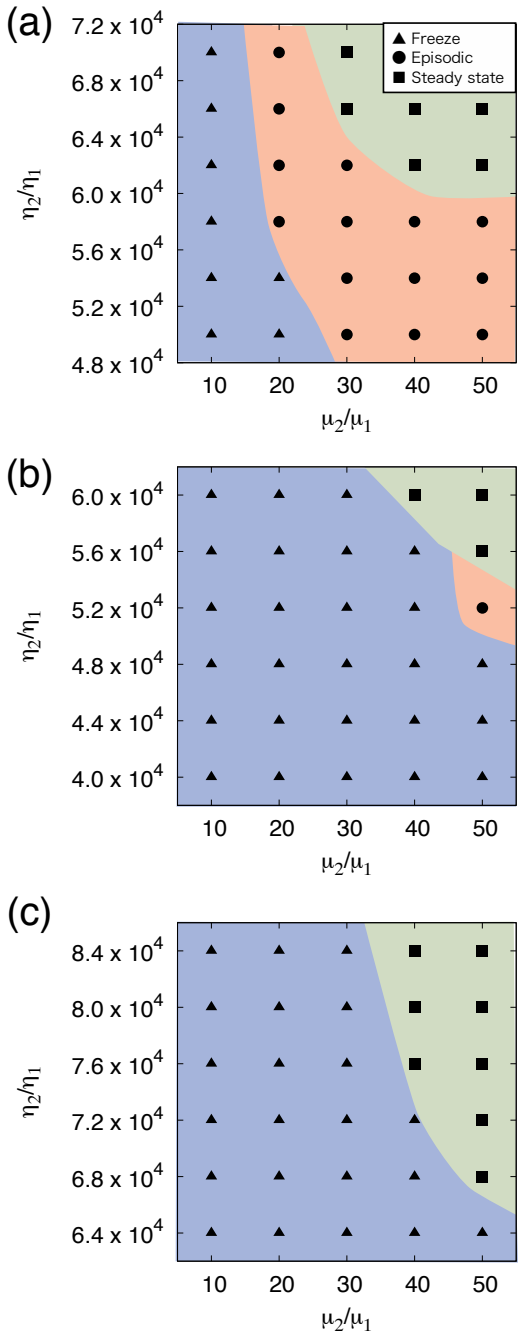

Figure 7: Possible heating states as functions of shear modulus and viscosity ratios at Q_s=20,000. Core radius is (a): 156 km, (b): 158 km, and (c): 160km, respectively. Triangle means that ocean freezes completely. Areas shown by squares are steady state, in which the ice thickness, the eccentricity and the heating rate become equilibrium values and do not change after that. When parameters are in the circle area, the episodic heating is induced.

With increasing core radius, the viscosity ratio for the episodic heating mode decreases. In the case of a large core, the ice mantle thickness decreases compared to the small core, and thus the temperature gradient increases. Because of this, heating is expected to be concentrated deep within the ice layer. In the cases of the 158 km and 156 km cores, the steady state ocean is mainly induced because the temperature gradient is relatively small and instability between cooling and heating is not induced.

Fig. 7 shows an evolution with Q_s=20,000. Compared with Q_s=18,000, the ocean is easy to freeze because the equilibrium heating rate is smaller. In the case of a 160 km core, an episodic heating state is not induced at any value of the shear modulus and viscosity ratios. If the Saturnian Q-value exceeds 20,000, cores with radii smaller than 158 km are needed to induce the episodic heating.

Whether oscillatory heating modes are possible or not depends on the Saturnian Q-value and the radius of the core because these two parameters affect the equilibrium tidal heating rate and the basal temperature gradient. In our analysis, episodic heating can occur within the gray area in Fig. 8.

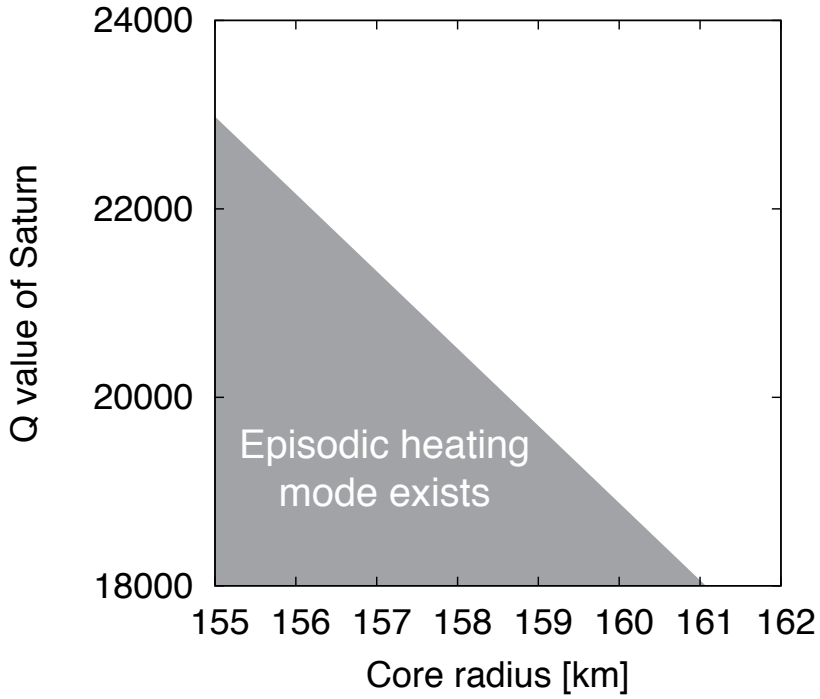

Figure 8: Ranges of core size and Saturnian Q-value where episodic heating can be induced. If rheological parameters are in proper range, episodic heating is possible in the gray area.

If the radius of the core is 155 km, Q_s<23,000 is required for episodic heating to occur. The maximum core radius for episodic heating is 161 km. In order to induce episodic heating with cores larger than 161 km, a smaller Q_s is required.

2.8 Coupling tidal heating and observed property of Enceladus

2.8.1 Large heat flux and partial ocean

The episodic heating mode generates strong oscillations in tidal heating. However, the maximum heating rates are around 1.5 GW at most for all rheological and structure parameters considered. Although Spencer et al. (2013) suggests a value of a few giga watt only, the generated tidal heat in our calculation is smaller than the observed heat flux. Thus, if Enceladus has an episodic heating mode, an additional mechanism is needed to explain the anomalous heat flux at the south polar terrain. Some models are suggested for the anomalous large heat flux. Nimmo et al. (2007) show that shear heating and re-condensation of emanated particles can generate a few giga watts of heat. Matson et al. (2012) propose water circulation in the ice mantle. Here, we propose that episodic large heat pulses may trigger additional mechanisms by sustaining enhanced "background heating".

Although the heating rate is not sufficient to explain the observed heat flux, episodic heating may explain a partial ocean and its stability. By oscillatory heating, Enceladus can have an ocean for a long time achieving the current eccentricity. Because we do not consider the lateral distribution of heat generation and transfer in this work, the ice thickness is homogeneous in our model. However, heating is not homogeneous and should affect the localized surface state and subsurface ocean. An episodic ice thickness change should cause the heterogeneity of the ocean thickness. If the position of the past ocean was different from the current position, some traits which imply large heat radiation in the

past can be explained. Enceladus has large depression areas and crater relaxations around the area where activity is not observed at present (Giese et al., 2010; Bland et al., 2012). Such regions may be related to oceans which existed in the past cycle of the episodic heating state.

One caveat of our model is that oscillatory heating rates can be produced only by the low melting temperature around 175 K. In order to attain such a low melting point, the ice layer must contain a relatively large amount of ammonia. If the melting point of ice is around 200 K, the temperature gradient is large and melting of ice does not occur, which results in complete freezing of the ocean in our model. Although ammonia molecules are detected (Waite et al., 2009), their concentration at large depth is uncertain, and would require further investigation.

2.8.2 Anelasticity of ice

Considering the orbital period of Enceladus, energy dissipation by anelasticity of the ice has a large effect when the viscosity of the ice is exceeding 4×10^{14} Pa s (Rambaux et al., 2010). In our work we consider a low melting temperature of the ice, and set the basal temperature at 175 K. At this basal temperature, the viscosity of the ice is around 10^{17} Pa s (Arakawa and Maeno, 1994). Thus an anelastic part composed of the Kelvin-Voigt unit plays an important role in the heating modes. One problem of using the Burgers model is that shear modulus and viscosity of the Kelvin-Voigt unit are not well constrained. In order to induce the episodic heating mode, the viscosity ratio of the Burgers body should be greater than 10^4 in our calculation. Considering that the long term viscosity η_2 is at least 10^{17} Pa s, the transient viscosity η_1 has to be around 10^{13} Pa s. This magnitude of viscosity is the possible range for the ice rheology. The shear modulus ratio μ_2/μ_1 should be greater than 20 for episodic heating to occur. We set the long term shear modulus at 3.3 GPa. Thus, the transient shear modulus must be on the order of 10^8 Pa. Additional

laboratory studies are needed to investigate whether the calculated parameter ranges can be attained for the ice.

We determine the viscosity of the ice by Eq. (11). However, if the bottom ice includes melt, creep becomes stronger and the viscosity drops by a few orders of magnitude (Arakawa and Maeno, 1994; De La Chapelle et al., 1999). Although we do not consider the effect of melt on the tidal dissipation in this study, large heating rates at the base of the ice layer may be caused by the effect of the melt. The magnitude of transient viscosity of $10^{12} - 10^{13}$ Pa s is consistent with the viscosity of pure ice containing some melt. Although we cannot constrain well the transient shear modulus of Enceladus' ice, Green and Cooper (1993) observed that the transient shear modulus of glass-ceramic containing partial melt becomes a few orders of magnitude smaller than the long term shear modulus. They mention that a Kelvin-Voigt unit could represent the partial melting behavior. In their analysis, $\mu_2/\mu_1 \approx 24$ produces the suitable fit to the experimental results. Thus, taking into account the partial melt of the ice, a transient shear modulus $\sim 10^8$ Pa is a reasonable assumption. For future studies, we need to take into account the effect of liquids in the ice layer. Mechanisms for the melt production such as premelting are suggested by Běhounková et al. (2012).

2.8.3 Effect of convection

In this paper, we considered conductive ice shells because the viscosity is too large for convection to be initiated. If convection occurs in the ice shell, the magnitude of the cooling rate increases and re-melting of a frozen ice shell is not induced. Shoji et al. (2012) calculated the case of a convective ice shell assuming that the convective layer is well mixed and homogeneous temperature near the melting point. In that calculation, episodic heating is induced only when the Saturnian Q-value is in the order of a few thousand and other heat sources are included. In addition, low viscosity ice such as slush

ice is needed for the episodic heating. Thus, it may be difficult to induce episodic heating in the case of a convective ice layer.

However, we do not rule out convection of Enceladus' ice shell. Conditions for convection to occur strongly depend on the grain size of the ice (Barr and McKinnon, 2007). One possible case is that convection is localized and is not in a steady state, which is consistent with the asymmetric surface state between the northern and southern polar terrain (O'Neill and Nimmo, 2011, Showman et al., 2013). Moreover, convection and conduction may occur episodically (Mitri and Showman, 2008; Běhounková et al., 2013). This switching between convective and conductive regimes may induce episodic heating. Compositional convection is also one of the hypothesis to induce the convection (Stegman et al., 2009). The effect of convection may play an important role for the origin of the plume emissions and surface topography (Besserer et al., 2013). It would be worthwhile to consider coupling of this type of ice shell with the orbital eccentricity in future studies.

2.8.4 Reformation of the ocean after freezing

In this work, we stop calculations once the ocean freezes completely (Fig. 4). Although we do not perform numerical calculations, we can roughly estimate the heating states after the complete freezing of the ocean. Because of the complete coupling between the ice layer and rocky core, dissipation in the ice layer is reduced drastically, which results in decreasing the bottom temperature of the ice and thus further reduction of the tidal dissipation. However, because of the equilibrium heating rate, the eccentricity increases. This suggests that the eccentricity should be relatively high in the event of the steady state in which the ocean does not exist. Once the ocean disappears, tidal heating in the core may affect the heating of Enceladus because the dissipation in the ice is reduced. In that case, the ice may melt by the bottom heating. In order to estimate these heating states in the future work, we need to calculate the whole thermal balance.

2.9 New observational facts

After the research by Shoji et al. (2014), some new observational facts on Enceladus have been revealed by some works. Although maintenance of the ocean is still a large problem for Enceladus, we discuss the relationship between the observed facts and our work.

2.9.1 Gravity

One major progress for Enceladus' research is that gravity measurement has been published by Iess et al. (2014). By their analysis, the moment inertia factor (MoI) of Enceladus is 0.335-0.336. This value is consistent with the structure of 60 km thick H_2O mantle and 2.4 kg m^{-3} density rock core (Iess et al., 2014). Assuming the Airy isostasy, compensation occurs in 30-40 km in depth, which can be the ice thickness in global scale. Although global ocean cannot be ruled out solely by gravity measurement, Iess et al. (2014) indicate that liquid water is concentrated around the south polar region, which is consistent with other model such as topography as well as gravity measurement. Thus, so far, the most compatible interior model of Enceladus has 30-40 km ice mantle with nearly 10 km thick ocean around the south polar region (Iess et al., 2014).

Regional sea in Enceladus has been suggested by some works (e.g., Collins and Goodman, 2007). The interesting fact is that the density of the core should be smaller than conventional model and icy mantle may be only 30-40 km in thickness. In our work, the core thickness should be less than 161 km in thickness to attain the thick ice mantle. If the icy mantle is thin, large heat is transferred from the ocean to the surface, and thus a subsurface ocean is easy to freeze. If we consider only the tidal theory, heating rate increases at thin icy mantle. Thus, it seems that thin ice layer is easy to maintain the ocean. However, heating rates are constrained by equilibrium heating between dissipation and resonance with Dione. Even though large heat is produced by the thin ice layer, eccentricity decrease

rapidly and then heating rate reaches to 1.1 GW equilibrium value. Important point is the balance between transferred heat and the equilibrium heat. As a result, thick icy mantle is easy to maintain the ocean by the equilibrium heating rate.

By the thin icy mantle, maintenance of a subsurface ocean becomes more difficult with the current eccentricity. In addition, Běhounková et al. (2012) revealed that regional sea is easier to cool compared with global ocean. Gravity measurement of Enceladus implies these two problems. Thus, ocean stability problem has become chaotic now. Of course some suggestions are possible. For example, resonance with Dione began at the very recent past, and past eccentricity of Enceladus is very large enough to maintain the ocean (Běhounková et al., 2012). In the tidal heating with the resonance with Dione, heating rate reaches the equilibrium rate (about 1.1 GW). If heating rate is less than 1.1 GW, eccentricity increases until the generated heat becomes 1.1 GW. In the case of regional sea, heating rate is smaller than the global ocean. However, by the increase of eccentricity, 1.1 GW of heating may be possible. In addition, heat loss by the convection decreases at the regional sea. Thus, assuming the changing of the eccentricity, 1.1 GW heat is larger than the heat loss, which makes the sea maintained. One problem is that ocean should not freeze at the small eccentricity era. Běhounková et al. (2012) suggest that stop of convection prevents the sea from freezing. We cannot rule out non-spherical core (McKinnon 2013), which may change the heating distribution. Nimmo et al. (2014) suggest the physical libation as the effective mechanism. These works show that Enceladus' ocean can exist by the complicated process. As mentioned below, chemical process in the core also plays some roles. If conventional mechanism is insufficient for Enceladus, our work can contribute by giving the limitation for explaining the Enceladus' ocean by conventional approach because we considered the coupled calculation used at Galilean satellite (Hussmann and Spohn, 2004).

2.9.2 Plume emission

In addition to the global structure, research for plume emission has put forward. By the detailed observations, it it confirmed that magnitude of emission changes with the position of Enceladus around Saturn (Hedman et al., 2013). This fact largely implies that tiger stripes are controlled by the tidal stress. Detailed analysis by Porco et al. (2014) revealed that plume emissions are originated to deep liquid server (perhaps subsurface ocean). Liquid water goes up to the surface through the cracks connected to the ocean. Relatively high temperature around the south polar region is caused by the latent heat of the liquid within the conduit. Based on the estimation by Crawford and Stevenson (1998), Porco et al. (2014) point out that tidal stress generates cracks in the brittle ice, and liquid water is filled in the cracks. If the liquid touches the outer space directly, it becomes jets by boiling. Jet activities are correlated to the observed hot spots (Porco et al., 2014).

If plume emission is caused by a subsurface ocean, stability of the ocean becomes problem again. Effective topic for the future work must be the coupled calculation with regional sea structure model. Our structure model assumes the spherical layer for simplicity. As Běhounková et al. (2012) mention, if the past eccentricity before the resonance is sufficiently large, regional sea may be maintained. In order to prove this idea, we have to take into account the beginning of the resonance. In addition, non-spherical shell model have to be coupled to orbital model, which is extremely complicated but should be valuable if attained.

2.10 Core of Enceladus

By the recent observations, core density seems to be smaller than the conventional models, which strongly implies that Enceladus' core is not dry rock. Thus, for the future Enceladus' research, interaction of the core should be important to be considered. If

some fraction of water is contained in the core, we can estimate that viscosity of the core becomes lower than the dry rock whose viscosity is more than 10^{17} Pa s. In our work, tidal dissipation of the core is ignored because rock viscosity is too high to generate large dissipation. However, if the surface of the core has low viscosity such as mud or clay state, relatively large magnitude of tidal dissipation may be induced.

Chemical interaction between core and ocean is another topic to be analyzed. In addition to the radiogenic heat, rock core can generate some heat by serpentinization. Serpentinization affects early stage of evolution (Malamud and Prialnic, 2013; Czechowski, 2014). Although estimation by Vance et al. (2007) shows that the magnitude of serpentinization is much less than the radiogenic heat and longevity of serpentinization is short for icy satellites, Cassini observations indicate the on-going or recent past hydrothermal activities (Hsu et al., 2011; Sekine et al., 2014). Hsu et al. (2011) found that E-ring contains silica nano particles. More than 100 °C of fluid temperature is required in order to generate the silica particles (Sekine et al., 2014). Considering the stability of silica particles, hydrothermal activity should occur now or/and at least the recent past (Sekine et al., 2014). If some magnitude of serpentinization occurs in the core, 100-350 °C of temperature should be maintained at the bottom of the ocean (Postberg et al., 2014), which can be an additional heat source. In our calculation, ocean thickness becomes no more than a few kilometers, which is not consistent with the recent observations. In addition, plume emissions are maintained by relatively high temperature (Matson et al., 2007; Porco et al., 2014). Compared with low temperature, high temperature ocean is difficult to maintain because thermal gradient becomes larger. Thus, if large magnitude of the additional heat is generated by chemical process in the core, this heat can contribute largely to the stability of $\sim$10 km thick ocean. Anyway, including new observational results, thermal process in the core should be revisited for the future work.

3 Compositional diapirism of Ceres

3.1 Vaporization of Ceres

Ceres, the largest body in the asteroid belt, is an important object in planetary science because it holds information on the origin of our solar system. The bulk density of Ceres is between 2100 kg m^{-3} and 2200 kg m^{-3} (Thomas et al., 2005; Carry et al., 2008), which is much lower than that of the rocky asteroid Vesta (Russell et al., 2012). Although the internal structure and composition of Ceres are not known well, its relatively low density implies the presence of H_2O (McCord and Sotin, 2005). Spectroscopy of Ceres' surface revealed absorption at 3 μm, which may result from OH or H_2O (Lebofsky, 1978), although an ammonium saponite origin has not been ruled out (King et al., 1992). The low albedo region of Ceres is consistent with the existence of ice and/or frost (Carry et al., 2008). Fanale and Salvail [1989] estimated the stability of water, and showed that water can exist on the subsurface of Ceres, which motivated the subsequent observations of water vaporization (A'Hearn and Feldman, 1992; Rousselot et al., 2011).

The possibility that H_2O is present within Ceres is supported by recent observations of water vapor emission from the surface (Küppers et al., 2014). They indicate that comet-type sublimation of the surface ice and cryovolcanism caused by internal heat are two possible origins of the emission. Although the mechanism that caused the emission has not yet been determined, vapor emission is observed when Ceres' orbit takes it nearer the Sun (Küppers et al., 2014), which is consistent with the sublimation of ice hypothesis.

One important observation is that vapor is only emanated from the localized low albedo terrains at mid-latitude (Küppers et al., 2014), which are called Piazzi and Region A (Parker et al., 2002; Carry et al., 2008). Thus, if water vapor is induced by the above-mentioned mechanisms, we have to explain why vapor emission is not observed around the equatorial or polar regions. One explanation is that the dark regions have a higher

temperature than the surrounding terrain. However, because the surface temperature of Ceres is typically highest in the equatorial region, assuming small albedo variation, sublimation should also occur there if this hypothesis is correct. Cryovolcanism is induced by liquid rising through the brittle material due to buoyancy. However, it is unknown why a positive buoyancy would be generated only in the mid-latitude regions.

Global images for Ceres are provided by the Hubble Space Telescope (Li et al., 2006) and the Keck II telescope (Carry et al., 2008) with images having a resolution of a few tens of kilometers. Although these images are very important for constraining the surface features, this resolution is not sufficient to analyze localized morphologies in detail. It is probable that Piazzi and Region A are large impact craters, and that the low albedo may represent topographic variation or/and materials caused by the impact events. However, an endogenic origin cannot be ruled out. In addition to the two large dark spots, some low albedo regions are observed, most of them at mid-latitude, despite the greater stability of the ice being at high latitude (see Fig. 4 in Carry et al., 2008).

3.2 Analogy to Europan morphology

Due to the lack of detailed observations by probes, it is worth considering the morphology of other celestial bodies. Young and dark morphologies, which are called chaos and lenticulae, have been observed at Europa (e.g., Greeley et al., 2000), and some of them are observed in mid-latitude (Riley et al., 2000). Two different mechanisms (or a combination of the two) are suggested for the origin of the lenticulae and chaos morphologies. One is the cryovolcanic model. This involves liquid or sill-like water rising through a fracture in a relatively thin brittle ice shell and emitting volcanic-like eruptions (Collins et al., 2000; Fagents, 2003; Michaut and Manga, 2014). The other mechanism is the diapir model (Pappalardo et al., 1998; Rathbun et al., 1998; Schmidt et al., 2011). If the icy layer is

relatively thick, warm internal ice rises as a diapir, which makes the shallow subsurface ice melt. The dark spot of Ceres is around 60 km in diameter (Küppers et al., 2014). In Europa, chaos terrain of the same size, called the Mitten, has been observed (Figueredo et al., 2002). This chaos morphology is considered to be formed by diapirism (Figueredo et al., 2002).

One problem with diapirism is that the heat in the rising plume must not diffuse until it reaches the surface area, in order to maintain sufficient buoyancy. Furthermore, detailed numerical calculations revealed that it is difficult to reproduce the observed morphology through a thermal diapir mechanism (Showman and Han, 2004, 2005). In addition to thermal buoyancy, compositional buoyancy can generate a diapir (Pappalardo and Barr, 2004; Han and Showman, 2005); a compositional density difference actually generates a larger buoyancy than thermal diapirism. In addition to Europa, compositional diapirism has been suggested as the origin of the cell-like morphology of Triton (Schenk and Jackson, 1993). Some morphologies on Venus and the Earth are also considered to be generated by compositional diapirism (e.g., Hall and Kincaid, 2001; Hansen, 2003).

As for the internal structure of Ceres, two models have been suggested. One is a homogeneous structure composed of ice and rock (Zolotov, 2009). The other model is a differentiated structure model (Thomas et al., 2005; Castillo-Rogez and McCord, 2010; Castillo-Rogez, 2011). Detailed thermal calculations of Ceres show that its interior structure can be differentiated by short- and long-term radioactive decays (Castillo-Rogez and McCord, 2010). Due to the lack of precise observations, we cannot determine which structure is more likely.

Assuming that a differentiated structure is present, Ceres is mainly composed of a rocky core and an icy mantle. However, thermal calculations suggest that the surface layer is not differentiated, but is a rock-ice mixture (McCord and Sotin, 2005; Castillo-Rogez

and McCord, 2010). These thermal calculations show that the undifferentiated crust is a few tens of kilometers in thickness. Because a rock-ice mixture has a higher density than ice, this crust is gravitationally unstable and should subside due to the Rayleigh-Taylor instability. Under the condition that a high-density layer overlies the low-density layer, small perturbations at the boundary between the two layers grow until gravitational instability disappears (Chandrasekhar, 1961). Thus, the crust overlying the less-dense ice layer disappears due to Rayleigh-Taylor instability.

However, Rayleigh-Taylor instability does not always occur when gravitational instability is generated. Rubin et al. [2014] estimated the stability of the undifferentiated crust of Charon. They revealed that the occurrence of Rayleigh-Taylor instability depends on the temperature of the crust (critical temperature for Rayleigh-Taylor instability), showing that an undifferentiated crust can be maintained on the surface of the Kuiper belt objects (Rubin et al., 2014). Callisto may also have a rock-ice mixture crust (Nagel et al., 2004); however, the surface temperature of Ceres is higher than that of the Kuiper belt objects and Callisto, meaning that the undifferentiated crust should subside more easily. However, the quantitative conditions for this subsidence have not yet been determined. In addition, Ceres might have migrated inward from the Kuiper belt (McKinnon, 2008, 2012). In this case, Ceres will likely experience periods of having a colder surface due to the long distance from the Sun.

If the temperature around the surface area is less than the critical temperature, the crust is stable with respect to Rayleigh-Taylor instability, while the bottom part of the crust should subside due to the temperature being higher than the critical temperature. Thus, at the depth where the temperature equals the critical temperature, a boundary between pure ice and the overlying crust is generated. Due to the local stress and temperature variations, the boundary is not completely flat, and a perturbation composed of pure ice is induced,

by which compositional diapirism may be possible through perturbation of the pure-ice layer.

One major problem for the stability of the crust is that the crust should be destroyed by impacts. However, the albedo variations of Ceres are relatively small compared with those of other asteroids (Li et al., 2006), which indicates that resurfacing erased the surface variation or that Ceres has not experienced many impact events, in contrast to other asteroids (Rivkin et al., 2011). At present, the latter case cannot be ruled out. Thus, part of the crust may be maintained.

Of the two mechanisms discussed for Europa, cryovolcanism has also been suggested for Ceres by Küppers et al. (2014). In this section, extrapolating the hypothesis of the Europa morphology to Ceres, we consider the possibility of compositional diapirism as a formation mechanism for the dark spots and vapor emission. In addition, we analyze whether compositional diapirism can explain why the vapor emission is observed only around the mid-latitude regions.

3.3 Stability of the crust

3.3.1 Critical viscosity of the crust

For the stability of the crust, we use an equation derived by Rubin et al. (2014). In Rayleigh-Taylor instability, perturbation at the boundary between two materials grows to large amplitude. Assuming that initial amplitude of perturbation Z_0 with the layer thickness h grows to a larger amplitude in a time scale τ, this time scale can be related to Z_0 with critical viscosity η_{crit}, which is the lower boundary of the viscosity for the perturbation grow is given by

$$\left(\frac{Z_0}{h}\right)^{1-n} = (n-1)(\dot{\epsilon}\tau)\left[\frac{C_{L\Delta\rho}}{2n}\right]^n\left(\frac{L}{h}\right)\left[\frac{\Delta\rho g h}{\eta_{crit}\dot{\epsilon}}\right]^n \tag{22}$$

where $C_{L\Delta\rho} \approx 0.76$ is a dimensionless quantity depending on the geometry and rheology (Rubin et al., 2014). Over the critical viscosity, initial amplitude grows, and the grown blob separates within τ. $\dot{\epsilon}$ is strain rate. $\Delta\rho$ and g=0.27 m s^{-2} are the density difference between the crust and the pure ice, and the acceleration due to gravity on the surface of Ceres, respectively. n is the index that relates the stress σ and the strain rate $\dot{\epsilon}$ through $\dot{\epsilon} \propto \sigma^n$. L is given as

$$L = \frac{nRT_0}{E_a}\frac{T_0}{|dT/dz|}, \tag{23}$$

where R and T_0 are the gas constant and the temperature at the interface between the crust and the underlying ice, respectively. L shows the lengthscale over which viscosity varies (Rubin et al., 2014). Assuming $\dot{\epsilon} = \tau^{-1}$, the critical viscosity of the ice for the Rayleigh-Taylor instability $\eta_{\rm crit}$ is given by

$$\eta_{\rm crit} = \left[(n-1)^{1/n}\frac{C_{L\Delta\rho}}{2n}\right]\left(\frac{Z_0}{L}\right)^{(n-1)/n}\Delta\rho g L\tau, \tag{24}$$

At around 150 K, n should be 1.8 because grain boundary sliding dominates the creep of the ice (Rubin et al., 2014). As shown below, the critical temperature for the stability of the crust is not so different from 150 K. Thus, we use $n = 1.8$ in this work.The activation energy E_a= 49 kJ mol^{-1} is a reasonable value for grain boundary sliding, which dominates the creep of the ice (Rubin et al., 2014). $|dT/dz|$ is the temperature gradient across the crust with $z = 0$ at the interface. Thermal calculations by Castillo-Rogez and McCord (2010) show a temperature gradient at shallow areas. Although dependent on the model assumption, at 10 Myr from accretion, $|dT/dz|$ $\sim$2$\times$10^{-3} K m^{-1}, which is consistent with the estimation for at the early stage by Rubin et al. (2014). After that, the temperature gradient decreases to 0.6-1.0$\times$10^{-3} K m^{-1}, and becomes stable for a few billion years (Castillo-Rogez and McCord, 2010). Thus, we analyze the stability of the crust by using

two critical viscosities. One is short-term critical viscosity with $|dT/dz|$ =2×10^{-3} K m^{-1} and τ=10 Myr, which is the case for the early era of Ceres. The other is long-term critical viscosity with $|dT/dz|$ =1×10^{-3} K m^{-1} and τ=1.5 Gyr.

The undifferentiated crust is assumed to be composed of rock and ice. Due to the effect of the rock, the viscosity of the crust can be larger than that of pure ice. Using the work by Nagel et al. (2004), we can express the viscosity of the rock-ice mixture $\eta_{\rm mix}$ as

$$\eta_{\rm mix} = \frac{\eta_{\rm ice}}{f(\phi)}, \tag{25}$$

where $\eta_{\rm ice}$ is the viscosity of ice. $f(\phi)$ is the effect of the rock component as a function of the volume fraction of the rock ϕ and is given by

$$f(\phi) = \left(1 - \frac{\phi}{\phi_{\rm CPL}}\right)^{\beta}, \tag{26}$$

where β is a coefficient that ranges from 1.55 to 2.5 (Nagel et al., 2004). In this work, for simplicity, we fix the value of β at 2.0, which is the median value of the range. $\phi_{\rm CPL}$ is the rock fraction at the close-packing limit and is $\phi_{\rm CPL} = 0.74$ (Torquato et al., 2000). ϕ can be calculated as follows:

$$\phi = \frac{\rho_{cr} - \rho_i}{\rho_r - \rho_i}, \tag{27}$$

where ρ_{cr}, ρ_i and ρ_r are the densities of the crust, ice and rock, respectively. The values of these densities are not known. We use $\rho_i = 940$ kg m^{-3}, which is consistent with ice. In the case of ρ_{cr}, we assume that the crust has the same density as the mean density of Ceres. However, the bulk density is also not known to a high accuracy. In this work, we assume ρ_{cr}=2200 kg m^{-3}, which is the latest observational result of Carry et al. (2008). A large uncertainty lies in the value of ρ_r. In the case of dry rock, ρ_r is around 3500 kg

m^{-3}, which is a reasonable value for the initial density of the rock. However, Castillo-Rogez and Schmidt (2010) consider the possibility that silicate rock was hydrated prior to accretion for the parent body of Themis. If Ceres' rock has also been hydrated at accretion, it is probable that ρ_r is near the hydrated rock density. Thomas et al. (2005) consider the density of Ceres' core to be between 2700 kg m^{-3} and the density of Vesta, which was found to be 3440 kg m^{-3} by McCord and Sotin (2005). Thus, we assume two values of ρ_r, namely, 2700 kg m^{-1} and 3440 kg m^{-1}, which makes ϕ=0.72 and 0.50, respectively. We have to note that Eq. (26) may not be valid when ϕ is near $\phi_{\rm CPL}$. However, Rudman (1992) estimates that the error is small even though the volume fraction is near the CPL range. Thus, for simplicity, we use Eq. (26) as the mixture viscosity at both rock densities. Because the value of $f(\phi)$ is smaller than 1, $\eta_{\rm mix}$ is larger than $\eta_{\rm ice}$. If $\eta_{\rm mix} > \eta_{\rm crit}$, the crust will be stable. Thus, $\eta_{\rm ice}$ must be more than $f(\phi)\eta_{\rm crit}$.

3.3.2 Ice viscosity

The viscosity of ice $\eta_{\rm ice}$ is given by the stress σ and the strain rate $\dot{\epsilon}$ as

$$\eta_{\rm ice} = \frac{\sigma}{2\dot{\epsilon}}. \tag{28}$$

The strain rate of ice was analyzed by Goldsby and Kohlstedt (2001). The creep of ice can be induced by four types of flow: volume diffusion, grain boundary sliding, basal slip and dislocation creep. The strain rate can thus be given as the sum of each creep mechanism as follows (Goldsby and Kohlstedt, 2001):

$$\dot{\epsilon} = \dot{\epsilon}_{\rm diff} + \left(\frac{1}{\dot{\epsilon}_{\rm basal}} + \frac{1}{\dot{\epsilon}_{\rm gbs}} \right)^{-1} + \dot{\epsilon}_{\rm disl}. \tag{29}$$

Each component can be represented as an exponential function with different parameter values as

$$\dot{\epsilon}_i = A\frac{\sigma^n}{d^p}\exp\left(-\frac{E_a + PV}{RT}\right). \tag{30}$$

Here the subscript i denotes the type of flow. d, P, V and T are the grain size, pressure, activation volume and temperature, respectively. A, n and p are parameters that vary with flow type. The values of each parameter are shown in Rubin et al. (2014). According to the estimation of Rubin et al. (2014), the value of PV is much smaller than the activation energy. Thus, we can ignore the effect of PV.

3.3.3 Critical temperature for instability

Fig. 9 shows the critical viscosities for the ice component as a function of temperature (T_0 and T). The critical viscosities are calculated using $f(\phi)\eta_{\rm crit}$ assuming a 1 km amplitude perturbation. The ice viscosities are calculated by Eqs. (28)-(30) with all creep mechanisms assuming d=1 mm and σ=0.1 MPa and 1 MPa.

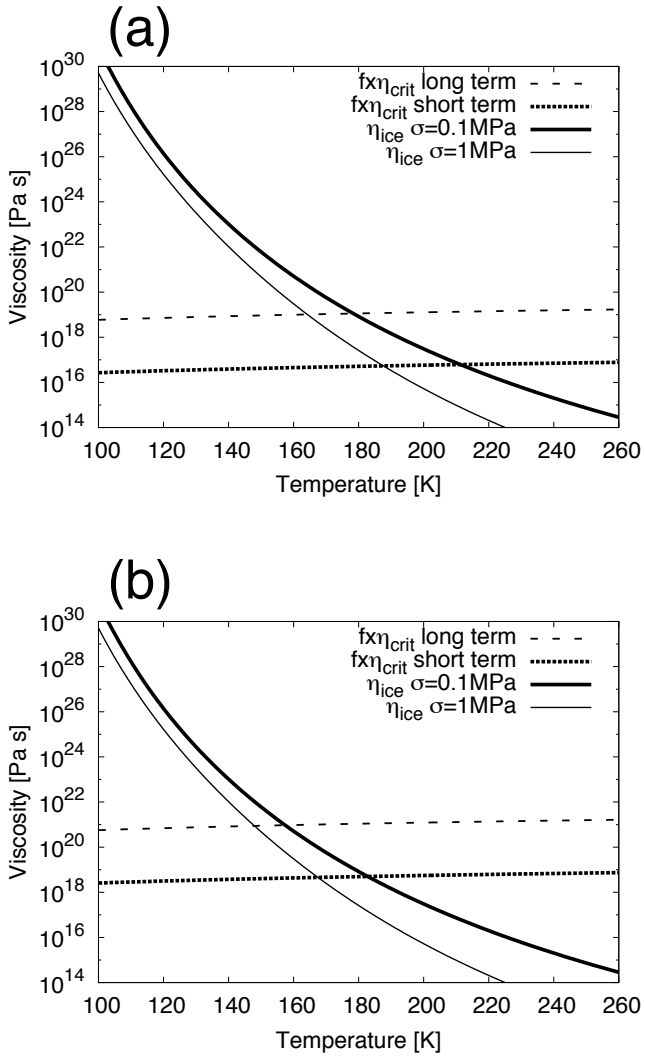

Figure 9: Ice viscosity and the critical viscosity for crust stability as a function of temperature for (a) $\rho_r = 2700$ kg m^{-3} and (b) $\rho_r = 3440$ kg m^{-3}. The thick and thin solid lines are the ice viscosities at 0.1 MPa and 1 MPa, respectively. The dotted line and dashed line are the short-term (dT/dz=2$\times$10^{-3} K/m, τ=10 Myr) and long-term (dT/dz=1$\times$10^{-3} K/m, τ=1.5 Gyr) critical viscosities, respectively, which are defined as $f(\phi)\eta_{\rm crit}$. When the ice viscosity is higher than the short-term critical viscosity, the crust is stable during the early evolution of Ceres. Long-term critical viscosity represents the stability for a few billion years.

Due to the small τ, the short-term critical viscosity is smaller than the long-term critical viscosity. When the ice viscosity is smaller than the critical viscosity, the crust is unstable and subsides due to Rayleigh-Taylor instability. The temperature at which the ice viscosity equals the critical viscosity becomes the critical temperature. By increasing ρ_r, the value of $f(\phi)$ increases due to the decrease in ϕ. Thus, the critical viscosity also increases, which results in a decrease in the critical temperature. The critical temperature changes by only a few kelvin, even though Z_0 changes from 1 km to 10 km.

Although it depends on the stress of the ice, the short-term critical temperatures is around 180 K and 200 K for ρ_r=3440 kg m^{-3} and 2700 kg m^{-3}, respectively. If the crust temperature is lower than these critical temperatures, the crust is stable during the early era of thermal evolution. The long-term critical temperature lies at around 150-160 K and 170-180 K for ρ_r=3440 kg m^{-3} and 2700 kg m^{-3}, respectively.

Although n=1.8 is a reasonable value, if another creep mechanism dominates, n changes. In addition, different values of β ought to be checked. We performed calculations using different values of n and β. In the case of n, the result changes little even though other values of n are assumed. $f(\phi)$ increases with decreasing β. Thus, critical viscosity also increases at a small β. In our calculation, if β is 1.55, which is the lower bound, the critical temperature decreases by around 10 K. However, Nagel et al. (2004) indicate that β can be 2-2.5 considering the experiment by Durham et al. (1992). Thus, we regard the critical temperatures shown above as being in a reasonable range.

Interior heat generated by radioactive decay is transferred by conduction or convection to the surface. Thus, we can presume that the temperature within Ceres is higher than the surface temperature. McCord and Sotin (2005) conducted thermal calculations assuming the surface temperature to be 200 K, while 180 K was used as the surface temperature in the work by Castillo-Rogez and McCord (2010). The surface temperature in the polar

region is lower, at around 130 K (Fanale and Salvail, 1989). Bland (2013) estimated the distribution of the surface temperature, finding the polar regions to be at about 140 K and the equator to be at 180 K. The large area at mid-latitude was around 170 K. One problem is that the surface temperature may change if the obliquity of Ceres changes greatly with time. Although an accurate obliquity variation of Ceres is not known, Nimmo and Bills (2011) estimated that the current obliquity of Ceres is 12.31°, and the obliquity oscillates with around 1° of amplitude. However, large obliquity variations are also suggested (Fuse et al., 2007). Surface temperature T_s can be calculated by

$$\begin{aligned} T_s &= \left[\frac{(1-A)F_c}{\epsilon\sigma}\frac{(i^2+\theta^2)^{1/2}}{\sqrt{2}\pi}\right]^{1/4} \quad \theta < i \\ &= \left[\frac{(1-A)F_c}{\epsilon\sigma}\frac{\sin\theta}{\pi}\right]^{1/4} \quad i < \theta < \pi - i \\ &= \left[\frac{(1-A)F_c}{\epsilon\sigma}\frac{(i^2+(\pi-\theta)^2)^{1/2}}{\sqrt{2}\pi}\right]^{1/4} \quad \theta > \pi - i, \end{aligned} \tag{31}$$

where θ and i are, respectively, the colatitude and obliquity of Ceres (Ojakangas and Stevenson, 1989; Roberts and Nimmo, 2008; Bland, 2013). $A = 0.9$, F_c =179 W m^{-2}, $\sigma = 5.67 \times 10^{-8}$ W m^{-2} K^{-4} and ϵ=0.9 are bolometric albedo, the solar flux at Ceres, the Stefan-Boltzmann constant and the emissivity, respectively (Bland, 2013). Fig. 10 shows the surface temperature as a function of colatitude with different obliquities.

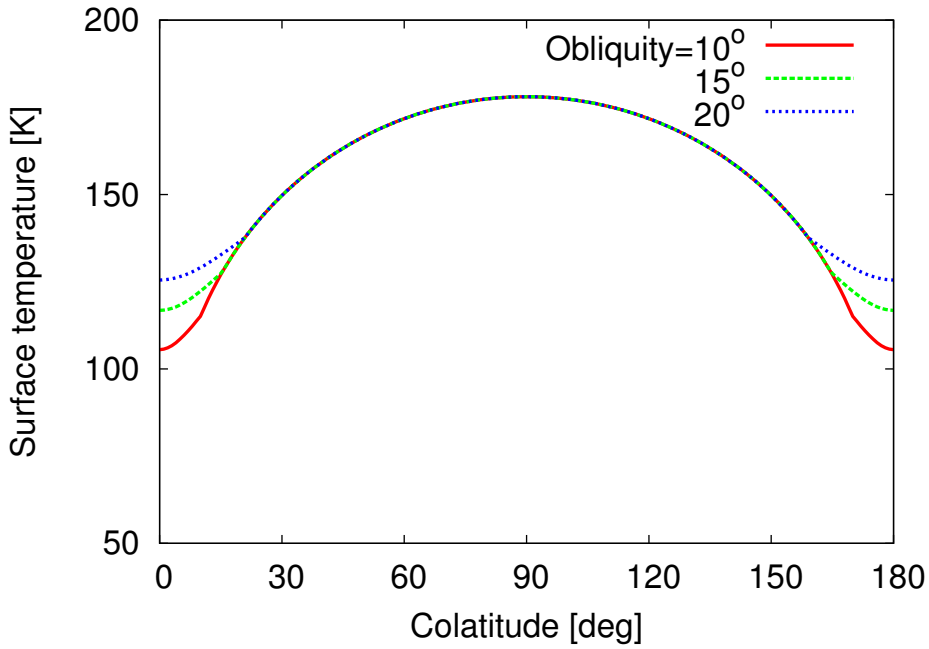

Figure 10: Surface temperature of Ceres as a function of colatitude for different obliquities. Around the equatorial region, the surface temperature is around 180 K, which is more than the preservation temperature of the crust. Thus, all crust has been subsided now around this area. However, mid- and high-latitude areas has lower surface temperature than the critical temperature for the long-term stability of the crust with low rock density. Thus, the crust may be preserved around the area if Ceres' rock density is relatively low.

Even though the obliquity is relatively large, the surface temperature around the equatorial region does not change. Although T_s changes by a few tens of kelvin in the polar regions, it is less than the 150 K. Thus, unless the time variation of the obliquity is significantly large, polar regions are cold.

While short-term critical temperature describes the stability of the crust during the early era of evolution, for diapir generation, the long-term critical temperature should be considered because it describes the stability for a few billion years. Because the surface temperature is higher than the long-term critical temperature, if ρ_r is 3440 kg m^{-3}, the crust is unlikely to be stable in the mid-latitude regions. On the other hand, in the case of ρ_r=2700 kg m^{-3}, the surface temperature is lower than both the short- and long-term critical temperatures in the mid-latitude regions. Thus, considering the temperature gradient and critical temperature for the long term, a crust more than 10 km thick may be stable for the age of the solar system. This crust can be maintained in early times by a $\sim$2 K/km temperature gradient and a short-term critical temperature of up to 210 K.

For 2700 kg m^{-3} density rock, it is necessary for silicate to be hydrated before the accretion. The model of accretion from hydrated rock is considered in the Themis thermal evolution (Castillo-Rogez and Schmidt, 2010). A future mission by Dawn will reveal whether it is probable for Ceres. In the next subsection, we perform numerical calculations of diapirism with ρ_r=2700 kg m^{-3} under the assumption that Ceres' rock is hydrated.

3.4 Compositional diapirism

3.4.1 Occurrence of compositional diapirism

Fig. 9 shows that the undifferentiated crust may be maintained in the mid-latitude regions in the case of low rock density.

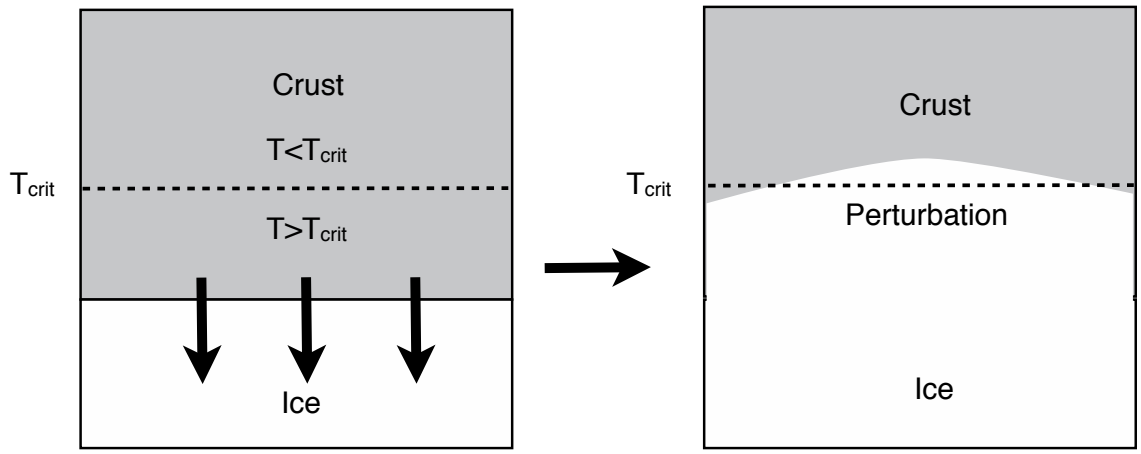

Figure 11: Schematic view of the generation of a perturbation. Through the melting and freezing of the ice, the bottom of the crust, the temperature of which is higher than the long-term critical temperature, subsides and sinks due to Rayleigh-Taylor instability. As a result of the stress and temperature variations due to the subsidence of the bottom crust, a perturbation can be generated at the interface between the crust and the pure-ice layer at the temperature of long-term $T_{\rm crit}$.

After Ceres accreted, the interior was rapidly melted by the radiogenic heat, which resulted in the differentiation in Ceres' structure. In shallow regions where the temperature is below the melting point of ice, differentiation does not occur. The generated melt begins to refreeze and a pure-ice layer is generated within 1-10 Myr (Castillo-Rogez and McCord, 2010). Subsequently, the ice layer thickens. In these processes, within the area where the crust temperature exceeds the critical temperature, the crust becomes unstable, causing some parts of the crust to sink due to Rayleigh-Taylor instability (Fig. 11). The upper part of the crust, the temperature of which is less than the long-term critical temperature, is stable on a geological time scale. When the bottom area of the crust sinks, localized stress and temperature variations are induced. Thus, it is probable that a perturbation is generated by the sinking of the bottom of the crust, which induces compositional diapirism (Fig. 11). Moreover, if the underlying pure-ice layer is sufficiently thick, convection in the ice layer may occur (McCord and Sotin, 2005), which also generates a perturbation.

Around the equatorial region, all parts of the crust subside because the surface temperature is higher than the long-term critical temperature. The perturbation required for a diapir is not induced when the crust completely disappears; thus, diapirism should not be generated in the equatorial region.

The generated diapir moves to the surface due to positive buoyancy. However, whether the diapir reaches the surface within a geological time scale depends on factors such as the temperature distribution and crustal thickness. Thus, we estimate the conditions under which the induced diapir can reach the surface of Ceres.

3.4.2 Ceres' structure model and diapirism theory

The evolution of a diapir can be modeled numerically by solving the dimensionless conservation equations for mass, momentum, energy and composition, which are given as

$$\nabla \cdot \vec{u} = 0 \tag{32}$$

$$-\nabla P + \nabla \cdot [\eta(\nabla \vec{u} + \nabla^T \vec{u})] + (\mathrm{Ra}T + \mathrm{Rc}C)\vec{e} = 0 \tag{33}$$

$$\frac{\partial T}{\partial t} + \vec{u} \cdot \nabla T = \nabla^2 T \tag{34}$$

$$\frac{\partial C}{\partial t} + \vec{u} \cdot \nabla C = 0 \tag{35}$$

where t is time, $\vec{e}$ is the vertical unit vector, $\vec{u}$ is the velocity, P is the pressure, η is the viscosity, T is the temperature and C is the composition at each point (Stegman et al., 2009). All physical values are given as dimensionless values. Ra and Rc are the thermal and compositional Rayleigh numbers, which are defined as follows:

$$\mathrm{Ra} = \frac{\alpha \rho_i g (T_b - T_s)}{\kappa \eta_b} D_{cr}^3 \tag{36}$$

$$\mathrm{Rc} = \frac{\Delta \rho g}{\kappa \eta_b} D_{cr}^3. \tag{37}$$

Here α=10^{-4} K^{-1} is the thermal expansivity and κ=10^{-6} m^2 s^{-1} is the diffusivity. T_s and T_b are the temperatures at the surface and bottom of the crust, respectively. D_{cr} is the thickness of the crust. η_b is the ice viscosity at the base with a temperature of T_b. The density dependence is included in the term RcC in Eq. (33). In the initial state, C is set to 1 and 0 in the pure ice and the crust, respectively. The evolution of C is calculated using Eq. (91), which describes the movement of the diapir.

The viscosity at each point changes as a function of the temperature and composition. Here, we calculate η by Eq. (25). The rock fraction depends on C. By the definition of the composition C, we can modify $f(\phi)$ using C as follows:

$$f(C) = \left(1 - \frac{(1-C)\phi}{\phi_{\mathrm{CPL}}}\right)^{\beta}. \tag{38}$$

This equation can be used in the case of pure ice because $f(C)$ becomes 1.0 when C=1 and $\eta_{\rm mix}$ equals $\eta_{\rm ice}$. The viscosity of ice was analyzed in detail by Goldsby and Kohlstedt (2001). However, for simplicity, we calculate the ice viscosity at each point using Arrhenius functions as follows:

$$\eta_{\rm ice} = \eta_{\rm ref} \exp\left[A\left(\frac{T_{\rm ref}}{T} - 1\right)\right], \tag{39}$$

where $\eta_{\rm ref}$ and $T_{\rm ref}$ are the reference viscosity and temperature, respectively. In this work, we set them to 10^{14} Pa s and 273 K, which is the melting point of pure ice. A is a constant coefficient that depends on the flow mechanism of the ice. In this work, we use A=20 in order to be consistent with the viscosity given by Goldsby and Kohlstedt (2001). Fig. 12 shows a comparison of the viscosities calculated by Goldsby and Kohlstedt (2001) and that obtained using the Arrhenius function with $A = 20$. All three results are fairly similar.

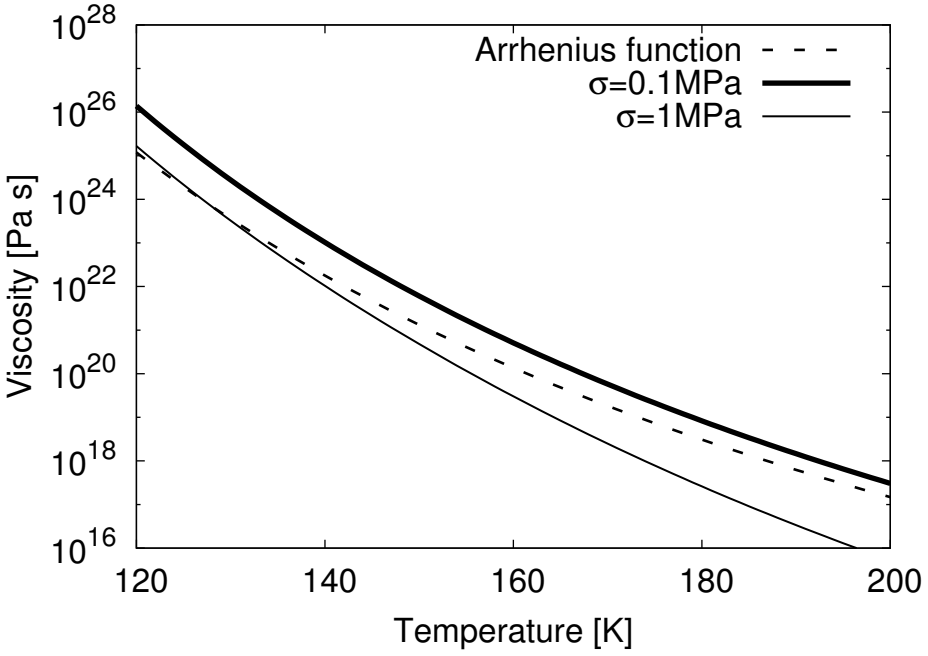

Figure 12: Solid lines are the ice viscosities from the work by Goldsby and Kohlstedt (2001) for different stresses. The dashed line is the viscosity calculated using Eq. (39) with A=20. This value of A generates moderate viscosity, which is not different largely from the viscosity by Goldsby and Kohlstedt (2001)

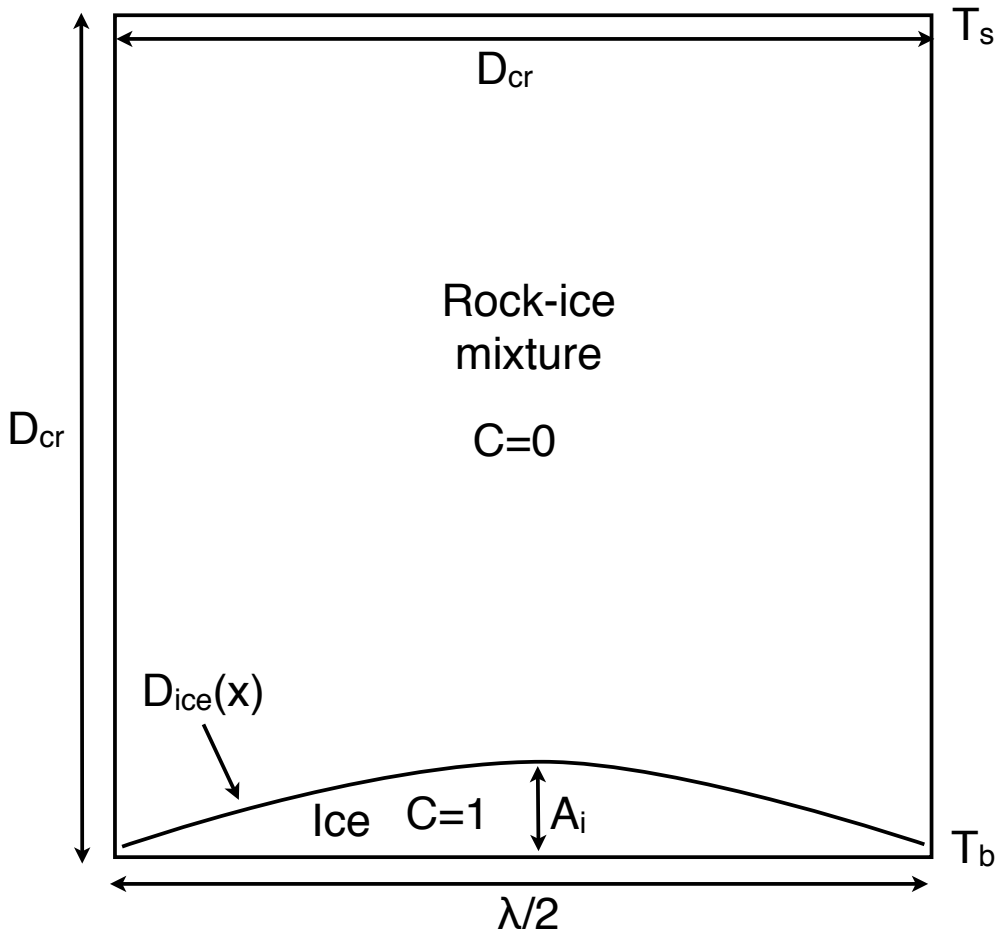

Figure 13: Initial setup for the calculation.

The initial conditions are set as shown in Fig. 13. We consider the two-dimensional calculated area. Although a three-dimensional calculation may give more accurate results, considering the uncertainty of the interior structure of Ceres, a simple two-dimensional calculation is enough to analyze the upwelling of diapir as a first step. The temperature increases linearly from T_s at the top to T_b at the bottom. From the analysis of the crust's instability, T_b is fixed at 180 K. The boundary line of the perturbation $D_{\rm ice}(x)$ is given as

$$D_{\rm ice}(x) = A_i \sin\left(2\pi \frac{x}{\lambda}\right), \tag{40}$$

where x and A_i are the horizontal length and amplitude of the perturbation, respectively. In this calculation, we assume that the horizontal scale of the initial perturbation is the same as the thickness of the crust. Thus, the wavelength λ is set at $2D_{cr}$. We assume two amplitude ratios of A_i/D_{cr}=0.1 and 0.2, which is consistent with the stability analysis. The assumed structure model has a scale ratio of 1×1. However, we perform the numerical calculations for just half of the diapir in order to reduce the calculation time, meaning the scale ratio is actually 1×2. The grid resolution is 20×40. We ran a calculation with 30×60 resolution, and confirmed that the two results are not different. Thus, we use 20×40 resolution to reduce the calculation time. Free-slip conditions are employed at every boundary. Although there are other boundary conditions such as rigid boundary, flee-slip is reasonable considering the surface and bottom movement of the crust.

Calculations are performed using the finite difference method until the diapir reaches the surface or the evolution time substantially exceeds 4.5 Gyr (the age of the solar system). For the calculations, we use stream function, and erase the pressure by combining the two equations shown in Eq. (33). In order to solve each equation, modified Cholesky decomposition method is used. As for the calculations of advective term, we use upwind method. We tried the calculations with different values of T_s and D_{cr}. From thermal

calculations, the crustal thickness D_{cr} was found to be more than 10 km (McCord and Sotin, 2005; Castillo-Rogez and McCord, 2010). In addition, considering the diameter of the observed dark spot, which is around 60 km (Küppers et al., 2014), we consider D_{cr} to be between 10 km and 60 km.

3.5 Upwelling of diapirism

A calculation result for diapirism at T_s=170 K is shown in Fig. 14.

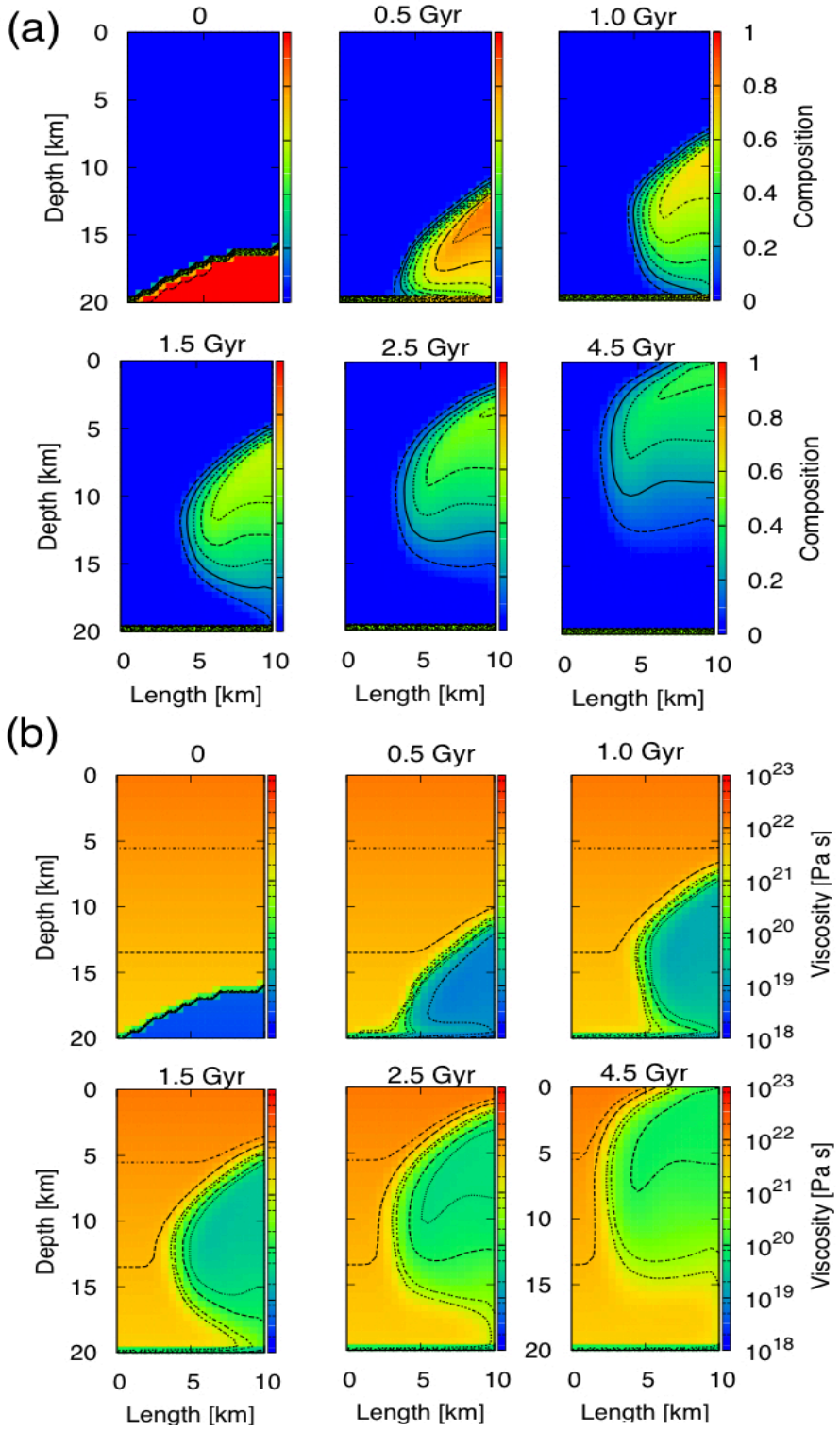

Figure 14: Evolution of a diapir with T_s=170 K, D_{cr}=20 km and A_i/D_{cr}=0.2. (a) and (b) show distributions of composition and viscosity, respectively. Calculations are performed for half of the diapir to reduce the computational cost. The generated diapir reaches the surface within 3.4 Gyr.

In the case of D_{cr}=20 km, once an instability composed of pure ice is induced, a diapir is generated over the subsequent 500 Myr (Fig. 14), and then begins to rise to the surface. As the diapir rises to the surface, the composition decreases by expansion of the diapir. We assume that the crust and diapir viscosities depend on their respective temperatures, which decrease from the bottom to the surface. This viscosity contrast suppresses the vertical movement of the diapir, which results in the diapir's expansion and the decrease of C. However, the buoyancy of the diapir is sufficient to produce the upwelling through the crust. In our calculation, in the case of T_s=170 K, D_{cr}=20 km and A_i/D_{cr}=0.2, the diapir reaches the surface after 3.4 Gyr, and is followed by the appearance of pure ice (Fig. 14).

Fig. 15 shows the time it takes for the diapir to reach the surface from the formation of the instability. We define the time that the diapir reaches the surface as that when $C > 0.1$ at the top of the crust.

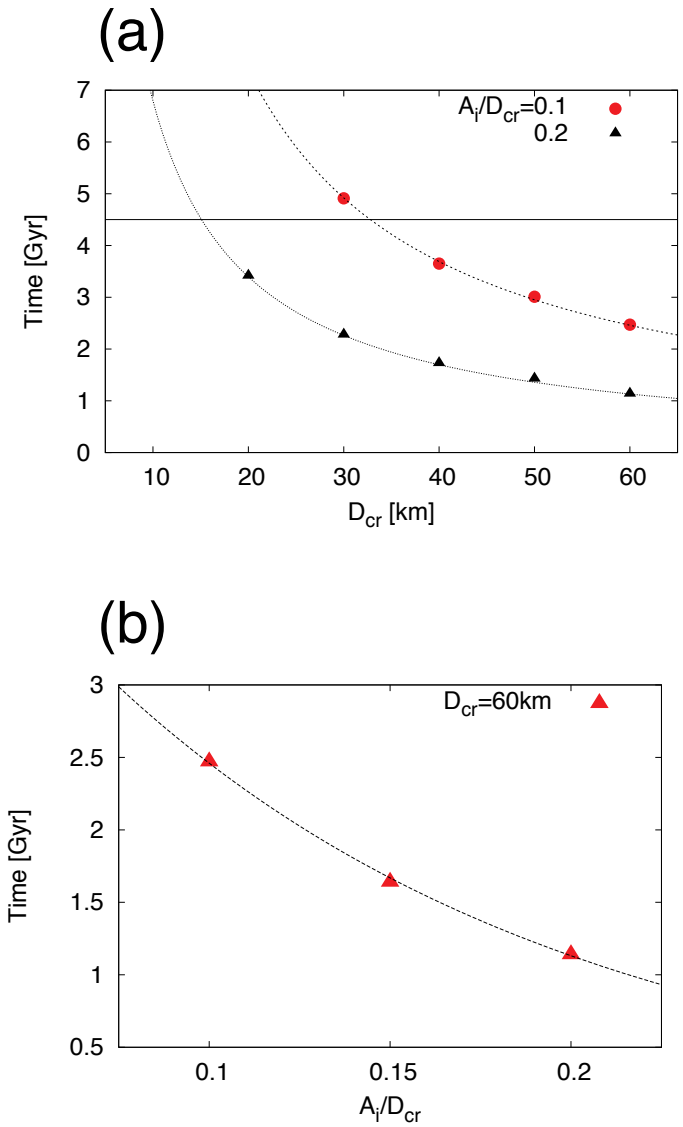

Figure 15: Time taken to reach the surface as a function of (a) the crustal thickness and (b) the amplitude ratio for a 60 km thick crust. The horizontal line in (a) is the age of the solar system (4.5 Gyr). The dotted lines in (a) and (b) are the times calculated using Eq. (41). In order that the fresh ice appears at the surface now, diapir should reach the surface in around 3 Gyr. In our calculation, 20-30 km thick crust is appropriate.

Given the fixed ratio between A_i and D_{cr}, the rising time decreases with increasing crustal thickness, which is due to the increase in buoyancy. Rc increases with the cube of the crustal thickness. Thus, although the crust is thicker, the higher buoyancy reduces the rising time overall. The rising time decreases with the inverse of the crustal thickness (Fig. 15 a). We note that this inverse relationship is valid when the horizontal scale of the initial perturbation is similar to that of the crustal thickness. If the horizontal scale of the perturbation becomes small, the magnitude of the buoyancy is reduced, and the inverse relationship becomes invalid. When the amplitude of the initial perturbation doubles, the time decreases by a factor of 0.46 (Fig. 15 b). From these results, the time to reach the surface $\tau_{\rm surf}$ scales as

$$\tau_{\rm surf} = 2.46({\rm Gyr}) \left(\frac{60({\rm km})}{D_{cr}({\rm km})} \right) \times 0.46^{\left(\frac{A_i/D_{cr}}{0.1} - 1 \right)}. \tag{41}$$

This time scaling is useful to estimate whether the diapir can reach the surface for arbitrary values of D_{cr} and A_i/D_{cr}.

If vapor emission is induced by diapirism, upwelling pure ice should have appeared at the surface in the recent past. We set the geological time scale for the long-term stability of the crust as 1.5 Gyr. Assuming that upwelling began with the generation of the perturbation, the diapir should reach the surface around 3 Gyr. In the case that A_i/D_{cr} is 0.2, a 20-30 km thick crust is appropriate for the time scale of upwelling. In our calculation, a 10 km thick crust is too thin for the diapir to reach the surface within the solar system age. However, Eq. (41) shows that if A_i/D_{cr} is around 0.3 (3 km thick perturbation), the diapir can reach the surface by around 3 Gyr.

Fig. 16 shows the composition and temperature distributions when the diapir reaches the surface.

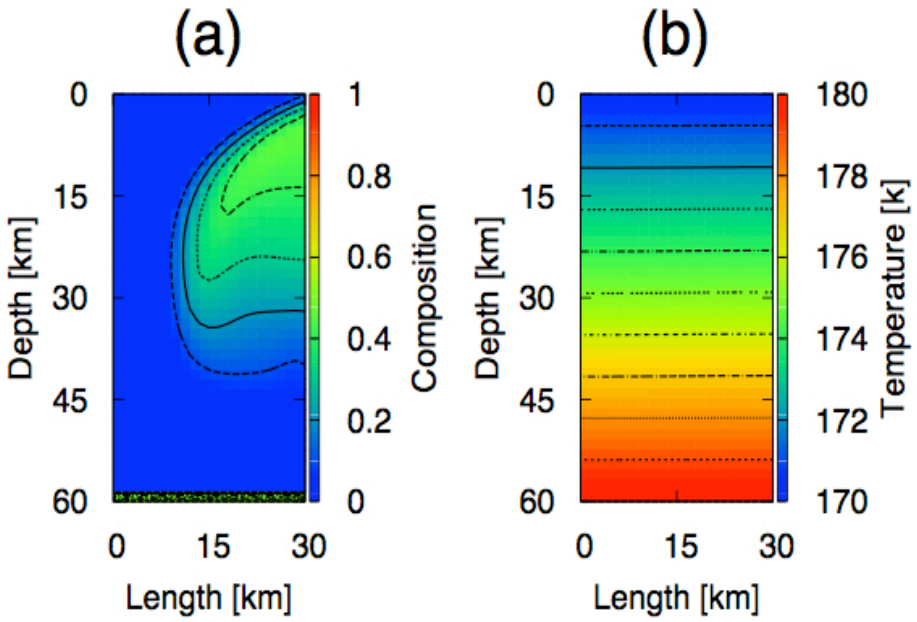

Figure 16: (a) Composition and (b) temperature distributions at 1.1 Gyr with T_s=170 K, D_{cr}=60 km and A_i/D_{cr}=0.2. Temperature distribution is not affected by the generated diapir. Thus, even though the impurities are contained in the ice, ice does not melt by the temperature change. For the vaporization of the ice, another mechanism such as sublimation is required.

In our work, D_{cr}=60 km and A_i/D_{cr}=0.2 are the conditions under which the diapir rises in the shortest time. Although the diapir reaches the surface, the temperature gradient changes very little. This is because the thermal Rayleigh number is very small for 180 K ice and the time scale in which the diapir rises is large, meaning that the temperature gradient is hardly affected. Thus, the diapir cannot melt the surface ice even if it contains ammonia. In order for the diapir to induce a vapor emission, an additional mechanism, such as the sublimation of the transported pure ice, is required.

Fig. 17 shows the case in which T_s=150 K, D_{cr}=60 km and A_i/D_{cr}=0.2.

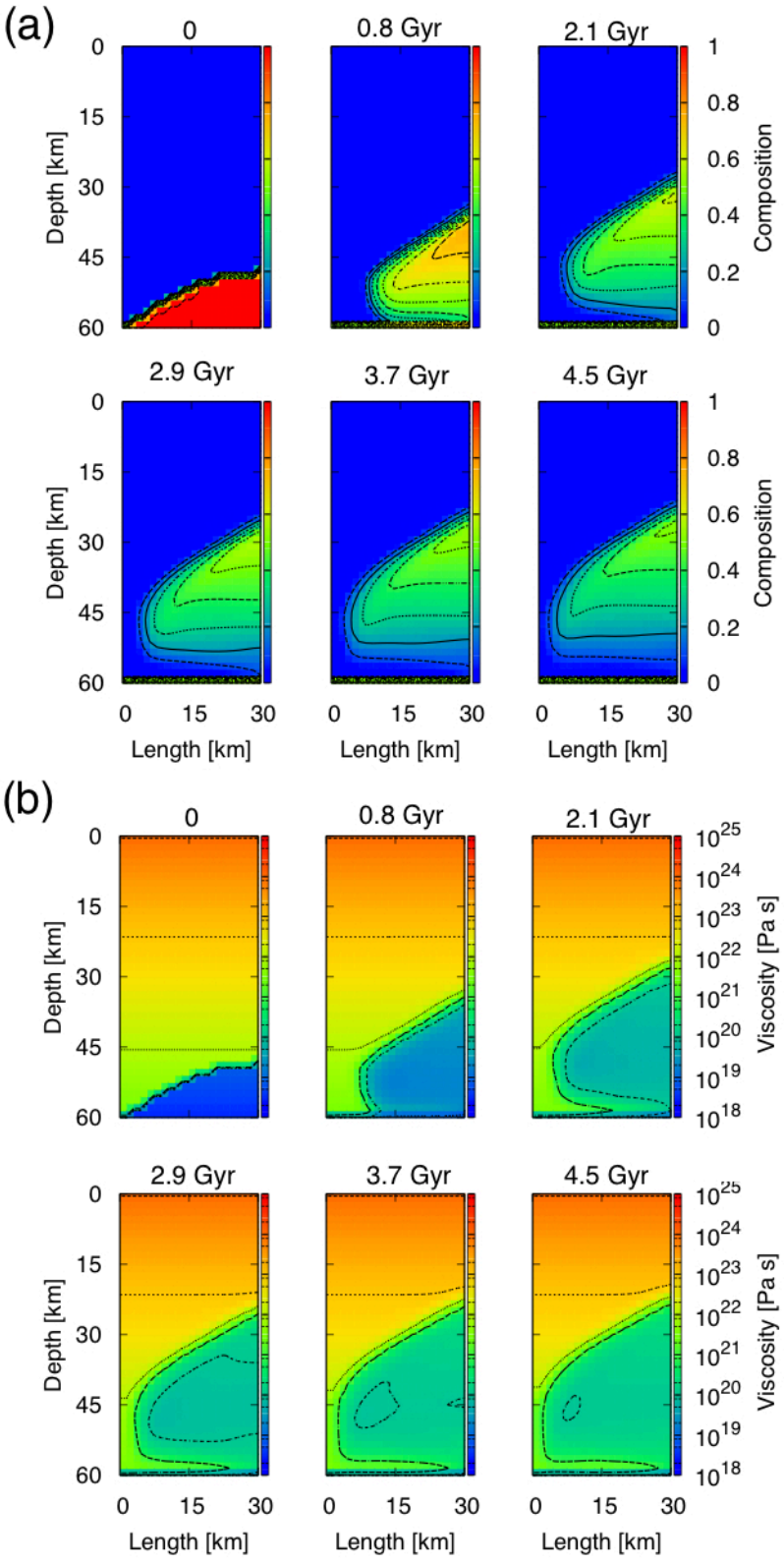

Figure 17: Evolution of a diapir with T_s=150 K, D_{cr}=60 km and A_i/D_{cr}=0.2. (a) and (b) show distributions of composition and viscosity, respectively. By the large viscosity contrast, diapir cannot reach the surface. Thus, around the high-latitude area, diapir cannot appear at the surface.

The diapir is formed within 800 Myr and rises. However, the diapir expands laterally. Due to the large viscosity contrast because of the small surface temperature, lateral expansion is easier than vertical expansion. The diapir rises from the bottom to a depth of 30 km within 2 Gyr. However, because the viscosity of the crust is very large, the upwelling velocity decreases drastically after that. 4.5 Gyr after the formation of the perturbation, the diapir has only reached a depth of 23 km. Thus, in our calculation, the diapir cannot reach the surface even within 4.5 Gyr. Due to the large buoyancy, the rising time of the diapir decreases with increases in both the thickness of the crust (Fig. 15). Thus, if the crust is thinner than 60 km, it is more difficult for the diapir to reach the surface.

In these calculations, we do not take into account the effect of impurities on the rheology. If impurities such as ammonia are contained, ice will melt at around 176 K. The viscosity of partially melted ice is drastically reduced (Arakawa and Maeno, 1994; De La Chapelle et al., 1999), and thus the thermal and compositional Rayleigh numbers increase significantly. In this case, the diapir can reach the surface more easily; however, the crust would be unstable and consequently subside.

3.6 Localization of the dark spots and emission

Numerical calculations show that the diapir reaching the surface is dependent on the surface temperature. The most accurate estimation, made by Bland (2013), makes Ceres' surface temperature 140 K in the polar regions and 180 K in the equatorial region. This temperature distribution is valid even though obliquity changes with time (Fig. 10).

Thus, in the equatorial region, the interior temperature should be higher than the long-term critical temperature of the Rayleigh-Taylor instability, which results in the subsidence of all of the crust. If all of the crust subsides, a compositional diapir cannot be generated. On the other hand, the interior in the mid-latitude and polar regions may be

colder than the long-term critical temperature, allowing the crust to be maintained for a long time. For this reason, a diapir may be induced in these regions. However, in the polar regions, the surface temperature is less than 150 K, which, according to our calculations, stops the diapir from reaching the surface. Hence, the diapirism morphology appears only in the mid-latitude regions (Fig. 18).

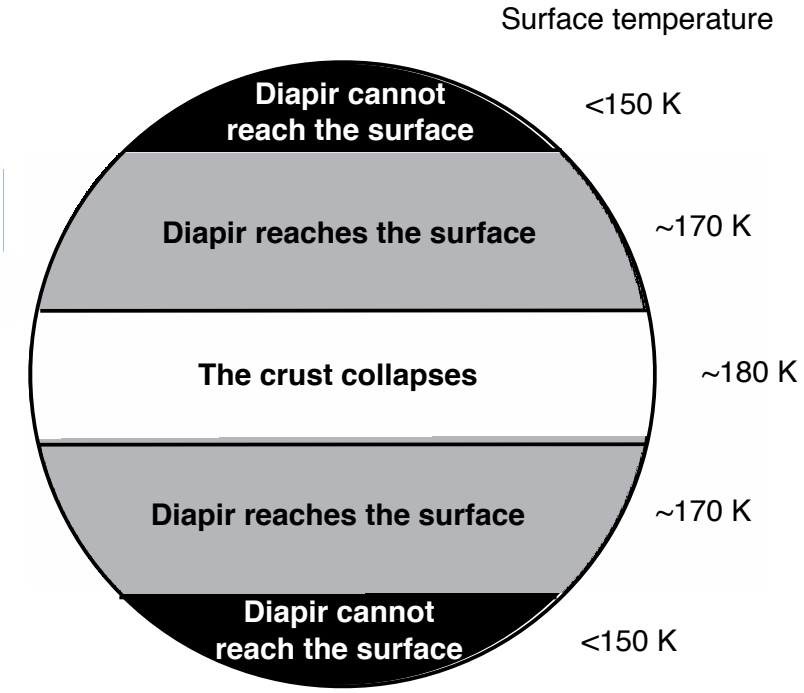

Figure 18: Schematic view of the regions where a diapir-induced morphology can appear. Around the equatorial region, surface temperate is the same to the long-term critical temperature for the subsidence of the crust. Thus, all crust has been renewed, which cannot generate diapirism. On the other hand, mid- and high-latitude areas have lower surface temperature. Thus, origin surface crust may be preserved now. However, surface temperature is too low for diapir to reach the surface. The moderate temperature around the mid-latitude is enough to preserve the crust, and for the diapir to reach the surface of Ceres.

If the dark spots are related to diapirism, our calculations are consistent with the observations of water vapor emission through sublimation around the mid-latitude regions only (Küppers et al., 2014). Such sublimation would require a supply of fresh ice, for which diapirism is a possible mechanism that transports pure ice to the surface. As mentioned in Section 3.2, a problem with the sublimation hypothesis is that it should occur in the equatorial region because its surface temperature is high. However, our analysis suggests that the high surface temperature causes the old crust to subside rapidly. Thus, a compositional diapir cannot be induced and fresh ice is not present at the surface in this region, and hence the vapor emission is observed in the mid-latitude regions only.

3.7 Uncertainty and problem of the calculation method in this work

For the calculations of diaprism, we considered the small amount of perturbation of the ice, and the boundary condition of the bottom area was assumed to be free-slip. One caveat is that we do not consider supply of further pure ice from the bottom. The property that mid-latitude area is suitable for the generated dispir to reach the surface does not change. However, if more ice goes up to the crust, diapir has more buoyancy and thus diapir may reach the surface at the low surface temperature. For the calculation of the advection term, although we used upwind method for simplicity, particle method has been suggested as the precise calculation method, which can be revised point for the future work.

3.8 Relationship to surface composition

Although detailed observation with high resolution has not been done yet, spectroscopic measurements on Ceres have been performed, which leads to speculation of surface chemical composition. Here, we discuss the relationship between the surface composition and diapirism. Although surface composition of Ceres is not unambiguously determined, re-

view is given by Rivkin et al. (2011). As mentioned in Section 3.1, absorption band at 3.06 μm is observed, and the origin of the absorption may be the feature of water ice (Lebofsky, et al., 1981). However, some suggestions against ice also have been given. Milliken and Rivkin (2009) interpret this absorption band is induced by $Mg(OH)_2$. Absorption at 11.4 μm is pointed out as the existence of (Mg, Ca)CO_3 (Rivkin et al., 2006). Thus, $Mg(OH)_2$ should be generated from Mg-carbonate by H_2O (Rivkin et al., 2009). Even though 3.06 μm absorption is not the sign of water ice, it seems that Ceres contains H_2O inside.

So far, clear evidence of water ice has not been detected by spectroscopic measurement regardless of the detection of vaporization. The reason why spectroscopic measurements cannot detect the ice is that the area of vaporization may be too narrow to be detected from the Earth. The fact that $Mg(OH)_2$ exists on the surface indicates that some area of Ceres overturned with interior layer. We can suggest that equatorial area where all crust subsides is the field of $Mg(OH)_2$. This area interacted with interior and water ice also appeared on the surface. However, by exposure to the space for a long time, water ice already has depleted by the past sublimation. In this work, equatorial crust subsides within 1.5 Gyr, and thus ice exposed by the overturn is on the surface for more than three billion years. It is implausible that ice remains for 3 Gyr and vaporizes now. Thus, observed vaporization is induced by the fresh ice transferred by the diapir, and $Mg(OH)_2$ is the feature of the past overturn at equatorial region. The area of the two dark spots which radiate vapor are narrow compared with other area. In addition, we cannot rule out that vapor is generated from crack wall of the dark spot, which results in the failure of spectroscopic detection of H_2O. It is probable that surface evolution of Ceres is not uniform but diverse (Rivkin et al., 2009). For the confirmation, the spatial distribution of surface composition is needed.

Organic molecules also can constrain the surface state of Ceres. If primordial crust is preserved in some area, this area should have relatively primitive condition. It is probable that Ceres accreted from the carbonaceous chondrites. If the primordial surface exists, organic compound may be preserved (Rivkin et al., 2011). On the other hand, it should disappear at the resurfaced area (Rivkin et al., 2011). If organics are detected by the future observations around the dark spots in midlatitude, it may be the evidence of the primordial crust. Although we cannot say confidently, the amount of organic material may have contrast between midlatitude and equatorial areas if the primordial crust is preserved. If our hypothesis on the diapirism is correct, surface composition has contrasting features between the equatorial and high latitude areas. Renewed crust should exist around the equatorial area while the primordial material exists around the mid and high latitude. Thus, spatial distribution of surface composition will be the factor to discriminate the surface state. We expect Dawn mission can detect this compositional variation with latitude.

Spectroscopic measurements from the Earth have limitation for detailed analysis of the surface state and evolution. We cannot say now whether or not diapirism occurs on Ceres. Dawn mission must be the key observation for the Ceres research, which will begin in 2015.

4 Thermal–orbital coupled tidal heating and habitability of Martian-sized extrasolar planets around M stars

4.1 Planets around M stars

The search for extrasolar planets has revealed that there are many terrestrial planets out of our solar system (e.g., Léger et al., 2009). By detecting these extrasolar terrestrial planets, many researches have tried to determine the planets' thermal and orbital histories (Henning et al., 2009; Barnes et al., 2010; Léger et al., 2011; Wagner et al., 2012). The thermal and orbital states of extrasolar terrestrial planets are important for the planets' evolution. In addition, the thermal and orbital states affect the habitability, making analysis of these factors of key importance.

Recently, in the search for habitable extrasolar planets, M stars were suggested for observation (Scalo et al., 2007) because the number of M stars is much larger than that of G stars. Conventionally, M stars are not considered to be likely hosts of habitable planets because their planets' orbits are too close, which results in the planets being tidally rocked (synchronously rotated) and their atmosphere freezing on the dark side. However, Joshi et al. (1997) hypothesized that carbon dioxide can make a planet habitable. Thus, the importance of M star extrasolar planet analysis continues to increase.

4.2 Importance of tidal heating at exoplanets

Focusing on the terrestrial planets in our solar system, the main heat sources are the insolation from the Sun and the radioactive decay in the planets themselves. However, if extrasolar planets orbit around small stars such as an M star, the tidal heating has a significant effect on the habitability. Compared with the Sun, M stars have low temperatures, and thus the magnitude of the insolation becomes low. Therefore, the habitable zone is closer to the star. The rate of change of a planet's orbit due to tidal dissipation increases

with decreasing orbital distance. For this reason, a planet orbiting an M star may not be able to stay within the habitable zone for a long time. In addition, assuming that the planets orbit according to Kepler's law, the tidal frequency is high, producing tidal heating that may exceed the radiogenic and insolation heating. In contrast to the terrestrial planets in our solar system, such tidal heating is an important factor for the thermal and orbital evolutions of planets orbiting M stars.

The effects of tidal heating on terrestrial planets orbiting M stars have been analyzed (Jackson et al., 2008; Barnes et al., 2008). Although these researches revealed that tidal heating influences a planet habitability, they assumed that the magnitude of the dissipation of the planet is constant. The tidal heating mechanism is complicated and interacts with the internal thermal state and orbit of the planet (e.g., Hussmann and Spohn 2004). When a planet is tidally heated, structure and thermal states of the planet changes, which affects the tidal heating by the feed-back. In addition, the orbit and heating rates also interact with each other. Tidal heat dissipation is dependent on the eccentricity of the orbit; the eccentricity decreases with heating rate because orbital energy is lost as tidal heat. Thus, tidal heating should be coupled with orbital and thermal evolution.

In this section, we evaluate the coupled calculation of tidal heating considering the thermal and orbital states. However, coupled calculations are very complex. In addition, the internal structure of extrasolar terrestrial planets is not constrained well. Thus, as a fist step, we consider a Martian-sized terrestrial planet. An advantage of this choice is that the internal pressure of planets of this size is small compared with earth-sized planets, due to their small radii, which allows a simple model of the internal structure to be used. A Martian-sized planet has been discovered (Muirhead et al., 2012); however, this planet is outside the habitable zone. Despite this, we can expect similarly sized planets to be discovered within habitable zones in future observations. Considering the observation,

Earth-sized planets are easier to detect compared to Martian-sized planet. However, we try the coupling theoretical calculation with Martian structure. In our solar system, Io is a tidally locked rocky satellite with high tidal heating (Segatz et al., 1988). Thus, we reference the thermal model of Io as well as Mars. If accurate internal structures of super-Earths are derived in the future, we can apply the results of this work to such models with more complicated structures.

4.3 Structure and evolution for the coupling calculation

4.3.1 Interior structure

In this work, for simplicity, we assume that the internal structure of the planet is composed of three layers: a liquid core, a mantle and a stagnant lid (Fig. 19 a).

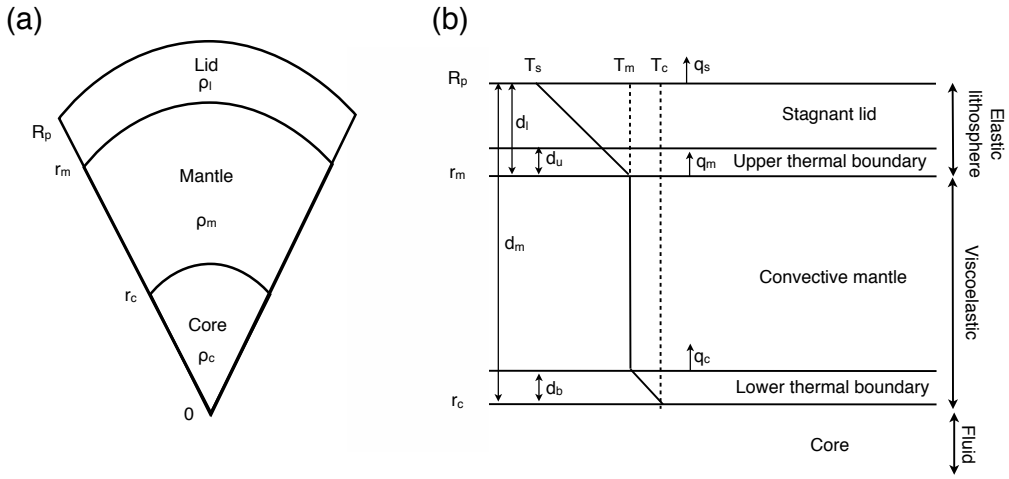

Figure 19: Structural and thermal models of the planet at (a): global scale and (b): local scale. For the calculations, the stagnant lid and upper thermal boundary of the mantle are assumed to be elastic because of the low temperature (defined as the lithosphere). Tidal heating occurs in the convective mantle and lower thermal boundary area. The core is fluid, and no tidal heating occurs in the core.

Stagnant lid convection occurs in the mantle. Because stagnant lid convection is the most typical convection system, scaling laws which relate the magnitude of the convection to the structure have been analyzed by many researches (e.g., Reese et al., 1999 b). Although mobile lid convection (e.g., O'Neill and Lenardic 2007) or heat pipe state (Moore 2001; Moore and Webb 2013) are suggested as alternative heat transfer mechanisms, we assume the stagnant lid convection as the heat transfer model in this work. Rheology and temperature distributions depend only on the radial distance (i.e., are independent of latitude and longitude). The mantle is differentiated into three parts: two thermal boundaries and a well mixed convective section (Fig. 19 b). At the two boundaries, heat is transferred by conduction. In this work, we define the lid and the upper boundary of the mantle as the lithosphere. The lithosphere is assumed to be elastic, and tidal heat is generated only in the mantle by viscoelastic dissipation (Hussmann and Spohn 2004). This assumption is valid because the surface temperature is less than 300 K in the habitable zone, which is much smaller than the mantle temperature (more than 1600 K). In the convective part, for simplicity, we assume that convective temperature is T_m and independent of depth. T_m changes with time both by the heating and cooling.

The rate of change of the mantle and core temperatures T_m and T_c are calculated based on the energy balance (Breuer and Spohn 2006).

$$\rho_m c_m V_m \epsilon_m (St+1)\frac{dT_m}{dt} = -4\pi r_m^2 q_m + 4\pi r_c^2 q_c + Q_{\rm tide} + Q_{\rm rad} \tag{42}$$

$$\rho_c c_c V_c \epsilon_c \frac{dT_c}{dt} = -4\pi r_c^2 q_c. \tag{43}$$

Here, the subscript m and c refer to properties of the mantle and core, respectively. ρ_m and ρ_c are the densities, c_m and c_c are the heat capacities, V_m and V_c are the volumes, r_m and r_c are the radial distances from the center to the convective mantle and the core,

respectively. ϵ_m is the ratio between the average mantle and upper boundary temperatures (Grott and Breuer 2008 b). In the case of adiabatic thermal model, temperature changes with the depth. Thus, effect of ϵ_m is required. ϵ_m ranges between 1.0 and 1.05 (Breuer and Spohn 2006; Grott and Breuer 2008 b). Because this range is around 1.0, Eq. (42) is applicable to the isothermal mantle model which we consider in this work. We conducted the calculations with different values of ϵ_m, and confirmed that the value of ϵ_m little affects the results. ϵ_c is the ratio between the average core and lower boundary temperatures, which is 1.1 (Breuer and Spohn 2006; Grott and Breuer 2008 a). The values of each parameter are shown in Table 2.

Table 2: Physical parameters and values.

Parameter	Symbol	Value	Unit	Reference
Planet radius	R_p	3390	km	1
Planet mass	M_p	6.3×10^{23}	kg	1
Core radius	r_c	1550	km	1
Lid density	ρ_l	3500	kg m^{-3}	
Mantle density	ρ_m	3500	kg m^{-3}	1
Core density	ρ_c	7200	kg m^{-3}	1
Mantle heat capacity	c_m	1200	J kg^{-1} K^{-1}	2
Core heat capacity	c_c	840	J kg^{-1} K^{-1}	2
Latent heat of melting	L_m	6×10^5	J kg^{-1}	3
Ratio of mean and upper mantle temperature	ϵ_m	1.0-1.05		1, 3
Ratio of mean and core temperature	ϵ_c	1.1		1, 3
Lithosphere thermal conductivity	k_l	4.0	W m^{-1} K^{-1}	
Mantle thermal conductivity	k_m	4.0	W m^{-1} K^{-1}	1
Core thermal conductivity	k_c	50.0	W m^{-1} K^{-1}	2
Mantle expansivity	α	4×10^{-5}	K^{-1}	2
Core expansivity	α_c	2×10^{-5}	K^{-1}	2
Mantle diffusivity	κ	10^{-6}	m^2 s^{-1}	1
Albedo	A	0.3		4
Reference temperature	T_0	1600	K	5
Mantle activation energy	E	300	kJ mol^{-1}	2
Lid shear modulus	μ_l	50	GPa	5
Lid viscosity	η_l	10^{40}	Pa s	
Anelasticity parameter	n_a	0.25		6
Melt fraction coefficient	B	30		7

(1) Grott and Breuer 2008a; (2) Nimmo and Stevenson 2000; (3) Breuer and Spohn 2006; (4) Paige et al. 1994; (5) Fischer and Spohn 1990; (6) Jackson et al. 2002; (7) Moore 2003

St is the Stefan number, which accounts for the consumption or release of latent heat by the mantle (Breuer and Spohn 2006). St is represented as the ratio of latent heat to the heat capacity of the mantle, and is given by

$$St = \frac{L_m}{c_m} \frac{V_a}{V_m} \frac{d\phi}{dT_m}, \tag{44}$$

where L_m is the latent heat of the mantle (Breuer and Spohn 2006). ϕ is the volume melt fraction, which is discussed below. V_a is the volume of the melt zone. Effect of melt in the rock has been studied by many researches (e.g., Rosenberg and Handy 2005). When mantle begins to melt, melt is distributed to the frame and junctions of grain boundaries. By increasing the melt fraction, melts among grains begin to be interconnected each other. However, as long as the melt fraction is under the critical value called the rheological critical melt percentage (RCMP), grain framework is maintained (Rosenberg and Handy 2005). When the melt fraction exceeds the RCMP, melt covers the grain completely and effect of liquid dominates. Considering these effects, if the melt fraction is under the RCMP, we assume that the convective area of the mantle is well mixed and that melt is not separated from the solid mantle; thus, $V_a = V_m$. This assumption may not be valid if the melt fraction exceeds the RCMP because the generated melt segregates from the solid mantle. However, we found that melt fraction of our coupled calculation is less than the 25 % at every condition, and Moore (2003) estimates that the segregation of melt occurs at the 40 % to 60 % of melt fraction. Thus the assumption of mantle with partial melt state is reasonable. $Q_{\rm rad}$ is the heating due to radioactive decay. For simplicity, we use the averaged radiogenic heating in the Martian mantle estimated by Grott and Breuer (2008 b). The volumetric radiogenic heating $q_{\rm rad}$ is given by

$$q_{\rm rad} = q_0 \exp(-\lambda t), \tag{45}$$

where $q_0 = 1.6 \times 10^{-8}$ W m^{-3} and $\lambda = 1.5 \times 10^{-17}$ s^{-1} (Grott and Breuer 2008 b). Thus, $Q_{\rm rad} = q_{\rm rad} V_m$. We do not consider the radiogenic heating from other parts of the planet. In the core of the Earth, potassium can be the large heat sources in the core, and Mars may contain potassium, but the stability of potassium in iron is extremely small at low pressure such as the case for the Martian core (Gessmann and Wood 2002). Thus, we ignored the heat generation in the core.

q_m is the heat flux from the mantle, which is given by (Nimmo and Stevenson 2000). In the case of stagnant lid convection, q_m can be related to the Nusselt number Nu as

$$q_m = k_m \frac{\Delta T}{d_m} Nu, \tag{46}$$

where k_m is the thermal conductivity of the mantle. ΔT is the temperature difference between top and bottom of the mantle. d_m is the thickness of the mantle. Assuming the newtonian viscosity, Nu can be scaled by the Rayleigh number Ra and Frank-Kamenetskii parameter θ (Reese et al., 1999 a) as

$$Nu \approx 0.5 \theta^{-\frac{4}{3}} Ra^{\frac{1}{3}}. \tag{47}$$

Ra is given by

$$Ra = \frac{\rho_m g \alpha \Delta T}{\kappa \eta_m} d_m^3, \tag{48}$$

where g, α and κ are acceleration due to gravity, thermal expansivity and thermal diffusivity of the mantle, respectively. η_m is the viscosity of the mantle, which is discussed in the next subsection. In this work, we assume the Arrhenius type viscosity, which mainly depends on the temperature. θ is given by

$$\theta = \Delta T \frac{E}{RT_i^2}, \tag{49}$$

where E and R are the activation energy and the gas constant, respectively. T_i is the internal temperature and defined as the mean temperature at the upper thermal boundary (Reese et al., 1999 b). Using Eqs. (28)-(49) q_m is given (Nimmo and Stevenson 2000) as

$$q_m = \frac{k_m}{2} \left(\frac{\rho_m g \alpha}{\kappa \eta_m} \right)^{\frac{1}{3}} \gamma^{-\frac{4}{3}}, \tag{50}$$

where

$$\gamma = \frac{E}{RT_i^2}. \tag{51}$$

Using the typical value of T_i=1800 K and $E = 300$ kJ/mol, γ becomes 0.011 (Nimmo and Stevenson 2000). In order to calculate the accurate value of γ, numerical calculation of convection is required (Reese et al., 1999 b). However, in this work, we fixed γ at 0.011 for simplicity. The heat flux from the core to the mantle q_c is given by

$$q_c = k_m \frac{T_c - T_m}{d_b}, \tag{52}$$

where d_b is the thickness of the lower boundary.

Thickness of the upper and lower thermal boundaries (d_u and d_b) are derived by Nimmo and Stevenson (2000). Through the upper thermal boundary, temperature drops by 8/γ and q_m of heat flux is transported from the mantle to the surface (Nimmo and Stevenson 2000). They mention that 8/γ of temperature drop is found by Solomatov (1995). Thus, d_u is given by

$$d_u = \frac{8 k_m}{\gamma q_m}. \tag{53}$$

In the case of the thickness of the lower boundary d_b, they assume that local Rayleigh number of the lower thermal boundary is the same to that of the upper thermal boundary. Under this assumption, local Rayleigh numbers are related as

$$\frac{\rho_m g\alpha(8/\gamma)d_u^3}{e^4\eta_m\kappa} = \frac{\rho_m g\alpha(T_c - T_m)d_b^3}{\exp(-0.5\gamma[T_c - T_m])\kappa\eta_m} = Ra_c, \tag{54}$$

where e and Ra_c are the Napier's constant and critical Rayleigh number (Nimmo and Stevenson 2000). From Eq. (54), the ratio between d_b and d_u is given (Nimmo and Stevenson 2000) as

$$\frac{d_b}{d_u} = 0.5(\gamma[T_c - T_m])^{-1/3} \exp\left(-\frac{\gamma(T_c - T_m)}{6}\right). \tag{55}$$

d_b can be calculated from Eqs. (53) and (55). The thickness of the lithosphere d_l and the surface heat flux q_s are related by

$$q_s = k_l \frac{T_m - T_s}{d_l}, \tag{56}$$

where k_l and T_s are the thermal conductivity of the lithosphere and the surface temperature, respectively. In this work, we assume that tidal and radiogenic heatings are generated in the mantle. Heat generation and loss in the lithosphere are ignored. Under this assumption, q_s equals q_m. Thus, from Eqs (50) and (56), the lithosphere thickness d_l can be calculated, which is required for the calculation of tidal heating.

If the surface of the planet is assumed to be in equilibrium with the insolation heat flux uniformly distributed over the surface, the surface temperature T_s is given by (Léger et al., 2009; Barnes et al., 2010)

$$T_s = (1 - A)^{1/4} g_e \left(\frac{R_*}{2a}\right)^{1/2} T_*. \tag{57}$$

If the heat transport is limited to the light side,

$$T_s = (1 - A)^{1/4} g_e \left(\frac{R_*}{a} \right)^{1/2} T_*. \tag{58}$$

A is the albedo of the planet, which is assumed to be constant at 0.3 (Paige et al., 1994). $g_e = 1.0$ is the effectiveness of the heat transport. a is the orbital distance, which is discussed in Section 4.3.3. R_* is the radius of the star, which can be related to the mass of the star through

$$\log_{10} \frac{R_*}{R_\odot} = 1.03 \log_{10} \frac{M_*}{M_\odot} + 0.1, \tag{59}$$

where $M_\odot$ and $R_\odot$ are the mass and radius of the Sun, respectively (Gorda and Svechnikov 1999). M_* is the mass of the star. T_* in Eq. (57) is the effective temperature of the star, which is given by

$$T_* = \left(\frac{L}{4\pi\sigma R_*^2} \right)^{1/4}, \tag{60}$$

where σ and L are the Stefan-Boltzman constant and luminosity of the star, respectively (Barnes et al., 2008). L is related to the mass of the star by

$$\log_{10} \frac{L}{L_\odot} = 4.101\mu^3 + 8.162\mu^2 + 7.108\mu + 0.065, \tag{61}$$

where $\mu = \log_{10}(M_*/M_\odot)$ (Scalo et al., 2007). $L_\odot$ is the luminosity of the Sun. Using Eqs. (57)-(61), T_s can be determined. We use the constant values as shown in Table 2 except for M_* and a. a changes with time according to the evolution of the orbit. In the case of M_*, we conduct the calculations by varying $M_*/M_\odot$ from 0.1 to 0.5, which is a reasonable range for an M star.

Melt fraction ϕ depends on the solidus and liquidus temperatures. The melt fraction is assumed to be 1.0 at the liquidus temperature and increases linearly from the solidus to

liquidus temperature (Moore 2003). The solidus $T_{\rm sol}$ and liquidus $T_{\rm liq}$ temperatures of the mantle are given as functions of pressure P (Takahashi 1990):

$$T_{\rm sol} = 1409.15 + 134.2P - 6.581P^2 + 0.1054P^3 \ \ {\rm K} \tag{62}$$

$$T_{\rm liq} = 2035 + 57.46P - 3.487P^2 + 0.0769P^3 \ \ {\rm K}. \tag{63}$$

Pressure depends on the depth z and can be calculated as

$$P(z) = \int_{R_p}^{z} \rho(z) g(z) dz, \tag{64}$$

where R_p is the radius of the planet. $\rho(z)$ is the density at z. $g(z)$ is the acceleration due to gravity at z, which can be expressed as

$$g(z) = \frac{M(r)G}{r^2}, \tag{65}$$

where r and G are radial distance (r=R_p–z) and the gravitational constant, respectively. $M(r)$ is the mass enclosed by a sphere of radius r, which is

$$M(r) = \int_0^r 4\pi r'^2 \rho(r') dr'. \tag{66}$$

We assume that the solidus and liquidus temperatures of the mantle are averaged between the top and bottom of the mantle (Hussmann and Spohn 2004):

$$\bar{T}_{\rm sol} = \frac{T_{\rm sol}(r_m) + T_{\rm sol}(r_c)}{2} \tag{67}$$

$$\bar{T}_{\rm liq} = \frac{T_{\rm liq}(r_m) + T_{\rm liq}(r_c)}{2}. \tag{68}$$

When T_m exceeds $\bar{T}_{\rm sol}$, the mantle begins to melt. Thus, ϕ can be expressed as

$$\phi = \frac{T_m - \bar{T}_{\rm sol}}{\bar{T}_{\rm liq} - \bar{T}_{\rm sol}}. \tag{69}$$

4.3.2 Tidal heating

For the calculation of the tidal heating, the mantle is assumed to behave viscoelastically. The tidal heating rate $Q_{\rm tide}$ can be obtained as follows (Segatz et al., 1988).

$$Q_{\rm tide} = -\frac{21}{2}\frac{(R_p n)^5 e^2}{G}{\rm Im}(\tilde{k}_2) \tag{70}$$

n is the mean motion of the planet. Assuming that the planet orbits according to Kepler's law, n can be related to the orbital distance a by $n = (GM_*/a^3)^{1/2}$. e is the eccentricity of the orbit, which is important for the coupled calculation because it interacts with the tidal heating. The evolution of e is discussed in Section 4.3.3. $\tilde{k}_2$ is the second degree complex Love number, which largely depends on the internal structure and rheology of the planet. In the case of spherical-shell structured models, the complex Love number can be calculated using the methods based on the gravity potential of the planet (Segatz et al., 1988; Tobie et al., 2005; Roberts and Nimmo 2008). Detailed theory and the precise method are reviewed by Tobie et al. (2005) and Roberts and Nimmo (2008). Here, we mention the outline.

Assuming the spherical-shell structure, displacement, stress and potential can be separated into radial function part and spherical harmonics (Alterman et al., 1959; Takeuchi and Saito 1972). Assuming the radial functions of displacement (y_1 and y_2), stress (y_3 and y_4), and gravity potential (y_5 and y_6) of a spherical shell model, they are related each other via propagation matrix A_{ij} as

$$\frac{dy_i}{dr} = A_{ij} y_j \tag{71}$$

where r is the radial distance from the center of the planet. For bodies with liquid cores, Sabadini and Vermeersen (2004) derived the components of A_{ij}, which is shown in the section of Encealdus. Each radial function is solved by the boundary conditions at the core and the surface. Love number of the spherical shell structure can be calculated (Tobie et al., 2005) by

$$k_2 = -y_5(R_p) - 1. \tag{72}$$

Note that Love number in Eq. (72) is not complex number because the radial function theory is developed for the elastic body. However, viscoelastic rheology model can be related to the elastic model by Fourier transformation, which is called correspondence principle (Bilot, 1954). By the Fourier transformation, radial functions of viscoelastic model becomes complex value in the domain of the frequency of applied force. Complex radial functions also can be related linearly via propagation matrix although each component becomes complex number. By solving the radial functions by the viscoelastic model, complex Love number can be calculated as

$$\tilde{k}_2 = -\tilde{y}_5(R_p) - 1, \tag{73}$$

where $\tilde{y}_5$ is the complex radial function of potential.

As for the rheology, we consider the Andrade model. An Andrade body is proven to fit well to the experimental results for the response of mantle rock (Jackson et al., 2002). The creep function for an Andrade body $J(t)$ is given by

$$J(t) = \frac{1}{\mu_m} + \beta t^{n_a} + \frac{t}{\eta_m}, \tag{74}$$

where t, μ_m and η_m are time, the shear modulus and viscosity of the mantle, respectively (Jackson et al., 2002; McCarthy and Castillo-Rogez 2013). n_a and β are the experimental

parameters, which represent the effects of the anelasticity of the material such as heterogeneity of the grain. If β is zero, the creep function becomes the conventional viscoelastic rheology (Maxwell model). β can be expressed as (Castillo-Rogez et al., 2011)

$$\beta = \frac{\mu_m^{n_a-1}}{\eta_m^{n_a}}. \tag{75}$$

This relationship is valid if the dissipation is dominated mainly by diffusion creep (Castillo-Rogez et al., 2011). n_a is the unconstrained empirical parameter, which ranges from 0.2 to 0.5. In this work, we use $n_a = 0.25$, which is based on the laboratory expedient of olivine (Jackson et al., 2002). Creep function at the frequency domain can be given (McCarthy and Castillo-Rogez 2013) by the Fourier transformation as

$$\tilde{J}(\omega) = \frac{1}{\mu_m} + \omega^{-n_a}\beta\cos\left(\frac{n_a\pi}{2}\right)\Gamma(n_a+1) - i\left[\frac{1}{\eta_m\omega} + \omega^{-n_a}\beta\sin\left(\frac{n_a\pi}{2}\right)\Gamma(n_a+1)\right], \tag{76}$$

where ω is the frequency, which is the same to the mean motion in the case of tidal heating. Γ and i are the gamma function and $\sqrt{-1}$, respectively. Complex shear modulus $\tilde{\mu}(\omega)$ of the Andrade model can be calculated as $1/\tilde{J}(\omega)$. Propagation matrix A_{ij} contains the complex shear modulus, which affects the tidal dissipation of the planet.

In the calculation of the tidal heating, the shear modulus and viscosity of the mantle are the most important factors. At temperatures under $\bar{T}_{\rm sol}$, the shear modulus is assumed to be constant at 50 GPa, which is a typical value for mantle rock. As for the viscosity, we adopt an Arrhenius function, which is the typical description for the mantle viscosity (e.g., Breuer and Spohn 2006):

$$\eta_m = \eta_0 \exp\left(\frac{E}{R}\left[\frac{1}{T_m} - \frac{1}{T_0}\right]\right). \tag{77}$$

$T_0 = 1600$ K is the reference temperature (Breuer and Spohn 2006) and η_0 is the reference viscosity at T_0.

When the temperature becomes higher than $\bar{T}_{\rm sol}$, the mantle begins to melt. If the melt is contained within the mantle, the shear modulus and viscosity drop drastically. As mentioned above, we assume that the partially molten mantle is well mixed. Reduction of the shear modulus and viscosity is controlled by the melt fraction ϕ. Moore (2003) gives the viscosity over the solidus temperature. When the melt fraction ϕ is under RCMP (40% to 60%), the viscosity of the mantle is multiplied by $\exp(-B\phi)$ where B is the dimensionless melt fraction coefficient. Thus, η_m becomes

$$\eta_m = \eta_0 \exp\left(\frac{E}{R}\left[\frac{1}{T_m} - \frac{1}{T_0}\right]\right)\exp(-B\phi). \tag{78}$$

In this work, we assume that RCMP is 40 $\%$. If the melt fraction exceeds the disaggregation point, the viscosity follows the Rascoe-Einstein relationship, which can be written (Moore 2003) as

$$\eta_m = 10^{-7}\exp\left(\frac{4\times10^4\ {\rm K}}{T_m}\right)(1.35\phi - 0.35)^{-5/2}\ \ {\rm Pa\ s}. \tag{79}$$

The shear modulus over the solidus temperature was determined by Fischer and Spohn (1990) to be $\mu_m = 10^{(\mu_1/T_m+\mu_2)}$ Pa, where $\mu_1 = 8.2\times10^4$ K. They also found that $\mu_2 = -40.6$ due to the continuous condition at the solidus temperature (1600 K in their work). In our calculation, the solidus temperature was calculated using Eq. (67). Thus, the shear modulus over the solidus temperature is

$$\mu_m = 10^{[\mu_1/(\Delta T_m+1600{\rm K})+\mu_2]}\ \ {\rm Pa}, \tag{80}$$

where $\Delta T_m = T_m - \bar{T}_{\rm sol}$. In addition, if ϕ exceeds the disaggregation point (0.4), the shear modulus is assumed to drop to 10^{-7} Pa (Moore 2003).

Figure 20 shows the tidal heating rate in the case of two layers (liquid core and mantle) as a function of viscosity and shear modulus of the mantle. Heating rates are calculated by Eqs. (70)-(76) with $M_* = 0.1 M_\odot$ and $e = 0.2$.

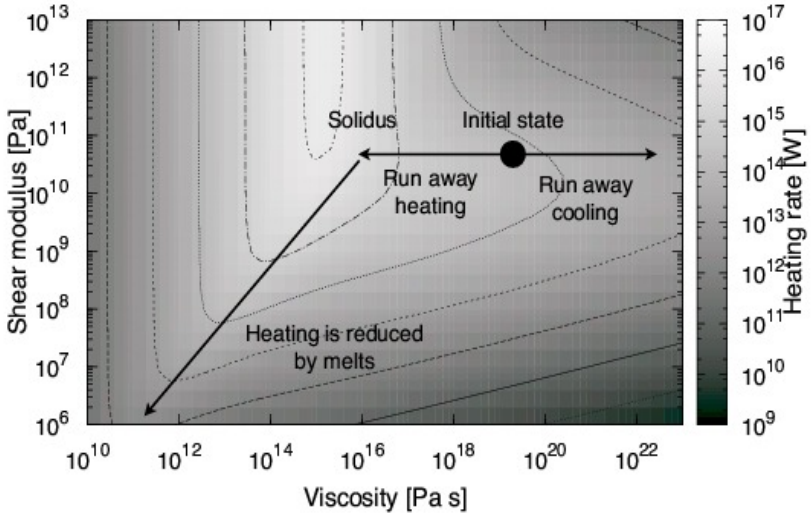

Figure 20: Heating rate of the two layer (core+mantle) model as a function of shear modulus and viscosity of the mantle. M_* and e are $0.1M_\odot$ and 0.2, respectively. Assuming the initial state at the circle point, two types of heating evolution (runaway heating or cooling) can be expected. If the temperature exceeds the solidus temperature, the melt reduces the mantle shear modulus and viscosity, which results in decreased tidal heating and ends runaway heating.

In the case of a 50 GPa shear modulus, the heating rates are maximized at a viscosity of 10^{15} Pa s. The peak of the heating rate is attained when the stress cycle is around the Maxwell time defined as η_m/μ_m. If we assume that the initial viscosity is 10^{19} Pa s, two types of heating state are possible. One evolution type is runaway cooling. If the heat radiated from the surface is larger than the tidal heating, the mantle cools and the viscosity increases. When the viscosity increases, the heating rates decrease as shown in Fig. 20. Thus, mantle cools more. The other heating state is runaway heating. If the tidal heating is large, the mantle temperature increases and the viscosity decreases according to Eq. (77), which results in increased tidal dissipation. However, runaway heating stops when the solidus temperature is reached. Because of the melt, the shear modulus and viscosity decrease, which results in a reduction of the heating rate (Fig. 20).

The coupled calculations in this work consider the three-layer model (the elastic lithosphere is included). The lithosphere works to decrease the heating rate because the displacement is reduced. An elastic layer can be included by considering the large viscosity of a viscoelastic layer. In our calculations, we set the viscosity of the lithosphere to 10^{40} Pa s. It is important to set a characteristic time for the viscoelastic body (η/μ) that is sufficiently larger than the tidal period to produce the desired elastic behavior. The shear modulus is set to 50 GPa. Thus, a viscosity of 10^{40} Pa s is sufficient to approximate the elastic body.

4.3.3 Orbital change

The interaction between tidal heating and orbital evolution is very complicated. In this work, following the work by Barnes et al. (2008), we use the classical orbital equations, which are based on the works of Goldreich and Soter (1966). By the dissipation of the central star by the planet, bulge is induced at the surface of the star. By the time delay of the displacement, direction of the bulge is different from the direction to the planet, which

induces the change of the angular moment of the planet. By the change of the angular momentum, orbital distance and eccentricity also changes. Dissipation also occurs in the planet by the central star. The dissipation of the planets reduces the eccentricity and the orbital distance. Orbital distance and eccentricity evolutions are given by the sum of the two dissipation. The rates of change of orbital distance a and eccentricity e are as follows.

$$\frac{da}{dt} = -\left(21\frac{\sqrt{GM_*^3}R_p^5 k_2}{M_p Q_p}e^2 + \frac{9}{2}\frac{\sqrt{G/M_*}R_*^5 M_p}{Q'_*}\right)a^{-11/2} \tag{81}$$

$$\frac{de}{dt} = -\left(\frac{21}{2}\frac{\sqrt{GM_*^3}R_p^5 k_2}{M_p Q_p} + \frac{171}{16}\frac{\sqrt{G/M_*}R_*^5 M_p}{Q'_*}\right)a^{-13/2}e \tag{82}$$

Here Q_p and Q'_* are the Q values of the planet and the star. Note that Q'_* is divided by two thirds and includes the value of the Love number of the star (Barnes et al., 2008). The first terms represent the effect of the dissipation of the planet. The second terms show the dissipation of the star. These equations consider the change of orbital distance, which is contrast to the Enceladus' tidal heating. Here, we calculate the long evolution of the planet. Thus, this complete orbital change equations are used. k_2 is the Love number of the planet, which is not complex but a real number. In the case of the viscoelastic rheology model, k_2 can be approximated by $|\tilde{k}_2|$. In addition Q_p can be represented by Re($\tilde{k}_2$)/Im($\tilde{k}_2$). The imaginary part of Love number is much smaller than the real part. Thus, we can write $k_2/Q_p \approx \mathrm{Im}(\tilde{k}_2)$. The complex Love number depends on the internal structure and thermal state of the planet, which affects the heating rate as shown in Eq. (70). Using the approximation shown above, we can relate the orbital, thermal, and heating evolution of the planet. We have to consider that Eqs. (81) and (82) are not valid when the orbital period of the planet is shorter than the rotational period of the star. In this case, the signs of the second terms change (Barnes et al., 2008). However, due to the large mass of the star compared to the Martian-sized planet, the values of the second terms are

significantly smaller than those of the first terms. Thus, Eqs. (81) and (82) are valid in this work. If the planet's mass is relatively large we need to consider the rotational and orbital periods, which may be important for the case of a super-Earth. Q'_* represents the magnitude of the star's dissipation, which also affects the orbital evolution of the planet. We tried the calculation with values between 10^5 and 10^7. However, even at $Q'_* = 10^5$, the first terms are larger than the second terms by more than six orders of magnitude. Thus, Q'_* does not affect the orbital evolution of the planet, and the effect of the dissipation of the planet is dominant unless Q'_* is unreasonably small. Thus, we use the constant value of $Q'_* = 10^{5.5}$ in every calculation shown in this paper.

The purpose of this work is a habitability analysis through coupled tidal calculations. Thus, as an initial condition for the orbital distance, we set the center of the planet between the inner and outer edges of the habitable zone (Jackson et al., 2008). The inner and outer edges of the habitable zone (l_{in} and l_{out}, respectively) were calculated by Barnes et al. (2008):

$$l_{in} = (l_{in\odot} - a_{in}T'_* - b_{in}T'^2_*) \left(\frac{L}{L_\odot}\right)^{1/2} (1-e^2)^{-1/4} \tag{83}$$

$$l_{out} = (l_{out\odot} - a_{out}T'_* - b_{out}T'^2_*) \left(\frac{L}{L_\odot}\right)^{1/2} (1-e^2)^{-1/4}, \tag{84}$$

where $a_{in} = 2.7619 \times 10^{-5}$ AU K^{-1}, $b_{in} = 3.8095 \times 10^{-9}$ AU K^{-2}, $a_{out} = 1.3786 \times 10^{-4}$ AU K^{-1} and $b_{out} = 1.4286 \times 10^{-9}$ AU K^{-2}. $T'_* = T_* - 5700$ K. T_* can be calculated using Eq. (60). However, if T_* is less than 3700 K, it should be 3700 K when considering T'_* (Barnes et al., 2008). $l_{in\odot}$ and $l_{out\odot}$ are the inner and outer edges of the solar habitable zone, respectively. They depend on the condition of cloud. $l_{in\odot}$ is $\sim$0.89 AU, $\sim$0.72 AU and $\sim$0.49 AU when the cloud cover is 0%, 50% and 100%, respectively. $l_{out\odot}$ is $\sim$1.67 AU, $\sim$1.95 AU and $\sim$2.4 AU when the cloud cover is 0%, 50% and 100%, respectively.

In this work, we take into account the habitable zone estimated by Barnes et al. (2008) as shown above. However, habitable zone shown in Eqs. (83) and (84) is based on the conventional estimations by Kasting et al. (1993) and Selsis et al. (2007). Recently, Kopparapu et al. (2013) revised the habitable zone based on new datas. In addition, habitable zone changes with time due to the evolution of the central star. We discuss the effect of the estimation and evolution of the habitable zone in the Section 4.6.

4.4 Calculation procedure

Although many equations are required for the coupled calculation, Eqs. (42), (43), (70), (81) and (82) are the main equations needed. Once the initial values of T_m, T_c, e and a are set, we can calculate properties of the internal structure such as the thickness of each layer and the thermal properties such as the surface temperature of the planet. Using the determined conditions, the complex Love number can be calculated, which is needed to calculate the tidal heating rate (Eq. (70)) and orbital evolution (Eqs. (81) and (82)). Using the calculated Love number and tidal heating rate, the rates of change of e, a, T_m and T_c can be determined, following which the internal structure and thermal properties are updated. Continuing this process, evolutional calculations based on the coupled calculations become possible. In our calculation, we integrate each value forward with a time step of 10^5 years for 10 Gyr. We tried other time step and confirmed that the original time step is valid for calculations. In some cases, mantle temperature exceeds the core temperature because the mantle is heated by tidal heating. In this case, we calculate the heat flux from the mantle to the core following Nimmo and Stevenson (2000). We separate the core into spherical shell and solved the conduction equation with 10^4 years of time step. However, if the stagnant lid thickness becomes very large, the convection in the mantle stops. Compared with the convective layer, the temperature of the conductive

layer is very low. Thus, the magnitude of the tidal heating is much smaller than that of a convective planet, and the tidal heating has little effect on the evolution. Our simple thermal and structural models are not valid for a conductive planet. In this work, the tidal heating in a conductive structure is out of our scope. Thus, when the convective mantle thickness becomes zero, we stop the calculations. Integrations were performed using the Runge-Kutta method. As for the initial values of eccentricity e_0, we considered a range of values less than 0.5. The initial values of T_m and T_c are not constrained. Thus we tried a wide range of temperatures between 1600 K and 2000 K. In addition, because the tidal heating in the mantle strongly depends on the mantle viscosity, we consider the reference viscosity η_0 as a free parameter between 10^{19} Pa s and 10^{20} Pa s.

4.5 Thermal-orbital tidal heating of the planet around M star

The thermal and orbital evolutions of the three-layer model are shown in Figs. 21 and 22. The initial values of T_m and T_c were 1800 K. The initial value of the semi-major axis was calculated considering habitability with 0% cloud cover. Surface temperature is determined by Eq. (57).

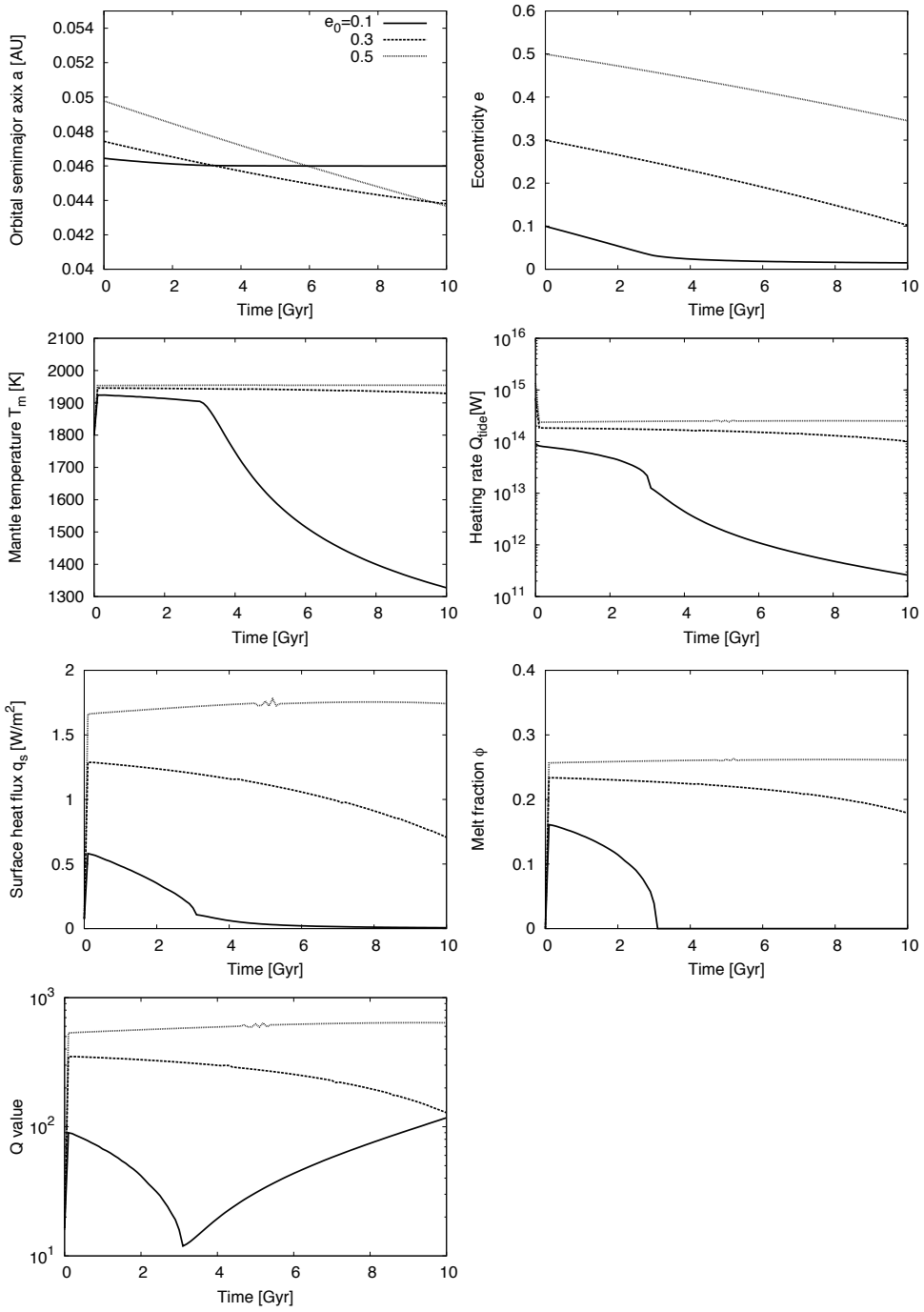

Figure 21: Orbital and thermal evolutions of the planet. Mass of the central star M_* is $0.1M_\odot$. $\eta_0 = 10^{19}$ Pa s. Initial values of the mantle temperature and core are 1800 K. Initial value of the eccentricity is 0.1 (solid line), 0.3 (dashed line) and 0.5 (dotted line). When the initial eccentricity is small, generated melt freezes again because eccentricity becomes small by the heating. In the case of large initial eccentricity, sufficient heat is generated and heating state becomes stable.

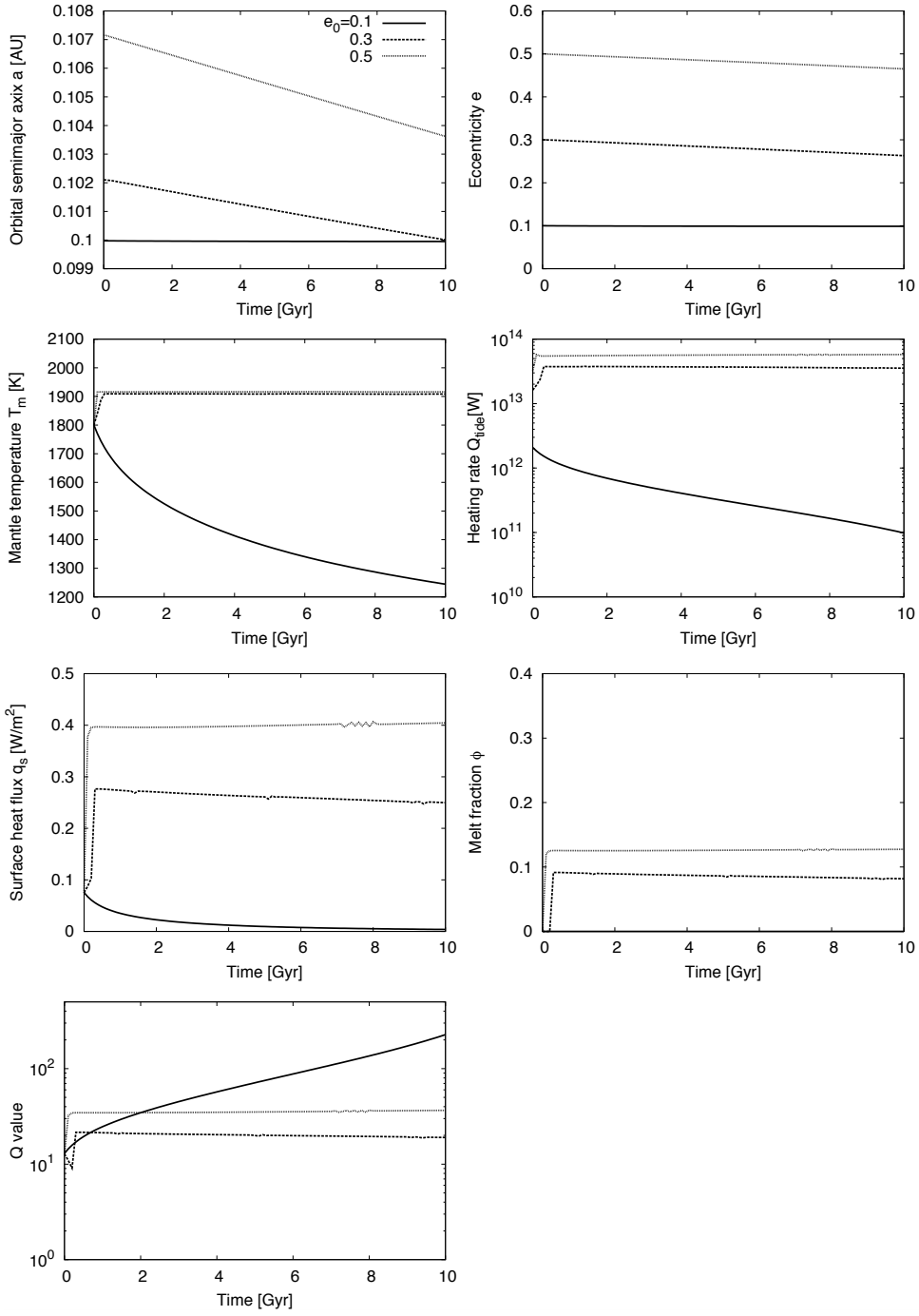

Figure 22: Orbital and thermal evolutions of the planet. Mass of the central star M_* is $0.2M_\odot$. $\eta_0 = 10^{19}$ Pa s. Initial values of the mantle temperature and core are 1800 K. Initial value of the eccentricity is 0.1 (solid line), 0.3 (dashed line) and 0.5 (dotted line). In the case of heavy central star, habitable zone is far from the star. Thus, the case that the initial eccentricity is 0.1 cannot generate the melt.

In the case of $M_* = 0.1M_\odot$ (Fig. 21), two types of evolution can be seen, depending on the eccentricity. Due to the initial conditions, a heating rate of more than 10^{14} W was generated with every eccentricity. Because of this large heat, the mantle temperature increases, inducing runaway heating. When the temperature exceeds the solidus temperature, the mantle begins to melt and the heating rates decrease as shown in Fig. 20. Because of the melt, runaway heating stops, and an equilibrium state is reached in which the radiated-heat rate is equal to the tidal heating. If e_0 is large enough, large heat is generated as shown in Eq. (70). Thus, the melt fraction becomes larger, which results in a large value of Q. Due to the large Q value, the eccentricity and semi-major axis do not change significantly even though M_* is small (the habitable zone is close to the star). Although semi major axis decreases by the tidal dissipation, it is far from the inner edge of the habitable zone in every case, which means that the planet stays in the habitable zone for more than 10 Gyr.

One caveat is that habitable zone itself changes with time because the luminosity of the central star changes. Thus, our estimation for the stability at the habitable zone of the planet may be too rough. However, Kopparapu et al. (2013) calculate the "continuous" habitable zone in which planets are habitable for 5 Gyr. In their calculation, continuous habitable zone of $0.1M_\odot$ mass star is between 0.2 AU and 0.5 AU. They also show the continuous habitable zone based on the model by Selsis et al. (2007). Our calculation results of the semi major axis are in the range of the continuous habitable zone of both models. Thus, we can say that Martian-sized planets can stay in the habitable zone for at least 5 Gyr.

If the value of Q is constant of the order of 10, the eccentricity is rapidly reduced and the tidal heating does not largely affect the thermal evolution of the planet. The orbital distance also changes significantly. However, considering the melt, the Q value increases

and the large eccentricity and semi-major axis are maintained, which is a difference between constant Q value calculations and the coupled calculations.

Due to the large eccentricity, relatively large heat generation occurs and the high temperature is maintained. This tidal heating is not too large because the melt reduces the viscosity and shear modulus. Thus, an equilibrium state occurs. However, at $e_0 = 0.1$, the heating rate is relatively small, which reduces the tidal heating, making an equilibrium state impossible to maintain. When the heating rate is reduced, runaway cooling occurs and the melt fraction also decreases. Radiogenic heating is not sufficient to heat up the mantle. The decreasing melt fraction causes the Q value to drop drastically. However, once the melt fraction becomes zero, the Q value increases again because the mantle temperature drops. The results in Fig. 21 are for the case in which the initial value of T_c and T_m were both 1800 K. We also tried with $T_c = 3000$ i.e., with an initial temperature difference of 1200 K. In that case the core temperature rapidly reaches the mantle temperature. Thus, the effect of a large T_c is small in terms of the evolution of the planet.

Barnes et al. (2009) analyzed the habitability focusing on the surface heat flux. Conventionally, the habitable zone is defined as the area where H_2O is kept in its liquid phase from models which assume that the ground is water saturated (e.g., Kasting et al., 1993). However, as well as liquid water, the surface state also plays an important role in determining habitability. Barnes et al. (2009) gave a condition for habitability based on the heat fluxes and surface states of Mars and the Jovian satellite Io. In their estimation, a heat flux of between 0.04 W m^{-2} and 2 W m^{-2} is required for habitability. If the magnitude of the heat flux is similar to Io, active volcanoes make the surface inhabitable. In our calculations, the hot equilibrium state of the planet radiates more than 0.5 W m^{-2} when $M_* = 0.1 M_\odot$ and e_0 is 0.3, which is the suitable value for the habitability. At e_0=0.5, although it does not exceed 2 W m^{-2}, the surface heat flux reaches the maximum limit.

Thus, the planet is predicted to have active volcanos like Io, which may make the planet inhabitable. If e_0 is less than 0.1, tidal heating is not enough to maintain the melt in the mantle, which results in cooling of the planet. From the coupled calculations, we can say that a Martian-sized planet that orbits in the habitable zone of an $M_* = 0.1M_\odot$ star is suitable for the habitability if the initial eccentricity is between 0.2 and 0.5. However, when the eccentricity is around 0.1, the heat flux exceeds 0.5 W m^{-2} at e_0=0.1. Thus, when we observe the Martian sized planet at the habitable zone of 0.1M$_\odot$ star, it is important whether the planet has the eccentricity more than 0.1 for the habitability. If observed eccentricity is over 0.1, the planet is predicted to have partial melt and the relatively large heat flux.

Figure 22 shows the case for $M_* = 0.2M_\odot$. Compared to the star with $M_* = 0.1M_\odot$, the melt fraction is small. At $e_0 = 0.1$, melt is not generated. Because the planet is assumed to orbit according to Kepler's law, the mean motion in the habitable zone is small. As shown in Eq. (70), the heating rate increases with n^5. Thus, tides cannot produce enough heat to generate large amount of melt in the case of $M_* = 0.2M_\odot$ star. Surface heat flux at the hot state is around 0.3 W m^{-2} and 0.4 W m^{-2} when e_0 is 0.3 and 0.5, respectively, which is suitable range for the habitability. The eccentricity does not change significantly for $M_* = 0.2M_\odot$ even though the Q value is relatively small because the orbital distance is large, which is different from the case of a $0.1M_\odot$ mass star. In the case of $M_* = 0.1M_\odot$, the orbital distance is small. However, the small rate of change of eccentricity is caused by the large Q_p due to the melt.

Through the coupled calculations, it has been determined that the thermal state of small extrasolar planets in habitable zones depends mainly on their initial eccentricity and the mass of their star. The initial value of the core temperature does not affect the heating state because tidal heating soon heats up the mantle anyway. Figure 23 shows the thermal

state as a function of the mass ratio of the star ($M_*/M_\odot$) and the initial eccentricity e_0 for different initial temperatures (T_{m0}) and reference viscosities (η_0). As can be seen in Fig. 23, the reference viscosity and initial temperature do not affect the heating states of the planet.

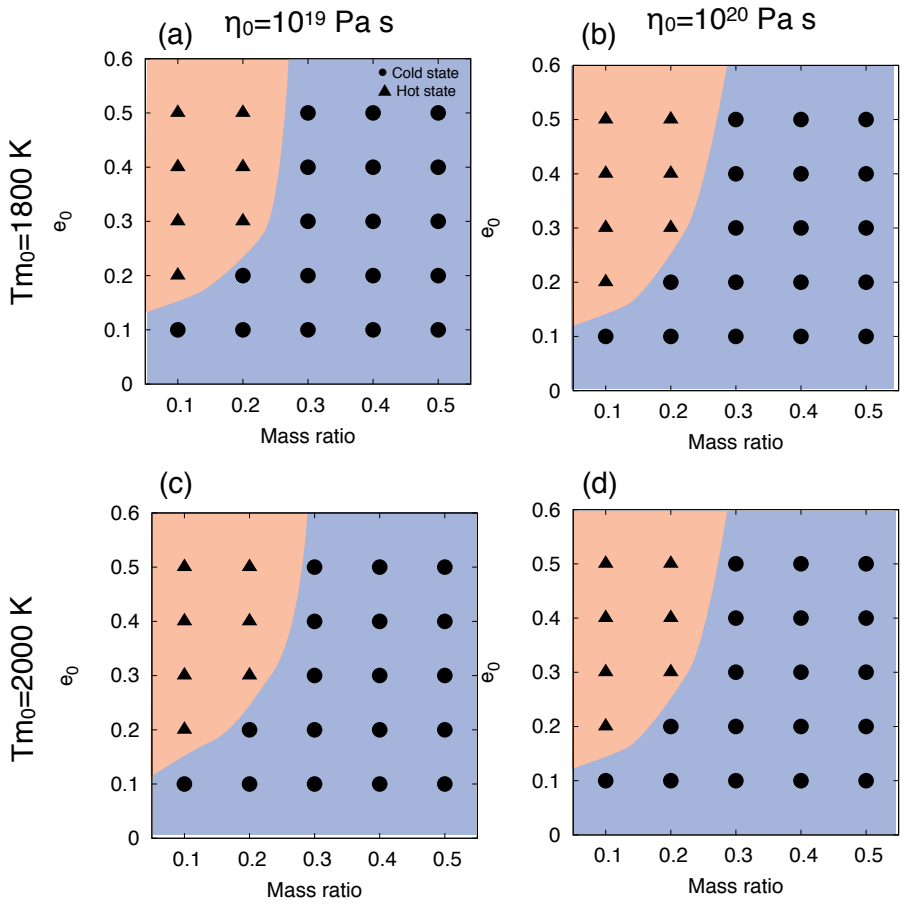

Figure 23: Heating state of the planet as a function of mass ratio of the star ($M_*/M_\odot$) and initial eccentricity of the planet (e_0). Triangle points show the hot state in which runaway heating and the melt induced equilibrium state occur. Circle points show the cold state, in which runaway cooling occurs. Top panels (a) and (b) show the results for T_{m0}=1800 K. Bottom panels (c) and (d) show the results for $T_{m0} = 2000$ K. T_{c0} is the same as T_{m0}. In the left panels (a) and (c), $\eta_0 = 10^{19}$ Pa s, and in the right panels (b) and (d) $\eta_0 = 10^{20}$ Pa s.

If the mass of the star is around $0.1M_{\odot}$, the planet reaches a hot state when $e_0 > 0.2$, independently of T_{m0} and η_0. As mentioned above, the planet can stay in the habitable zone for a long time in the hot state. If the mass of the star is around $0.2M_{\odot}$, a hot state occurs if $e_0 > 0.3$. If $M_*/M_{\odot}$ is more than 0.3, a hot state is not formed even though the eccentricity is quite large. The habitable zone of a star in this mass range is too far from the star for tidal heating large enough for runaway heating and melting of the mantle to occur. Since the cold planet has low temperature and rigid, stars of less than $0.2M_{\odot}$ in mass are good targets for finding habitable planets.

4.6 Environment induced by the tidally heated planet

4.6.1 Morphology

If the tidal heating is sufficiently large, the mantle is heated and the surface heat flux exceeds the Martian heat flux. In this work, we assume stagnant lid convection as a heat transport mechanism. As an alternative mechanism, plate tectonics may occur in planets in a hot state. Although it is currently only possible to observe the plate tectonics of Earth, it has been suggested that plate tectonics occurs in large, rocky extrasolar planets (e.g., Valencia et al., 2007). However, plate tectonics is a very complicated system and the main induction mechanism is not well understood. The size of the planet may affect the stress (Valencia et al., 2007; O'Neill and Lenardic 2007); however, Korenaga (2010) suggests that the effect of surface water is more important than the size of the planet. In our model, we do not include surface oceans and the size of the planets considered is relatively small. Thus, stagnant-lid convection is more reasonable. However, in the case of Mars, plate tectonics has been suggested to be the origin of the early internal dynamo (Nimmo and Stevenson 2000). Thus, plate tectonics cannot be ruled out for Martian-sized extrasolar planets.

Delamination may be more probable in small-sized extrasolar planets than plate tectonics. In a hot state, the melt in the mantle reduces the mantle viscosity. Thus, the bottom of the stagnant lid is delaminated and absorbed into the mantle. Delamination displaces the surface of the planet, which is the suggested cause of the corona of Venus (Smrekar and Stofan 1997). Thus, we can suggest that the planet is heated by tides, and the morphology of the planet is mainly a product of localized delamination processes caused by partial melting. As an alternative heat transfer model, heat pipe mode is suggested in Io and the Earth (Moore 2001; Moore and Webb 2013), which can be the important heat transfer mechanism for the tidally heated extrasolar planets. Thus, the effects of delamination and heat pipe should be considered in future work. In the case of delamination process, detailed calculations in super-Earths are conducted in the next section.

4.6.2 Magnetic field

It was revealed that Mars had an intrinsic magnetic field in the past (Acuña et al., 1999). The most probable origin of the intrinsic magnetic field is the dynamo in the core. The mechanism of the Martian dynamo is not well understood. However, it is required that more heat than that transported by adiabatic heat flux is transported from the core to the mantle in order to induce the core convection (Nimmo and Stevenson 2000). If tidal heat is not generated in the mantle, heat is transported sufficiently by the mantle and a dynamo may be induced. However, in our calculations, tidal heating heats up the mantle. In some cases, heat is even transported from the mantle to the core. Thus, in the hot state of a planet, it is unlikely the dynamo is activated.

An intrinsic magnetic field is not predicted in a tidally heated planet; however, if the orbital plane of the planet is oblique to the magnetic axis of the star, an induced magnetic field may be possible because of the melt in the mantle. In the case of Io, an induced magnetic field is observed (Khurana et al., 2011) . The induced magnetic field of Io is

consistent with a mantle of at least 20 % partial melt (Khurana et al., 2011). This melt fraction is comparable to our calculation results.

4.6.3 Heterogeneity of the planet

For simplicity, we assume that the internal structure of the planet is spherical shells and depends only on the radial distance. As for the habitable zone, the spherical-shell structure should provide a valid approximation because the temperature in light side is not so high. However, the heterogeneity of the planet is an interesting topic for future study, especially for planets that orbit significantly close to their stars. Tidal heating in a planet with a heterogeneous structure was calculated for the case of Enceladus, though it is extremely complicated (Tobie et al., 2008; Běhounková et al., 2012). If coupled calculations including a heterogeneous structure are possible in future work, an important comparison to the spherical-shell model of this work can be made.

4.6.4 Resonance

One caveat is that the coupled calculations in this work do not consider the resonance of the planet. If the planet is in a resonant state with other planets, the orbital evolution becomes significantly more complicated. Resonance among planets increases the planets' eccentricity, as exhibited by the Jovian satellites Io, Europa and Ganymede (Murray and Dermott 1999). Some satellites around Saturn also interact with each other (Murray and Dermott 1999). Hence, if there are multiple planets around a star, we must consider the resonance between them.

5 Delamination process of super-Earths

5.1 Plate tectonics controversy of super-Earths

Since extrasolar planets were discovered, many researchers have tried to analyze the internal structure and activity of super-Earths (e.g., Valencia et al., 2006; Kite et al., 2009; Wagner et al., 2011, 2012; Tackley et al., 2013). Such work is also important to the Earth itself because we can compare extrasolar terrestrial planets to the Earth. However, despite the extensive research undertaken, the internal activities of super-Earths are not known to high precision. For example, whether or not large rocky planets exhibit plate tectonics is of great interest because key related factors can be derived from the analysis of super-Earths. In addition, plate tectonics affects the habitability of the planet (e.g., Kasting and Catling, 2003). However, conclusions on this matter have been inconsistent. Valencia et al. (2007) and van Heck and Tackley (2011) stated that plate tectonics is likely in large planets due to the large shear stress while O'Neill and Lenardic (2007) concluded the opposite on the basis of large yield stress and fault strength. Other research has suggested that the likelihood of plate tectonics depends on additional conditions such as the water content (Korenaga, 2012), damage to the plate (Foley et al., 2012), the initial temperature (Naock and Breuer, 2014) and the internal heating rate (Stein et al., 2013). Modeling conditions and the rheology of the mantle also affect the tectonic behavior obtained for super-Earths (Karato, 2011, 2014; Stamenković et al., 2013; Stamenković and Breuer, 2014).

5.2 Delamination process

For the Earth, in addition to plate tectonics, delamination has been suggested as an internal activity mechanism (e.g., Bird, 1978, 79). The delamination process is caused by the peeling of the cold mantle lithosphere into the hot asthenosphere. This peeling is

caused by the thickening of lithosphere by the plate motion or material difference in the lithosphere. Extensive research has indicated that some morphologies are induced by the delaminating process (e.g., Gögüs and Pysklywec, 2008 a; Elkins-Tanton, 2005). Numerical calculations have also been performed using several models (Schott and Schmeling, 1998; Schott et al., 2000; Morency and Doin, 2004; Le Pourheit et al., 2006; Gögüs and Pysklywec, 2008 a, b; Valera et al., 2011). Morency and Doin (2004) analyzed the mechanism that induces delamination in detail. They revealed that small scale convection between the mantle lithosphere and asthenosphere causes local thinning of the mantle lithosphere, which forms a conduit from the asthenosphere to the crust. The flow of the asthenosphere in the conduit delaminates the mantle lithosphere. Then, the delaminated mantle lithosphere sinks into the asthenosphere.

Similarly to plate tectonics, we expect that delamination is an activity mechanism that takes place in extrasolar super-Earths. However, quantitative modeling of the delamination process in super-Earths has not been conducted until now. In this section, we analyze the magnitude of the delamination process in super-Earths. However, as plate tectonics research shows, the numerical results largely depend on the model parameters. In the next subsection, we describe our approach.

5.3 Delamination model of Earth and application to super-Earths

5.3.1 Structure

The structure of our model is mainly based on the work of Valera et al. (2011). Although other models exist (e.g., Schott and Schmelling, 1998), Valera's model is relatively simple. Because the internal structure and rheology of super-Earths are not well known, a simple model is effective for reducing the number of uncertainties. However, detailed models are also important for more accurate estimations, but these will be left for future

works.

Fig. 24 shows a schematic view of the initial structure.

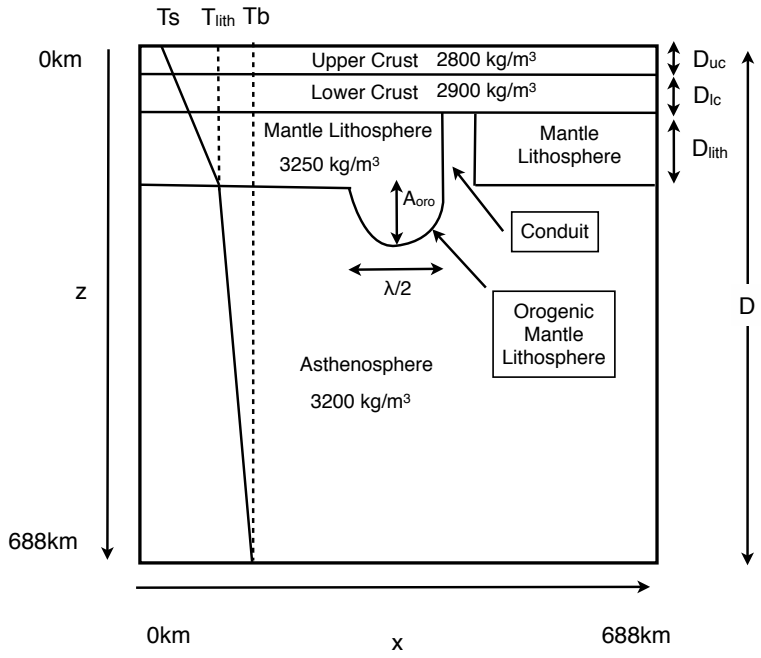

Figure 24: Schematic of the initial geometry and temperature distribution. The geometry of this model is based on that of Valera et al. (2011). The density contrast between the asthenosphere and the mantle lithosphere is assumed to be wet olivine and dry olivine, respectively.

The interior is composed of four layers: the upper and lower crusts, mantle lithosphere and asthenosphere. The mantle lithosphere is thicker at the center. This central layer represents the orogenic lithosphere (Valera et al., 2011) and can be regarded as the mantle lithosphere generated by the conduit formation, as was done by Morency and Doin (2004). The thickness of the orogenic mantle lithosphere D_{oro} is assumed to be sinusoidal and given by

$$D_{oro} = A_{oro} \cos\left[2\pi\left(\frac{x - 344(\mathrm{km})}{\lambda}\right)\right], \tag{85}$$

where A_{oro} and λ are the amplitude and wavelength of the orogenic mantle lithosphere. This thick mantle lithosphere has large negative buoyancy, which can initiate the delamination process. Although we consider the density of the mantle lithosphere to be homogeneous, additional negative buoyancy also results from the chemical difference in the delamination area (Göğüs and Pysklywec, 2008 b). In addition to the orogenic lithosphere, Valera et al. (2011) included the orogenic lower crust. However, in their calculation, the delamination process would have occurred even if it did not exist. If the orogenic crust is included, we have to consider its density and thickness, which means introducing additional uncertainties. Thus, for simplicity, we do not consider the orogenic crust.

For the delamination process, asthenospheric conduit is required. This conduit is generated by the small scale convection at the boundary between the mantle lithosphere and asthenosphere (Morency and Doin, 2004). Through this conduit, hot asthenosphere reaches the crust and the convection in the conduit peels away the mantle lithosphere.

The temperature in the crust and mantle lithosphere increase linearly from T_s at the surface to T_{lith} at the bottom of the mantle lithosphere. T_s and T_{lith} are fixed at 273 K (0° C) and 1623 K (1350° C) in every calculation (Valera et al., 2011). In the asthenosphere, the temperature increases according to the first order approximation of the adiabatic tem-

perature gradient as follows:

$$T_a(z) = T_{\rm lith} + \frac{\alpha_0 g T_{\rm lith}}{c_p}(z - D_{\rm lith} - D_{cr}), \tag{86}$$

where z, c_p and α_0 are the depth, specific heat and reference thermal expansion, respectively (Grott and Breuer, 2008). $D_{\rm lith}$ and D_{cr} are the thicknesses of the mantle lithosphere and the crust (D_{cr}=D_{uc}+D_{lc}). g is the acceleration due to gravity near the surface area, which is given by

$$g = \frac{GM}{R_p^2}, \tag{87}$$

where G and M are the gravitational constant and the mass of the planet, respectively. R_p is the radius of the planet. In this work, R_p was calculated from M using the scaling law $R_p \propto M^{0.27}$, which was derived by Valencia et al., (2006). Due to the increase in g, heavy planets have higher interior temperatures. For the thickness of the crust D_{cr}, we use the scaling law derived by O'Rourke and Korenaga (2012), $D_{cr} \propto M^{-0.284}$. In the case of an Earth-sized planet, D_{cr} is assumed to 37 km (Valera et al., 2011). This scaling law represents the crust thickness decreasing with increasing planet mass. One caveat is that this is derived by assuming a pressure independent rheology model (O'Rourke and Korenaga, 2012). As shown below we do consider the pressure dependence of the rheology. Thus, this scaling law may not be appropriate for our calculation. However, it is common for heavy planets to have a large surface gravity and the property of the crust thinning for large super-Earths can be applied to our calculation. Thus, we use their scaling law for the crust thickness for simplicity. For the delamination process, a low-viscosity lower crust is required (Morency and Doin, 2004). In the case of the model developed by Valera et al. (2011), a 15-km-thick upper crust and a 22-km lower crust were used. Because the upper crust thickness for a super-Earth is not constrained, we determined each crust

thickness by fixing the ratio of the upper and lower crust thicknesses although the whole crust thickness (D_{uc}+D_{lc}) changes with the mass of the planet. The viscosity of the crust is fixed as shown in Table 3 (Valera et al., 2011). As for $D_{\rm lith}$ for super-Earths, we perform calculations with different values to elucidate its effect.

Table 3: Physical parameters for calculations.

Symbol	Parameter	Value	Unit
Calculated thickness	D	688	km
Surface temperature	T_s	273	K
Bottom temperature of the mantle lithosphere	T_{lith}	1623	K
Wave width of the orogenic lithosphere	λ	487.2	km
Upper crust viscosity		10^{23}	Pa s
Lower crust viscosity		10^{20}	Pa s
Earth mass	$M_\oplus$	5.9742×10^{24}	kg
Earth radius	$R_\oplus$	6372	km
Specific heat	c_p	1300	$\mathrm{JK^{-1}kg^{-1}}$
Thermal conductivity	k	3.2	$\mathrm{Wm^{-1}K^{-1}}$
Reference thermal expansion	α_0	3.7×10^{-5}	$\mathrm{K^{-1}}$
Reference thermal diffusivity	κ_0	10^{-6}	$\mathrm{m^2\ s^{-1}}$
Reference viscosity	η_{ref}	10^{19}	Pa s
Reference temperature	T_{ref}	1573	K
Activation energy	E_a	500	$\mathrm{kJ\ mol^{-1}}$
Activation volume	V_a	6.4×10^{-6}	$\mathrm{m^3mol^{-1}}$

5.3.2 Theory

The evolution of the delamination process is calculated by solving the following non-dimensional equations.

$$\nabla \cdot \vec{u} = 0 \tag{88}$$

$$-\nabla P + \nabla \cdot [\eta(\nabla \vec{u} + \nabla^T \vec{u})] + (\mathrm{Ra}T - \mathrm{Rc}C)\vec{e} = 0 \tag{89}$$

$$\frac{\partial T}{\partial t} + \vec{u} \cdot \nabla T = \nabla^2 T - \mathrm{D_i} u_z T \tag{90}$$

$$\frac{\partial C}{\partial t} + \vec{u} \cdot \nabla C = 0, \tag{91}$$

Here, t is the time, $\vec{e}$ is the vertical unit vector, $\vec{u}$ is the velocity, P is the pressure, η is the viscosity, T is the temperature and C is the composition at each point. C represents the coefficient of the negative buoyancy caused by the composition. The initial distribution of C is given by the ratio of the density difference as follows:

$$C = \frac{\rho - \rho_{uc}}{\rho_{\mathrm{lith}} - \rho_{uc}}, \tag{92}$$

where ρ is the density as a function of position and ρ_{uc} = 2800 kg m^{-3} and ρ_{lith} = 3250 kg m^{-3} are the densities of the upper crust and mantle lithosphere, respectively. The density distribution is shown in Fig. 24. The negative buoyancy reaches a maximum at the mantle lithosphere where the largest value of C is found. The movement of each layer can be seen by the distribution of C, the evolution of which can be calculated by solving Eq. (91) at each time. D_i, Ra and Rc are the dissipation number and the thermal and compositional Rayleigh numbers, respectively. In this work, we scale each physical parameter by the physical values at the bottom, and thus each number is defined as follows:

$$\mathrm{D_i} = \frac{\alpha_b g}{c_p} D \tag{93}$$

$$\mathrm{Ra} = \frac{\alpha_b \rho_a g (T_b - T_s)}{\kappa_b \eta_b} D^3 \tag{94}$$

$$\mathrm{Rc} = \frac{(\rho_{\mathrm{lith}} - \rho_{uc}) g}{\kappa_b \eta_b} D^3. \tag{95}$$

ρ_a = 3200 kg m^{-3} and D = 688 km are the density of the asthenosphere and the thickness of the calculated area, respectively. α_b, κ_b and η_b are the thermal expansion, thermal diffusivity and viscosity at the bottom of the calculated area. For super-Earths, the pressure becomes very large, so we have to consider the pressure dependence of these parameters. The pressure dependence of the thermal expansion α and the thermal diffusivity κ are given by (Karato, 2014)

$$\frac{\alpha}{\alpha_0} = \left(1 + \frac{K_0'}{K_0} P\right)^{-1} \tag{96}$$

$$\frac{\kappa}{\kappa_0} = \left(1 + \frac{K_0'}{K_0} P\right)^{\frac{2q}{K_0'} + \frac{3}{2} - \frac{11}{6K_0'}}, \tag{97}$$

where P is the pressure. κ_0 is the reference thermal diffusivity at zero pressure. $K_0 = 260$ GPa, $K_0' = 4$ and $q = 1$ are constant values (Karato, 2014). For the viscosity of the mantle lithosphere and asthenosphere η, we use the Arrhenius function, which is given by

$$\eta = \eta_{\mathrm{ref}} \exp\left(\frac{E_a + PV_a}{RT} - \frac{E_a}{RT_{\mathrm{ref}}}\right) \tag{98}$$

where R is the universal gas constant. E_a and V_a are the activation energy and activation volume, which are given in Table 3 (Morency and Doin, 2004). T_{ref} and η_{ref} are the reference temperature and viscosity. We set the upper bound of the viscosity to 10^{22} Pa s (Valera et al., 2011). In addition to these parameters, the density also changes with

pressure. However, the calculations performed by Karato (2014) showed that the density change with pressure is small compared with other physical parameters even at a few hundred GPa. In our calculation, the pressure is no higher than 50 GPa. Thus, for simplicity, we ignore the pressure dependence of the density. The pressure is calculated from the gradient, which is given by

$$\frac{dP}{dz} = \rho g. \tag{99}$$

Fig. 25 shows the thermal and compositional Rayleigh numbers (Ra and Rc) as a function of the mass ratio ($M/M_{\oplus}$).

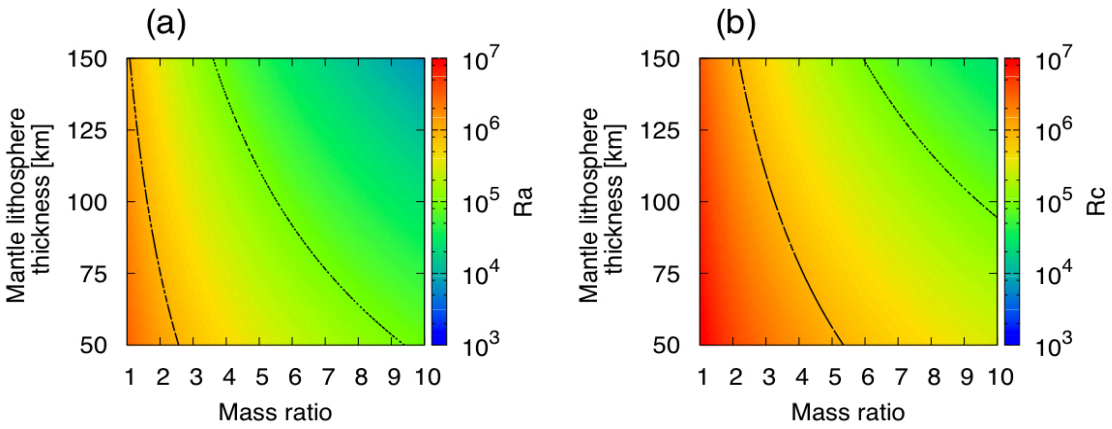

Figure 25: (a) Thermal and (b) compositional Rayleigh numbers as a function of the mass ratio of the planet ($M/M_{\oplus}$) and the mantle lithosphere thickness ($D_{\rm lith}$). The two contours are for 10^5 and 10^6. Rayleigh numbers decrease with the mass of the planet because effect of pressure on the viscosity is large. They also decrease with the thickness of the mantle lithosphere. We assume that the temperature at the base of the mantle lithosphere is fixed to the 1623 K. Thus, the asthenospheric temperature at the base of the calculated area decreases by increasing the mantle lithosphere thickness.

In our model, both Rayleigh numbers decrease as the mass of the planet increases. Although heavy planets have large g and high interior temperatures, the effect of increasing pressure is much larger. As shown by Eq. (98), viscosity increases with pressure although it is reduced by a high temperature. α decreases and κ increases with increasing pressure. These effects result in a decrease in the Rayleigh numbers. The Rayleigh numbers also decrease with mantle lithosphere thickness (Fig. 25). This is due to the reduction in the bottom temperature. In our model, the bottom temperature is determined by Eq. (86) with fixed T_s and $T_{\rm lith}$. In the case of a thick mantle lithosphere, the thickness of the asthenosphere is lower, which causes a reduction in the bottom temperature and an increase in viscosity.

Due to the small Rayleigh numbers, the vigorousness of the convection is reduced in large planets. However, stress, which delaminates the mantle lithosphere, becomes large at high viscosities. Thus, it is not certain that large Raleigh numbers induce more significant delamination. Through the calculations we compare the delamination in planets of $1M_\oplus$ and $5M_\oplus$ in mass. The resolution of the calculated area is 60×60 and the free slip condition is assumed at every boundary. For the calculation, we used the same method with the Ceres' diapirism. We use stream function, and solve each equation by modified Cholesky decomposition method. Upwind method is used for the calculation of the advective terms.

5.4 Delamination at heavy planets

The evolution of the delamination process for a $1M_\oplus$ planet is shown in Fig. 26.

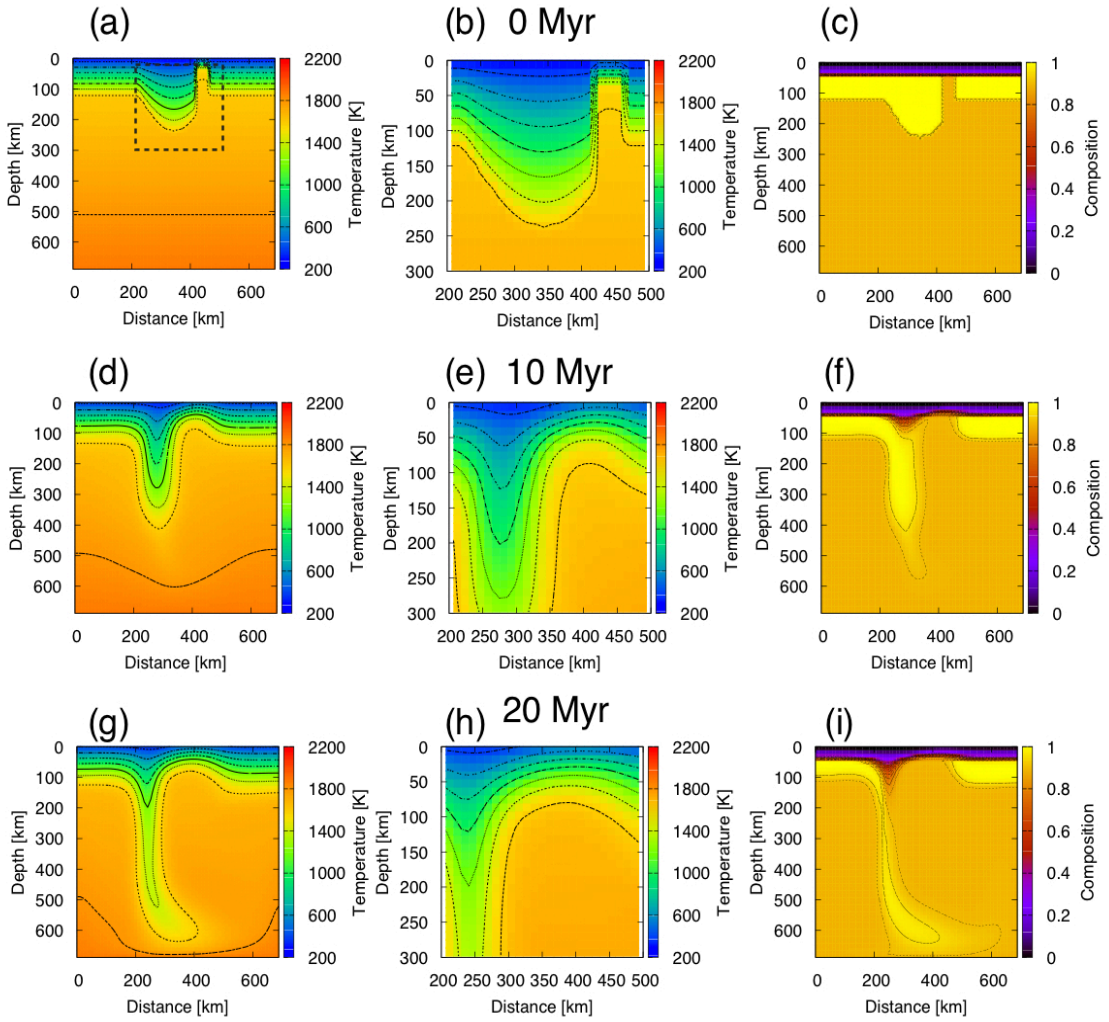

Figure 26: Evolution of the delamination for a $1M_{\oplus}$ planet. The mantle lithosphere is 83 km in thickness. The left column shows the temperature distributions and the right column shows the composition distributions. The temperature in the delaminated area (outlined in (a)) is shown in the central column. Delaminated area is around 200 km.

In this case the mantle lithosphere thickness was 83 km, which is the same as that in the model of Valera et al. (2011). Due to the negative buoyancy generated by the orogenic lithosphere, the mantle lithosphere sinks into the asthenosphere. At the same time, the convection of the asthenosphere in the conduit delaminates the mantle lithosphere from the lower crust. 20 Myr after the initiation of delamination, around 200 km of the mantle lithosphere in width had been delaminated into the asthenosphere (Fig. 26 i) and the downwelling lithospheric root had moved to the left side. This delamination process creates a larger temperature gradient in the crust (Fig. 26 h). Around 20 Myr after the initial state, the downwelling lithospheric root detaches from the mantle lithosphere (Fig. 26 i).

Fig. 27 shows that delamination occurs in a $5M_{\oplus}$ planet with the same mantle lithospheric thickness (83 km).

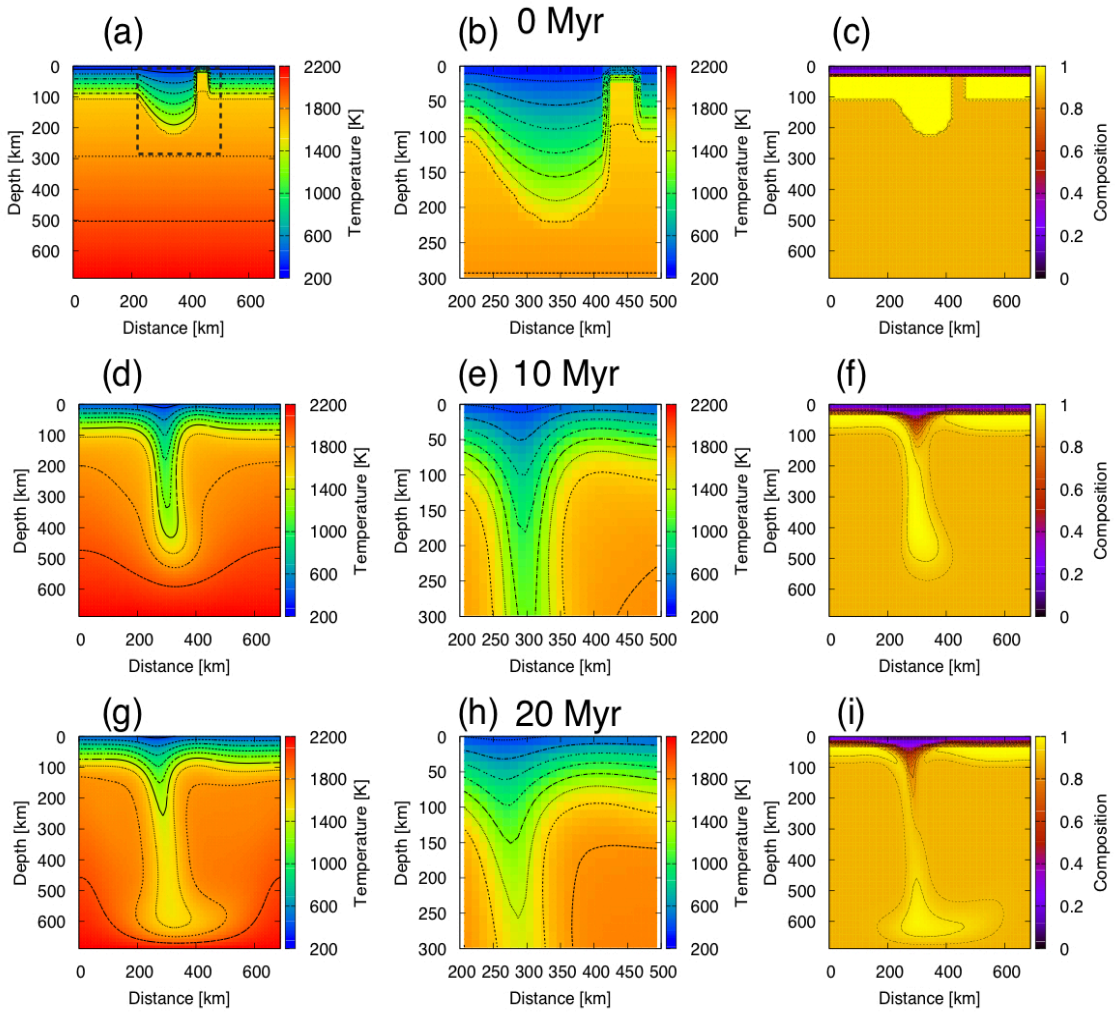

Figure 27: Evolution of the delamination for a $5M_{\oplus}$ planet. The mantle lithosphere is 83 km in thickness. The left column shows the temperature distributions and the right column shows the composition distributions. The temperature in the delaminated area (outlined in (a)) is shown in the central column. Delaminated area is around 100 km. Compared with a $1M_{\oplus}$ planet, delaminated area becomes narrower. This is due to the decrease of the magnitude of convection in the asthenosphere. The power of delamination decreases with the increasing of the mass of the planet.

Due to the small Rayleigh numbers, the magnitude of the convection in the conduit is smaller than that in the $1M_{\oplus}$ planet. Such convection is insufficient to vigorously delaminate the mantle lithosphere. Thus, the width of the delaminated area is around just 100 km in this case (Fig. 27 i). The large temperature gradient in the delaminated area is also reduced. Thus, in large planets, the delamination process cannot function as a mechanism that transfers large quantities of heat to the surface.

The calculations discussed above are for an 83-km-thick mantle lithosphere. However, because the magnitude of the mantle convection varies, the thickness of the mantle lithosphere will be different in super-Earths. Thus, we analyze the effect of the mantle lithosphere thickness on the vigorousness of the delamination. As shown in Fig. 26 and 27, delamination induces a large temperature gradient in the crust. If delamination occurs vigorously, the heat flux should have a large peak. Thus, we examine the relationship between the surface heat flux and the mantle lithosphere thickness as the vigorousness of the delamination. The surface heat flux is calculated by using $k(dT/dz)$ at $z = 0$, where k is the thermal conductivity.

Fig. 28 shows the surface heat flux for different thickness of the lithospheric mantle at 10 Myr.

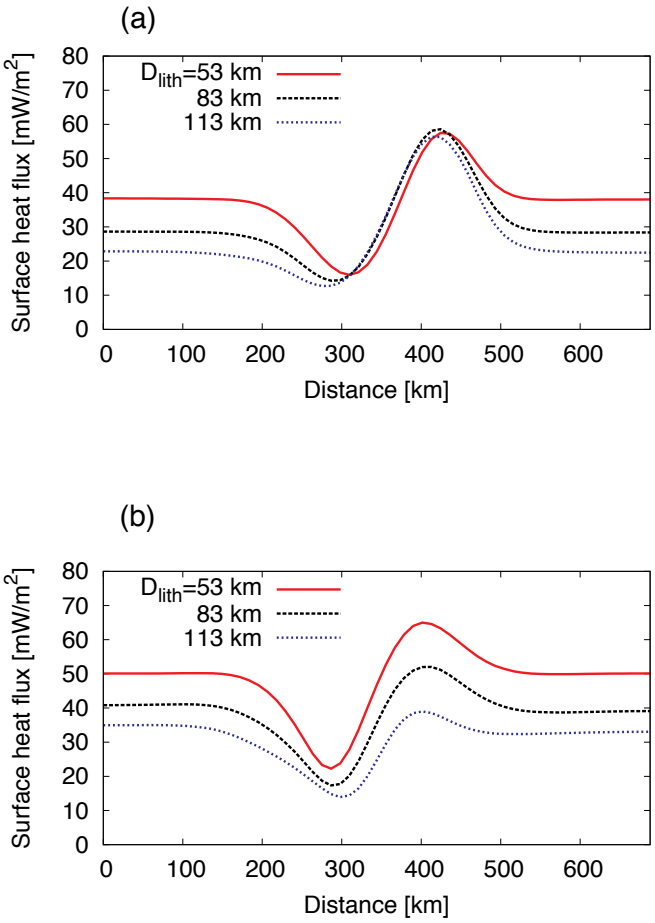

Figure 28: Surface heat flux for a (a) $1M_\oplus$ and (b) $5M_\oplus$ planet at 10 Myr for different thicknesses of the mantle lithosphere. In the case of Earth-mass planets, the peak of the heat fluxes are almost the same because asthenosphere reaches near the base of the lower crust. On the other hand, at heavy planet, peak of the flux decreases. This is because the asthenosphere cannot reach the lower crust by small vigorousness of the convection.

In the case of the $1M_{\oplus}$ planet, the peak value of the flux is almost independent of the mantle lithosphere thickness because the convection is sufficient to delaminate the mantle lithosphere even though $D_{\rm lith}$ changes. On the other hand, for the $5M_{\oplus}$ planet, the peak flux decreases with increasing mantle lithosphere thickness, which means that delamination cannot transfer large quantities of heat if $D_{\rm lith}$ is large. Typically, thick mantle lithospheres have large negative buoyancy. However, the reduction in the Rayleigh numbers caused by a thicker mantle lithosphere means the hot asthenosphere does not approach the Moho, which results in a reduction in the temperature around the Moho areas. In the case of a 113-km-thick mantle lithosphere, the peak heat flux in the delaminated area is almost the same as the flux in the non-delaminated area.

A caveat is that we used the same amplitude for the initial orogenic lithosphere in all cases. However, if the mantle lithosphere is thick, it is probable that the orogenic lithosphere is also thick, which may affect the negative buoyancy of the delaminated area. Thus, we calculate the surface heat flux for the $5M_{\oplus}$ planet with a different value A_{oro} in the initial state. Fig. 29 shows the heat flux at 10 Myr for $D_{\rm lith}$=113 km. Even though the additional orogenic mantle lithosphere thickens, the surface heat flux is relatively unchanged.

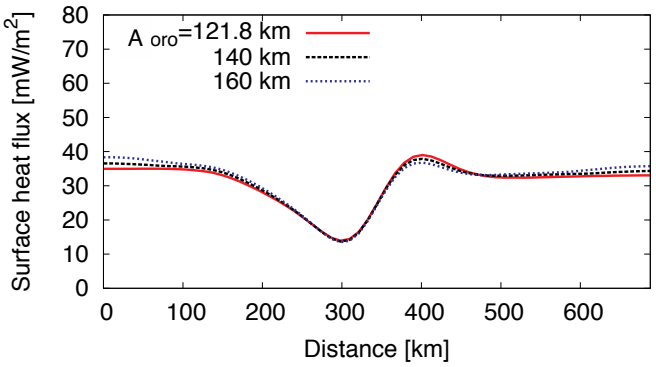

Figure 29: Surface heat flux for a $5M_{\oplus}$ planet at 10 Myr for different amplitudes of the orogenic lithosphere thickness. The thickness of the mantle lithosphere in the non-orogenic area is 113 km. Heat flux does not change largely even though the thickness of the orogen is different.

These calculations show that the magnitude of the convection in the delaminated area is important for the heat transfer facilitated by the delamination. The thermal Rayleigh number for the $5M_\oplus$ planet with a 113-km-thick mantle lithosphere is 9.6×10^4. Thus, in order to induce effective heat emission through delamination, a thermal Rayleigh number of more than 10^5 is required for our model. If the mantle lithosphere is around 100 km thick, $5M_\oplus$ is the upper limit of the mass. However, if the mantle lithosphere is thin at around 70 km, the upper limit increases to $7M_\oplus$ (Fig. 25).

In this work, we do not consider the compressibility of the mantle. In the case of the super-Earths, effect of pressure becomes large (Miyagoshi et al., 2014), which should be the further discussion.

6 Discussion

6.1 Relationship of each topic

Except for the Earth, one of the most typical heat source is the tidal heating. Of the active celestial bodies in our solar system, Io, Enceladus, Triton and Europa have more or less tidal heat as the heat source. Thus, for the consideration of the active bodies, tidal heating cannot be ruled out. Io and Europa can generate large heat by the equilibrium tidal heating state. On the other hand, Enceladus should not be in steady state, which makes Enceladus more attractive satellite. Here, we considered non-equilibrium tidal heating of Enceladus first. Ceres do not have large tidal heating due to the long orbital distance. Instead, Rayleigh-Taylor instability is estimated as the activation mechanism of Ceres. This type of activity is also important for the terrestrial planet out of the solar system, which is considered as the delamination process in super-Earths. However, beyond our solar system, terrestrial planets which are under strong tidal heating exist, which is like Io. Tidal theory and calculation methods have been developed at the icy satellite researches. Thus, we applied these method to the tidal heating of extrasolar planets.

In this work, tidal heating of Enceladus is related to the extrasolar planet around M star. Calculation method for heating rate shown by Eq. (6) is used at exoplanet tidal heating in Eq. (71). Temperature in each layer of Enceladus is calculated by the heat balance by conduction and interior heat caused by tide (Eq. (2)). This principle is applied to the calculation of mantle temperature in exoplanets (Eq. (42)). Thus, it is common that the interior temperature changes by the heat balance and interior heat. However, in the case of Enceladus, thickness of the icy layer also changes, which can be written by Eq. (10). On the other hand, in the case of exoplanet, mantle does not separate from the core, which is the difference between Enceladus and rocky planet.

Diapirism of Ceres is based on the Rayleigh-Taylor instability, and the main theory

is written by Eqs. (32)-(35). This equations are applied to the delamination shown by Eqs. (88)-(91) although delamination theory contains dissipation number as the effect of viscous dissipation. However, we note that effect of pressurization is large for the interior dynamics of super-Earths (Miyagoshi et al., 2014), which is not taken into account in this work. Thus, this can be the difference between small body like Ceres and large body like super-Earths.

In the calculation of orbital change by tidal heating, different equations are used between Enceladus and extrasolar planet. Orbital change of extrasolar planet in our work considers time change of orbital distance. On the other hand, we ignored the change of orbital distance (change of mean motion) at the heating of Enceladus. This equation adopted for Enceladus is valid for relatively short time evolution (around a few hundred million years), which is less than the time scale of extrasolar planets (around a few billion years). Thus, mean motion change is small at Enceladus. As mentioned section 2.3.3, change of orbital distance by the resonance is not so large, and thus tidal heating changes little by the orbit distance. If we consider the long time scale of Enceladus, our approximated equation becomes invalid.

6.2 Heat sources other than radio active decay and tide

In rocky and icy bodies, two main heat sources are radioactive decay and tidal heating. Thus, we considered the detailed effect of the heat generated by the two sources. Although it is difficult to find good heat sources other than tide and radio active decay, there are some mechanisms to produce heat. In the case of Enceladus, importance of serpentinization has been mentioned in Section 2.10. Although magnitude of serpentinization is estimated to be much smaller than the radiogenic heat (Vance et al., 2007), new observational results by Cassini motivate us to reconsider the effect of hydrothermal process

in Enceladus' core (Sekine et al., 2014; Postberg et al., 2014). In addition to Enceladus, liquid water should directly contact with the rocky mantle at Europa. Thus, hydrothermal process may work at Europan ocean floor.

For the relatively large bodies such as planets and satellites, accretion energy is suggested as the heat sources. By the change of kinetic energy, heat produced at the accretion stage may be important for some bodies. We have to keep in mind that current heating depends on the initial condition. For example, whether or not core is hydrated affects the tidal heating. However, it is estimated that some fraction of the accretional energy was released to space effectively (Hussmann et al., 2006) because the heat production was limited to the surface region. The contribution of this energy to the heat source at later stage evolution depends on the magnitude of overturn to incorporate the heat inside and the surface environments to facilitate radiation of heat to space.

Alternatively, Joule heating may be induced by the magnetic field now (Hand et al., 2011). However, in order to activate the Joule heating, interior should melt because Joule heating is induced by the electrical current. Thus, we have to consider again the heat sources to produce and maintain the interior ocean. Moreover, although it works as the additional heat, the magnitude of Joule heat is not so large enough to stabilize the ocean (Hand et al., 2011).

In the case of Europa, some researches conclude that elliptical orbital tidal heating and radiogenic heat are sufficient to maintain a subsurface ocean (e.g., Hussmann et al., 2002; Hussmann and Sporn, 2004). However, at small bodies such as Enceladus, sole orbital tidal heating is difficult to maintain the ocean sufficiently unless the past eccentricity is much larger than the current value (Běhounková et al., 2012). At Enceladus, tidal dissipation at different area may be important. Tidal heat is mainly produced in the icy mantle because ice has moderate viscosity to induce frictional heat. However, other area

also dissipates. Especially ocean dissipation is suggested to maintain the ocean (Tyler, 2009, 2011, 2014; Chen et al., 2014; Matsuyama, 2014). Recent gravity analysis indicates that Enceladus' core has smaller density than dry rock (Iess et al., 2014). It is probable that Enceladus' core has some fraction of water, which may induce the tidal dissipation at the surface area of the core. Considering the possibility of other area dissipation, we cannot rule out that Enceladus' main dissipation area is different from Europa. One caveat on Enceladus is that, even though the core has large dissipation, equilibrium heating rate limits the amount of total tidal heat generated in whole Enceladus (Meyer and Wisdom, 2007). Thus, Enceladus should be in non-equilibrium state. If additional heat is generated in the core by tides, eccentricity decreases drastically, and thus heating rate should be reduced soon. Although core tide can change the temperature distribution, it is uncertain that ocean can be maintained at Enceladus.

Other type of tidal heating can be important hypothesis for the additional heat sources. In this work, although we considered tidal heating by elliptical orbit of Enceladus and extrasolar planet, tidal heating is also induced by other orbital condition. This type of tidal heating is free from the equilibrium heating rate required at the eccentricity tide of Enceladus. One is the obliquity of the body (Tyler, 2009, 2011). When the orbiting body has obliquity, tidal bulge moves along latitude, which generates frictional heat. Obliquity tide is suggested as the effective heat source in Triton (Nimmo and Spencer, 2014) although it is insufficient for Enceladus (Chen and Nimmo, 2011). Physical libration is also the mechanism to generate large dissipation (e.g., Nimmo et al., 2014). These types of tide can be applied to extrasolar planets. In the future, it is expected that many kinds of planets which are different from ones in our solar system can be found. Some planets may interact with central stars like the interaction between icy satellite and large planet in the solar system.

6.3 Habitability of active bodies

One interesting aspect about active bodies is the habitability of lives. Typically, habitability of celestial bodies is discussed from the orbital distance from the central star. This distance is called habitable zone, which is defined by the area where liquid water can exist on the surface (e.g., Kasting et al., 1993). However, stability of the surface water is complicated, and thus habitable zone is not simply derived. For the inner edge of the habitable zone, Kasting et al. (1993) mainly consider the water loss by photolysis of vapor in stratosphere and the escape of hydrogen. Revised estimation by Kopparapu et al. (2013) is also based on this principle, which result in 0.99 AU as the inner edge. Recently, 3D calculation with the cloud distribution has been performed (Leconte et al., 2013), and inner edge was derived at 0.95 AU. Distance of habitable zone may change with the planetary system because orbital state of the planet depends on the central star. In the case of M star, habitable planet should be tidally-locked, which results in different climate from the Earth-like (fast rotating compared with orbiting) planets. Habitable zone of M type star is calculated with 3D dimension by Yang et al. (2013). They found that cloud around substeller point increases planet's albedo and reduces the surface temperature, which results in the stabilization of the climate because higher insolate temperature produce more cloud. Due to the climate stability, habitable zone of M stars extends (Yang et al., 2013). However, calculations by Leconte et al. (2013) indicate that cloud destabilizes climate, because the number and size of cirrus cloud increase with increasing the surface temperature and the generated cirrus cloud warms the surface by greenhouse effect. The effect of cloud to planet's climate remains controversy, and thus more work is required (Kasting, 2013). Cloud works to reduce the surface temperature by increasing the albedo, while it works to warm the surface of the planet by greenhouse effect. It is difficult to determine which effect becomes larger, which may depend on cloud type and

formation. It is probable that climate condition changes with each planetary system and planet, which should result in different habitable zone at each planetary system. Anyway, habitable zone should be considered further including atmospheric researches.

If extraterrestrials have the same mechanism to maintain their lives with terrestrial lives, another aspects constrain the habitable zone of the planetary system. For the stability of the environment appropriate for lives, plate tectonics may be important. Barnes et al. (2009) propose the additional constraint of habitable zone from the surface heat flux and surface activity. Io is the very active satellite, but magnitude of activity is too high for lives. On the other hand, Barnes et al. (2009) consider that the heat flux of current Mars is too small to induce the tectonic activity. Thus, surface heat flux suitable for habitability should be between the flux of Io and Mars. In this work, we considered orbital and thermal habitability, and Martian-sized planet can be habitable around M stars. Interactions with ocean and atmosphere are ignored in this work, which are the future studies. Surface ocean is very important factor for habitability. So far, although composition is different, the Earth and Titan have surface ocean (lake may be appropriate for Titan). In order to stabilize the surface ocean, thick atmosphere is required. For the coupled tidal heating in this work, we referenced the thermal model of Io. Atmospheric and ocean researches on Titan may constrain the exoplanets like the case of Io.

Habitable zone is an important factor to estimate the habitable body, especially the body is outside of the solar system. However, we cannot always say that celestial bodies outside of the habitable zone is not habitable. If the planets and satellites are beyond the snow line (the inner limit where ice can condense without evaporation.), surface can be covered with ice and liquid water may exist subsurface of the body. In our solar system, considering the subsurface liquid water, Europa, Titan and even Pluto may be habitable bodies, for example tidal dissipation of in the surface ocean.

However, habitability is not defined only from physical condition, and chemical and biological aspects are necessary. For example, in addition to liquid water, McKay et al. (2014) suggest that energy, carbon and nitrogen are key factors for the lives. Considering these factors, because all conditions can be attained at Enceladus, McKay et al. (2014) conclude that Enceladus is the most interesting object for habitability. One caveat is whether interior structure suited for habitability is maintained for a long time is uncertain. As shown in our work, Enceladus has large possibility of the drastic evolution process. Shapiro and Schulze-Makuch (2009) mention that Titan can be more important for habitability.

6.4 Link between global process and local process

In this work, we discussed tidal heating as a global physical process, and diapirism and delamination as relatively localized activities. When we consider a global system, local processes are usually simplified or sometimes ignored. In the case of tidal heating in this work, we assume that each interior layer is spherical and physical values such as density are independent of latitude and longitude. On the other hand, at the local process study, orbital evolution is not taken into account.

We sometimes regard each body as a point mass without structure, and sometimes as a large structure without orbital change. These assumptions are reasonable if each process does not largely affect (for example time and area scales are different, or orbital evolution is small). However, we have to be careful in some cases because physical processes in real celestial bodies are not independent from other scale dynamics. In the case of Enceladus, local heterogeneity may affect the global tidal evolution. Magnitude of tidal dissipation will change if non-spherical structure is assumed, which may affect the orbital evolution. If plate tectonics or/and compositional convection occurs in extrasolar planets,

tidal heating also changes because thickness of the surface lithosphere changes. In the case of Ceres, local process may be affected by global process. The place where Ceres is accreted is not known, and some researches suggest that Ceres have migrated from Kuiper belt area (McKinnon, 2008, 2012). Of course, it is largely probable that Ceres stays the current orbit for a long time. However, if Ceres moved from other place, surface temperature must be largely different from the current surface temperature. As can be seen in our work, diaprism of Ceres depends on Ceres' surface temperature. Interior temperature also changes by the surface temperature because magnitude of heat transfer changes. Although delamination process occurs at localized area, thickness of lithosphere is determined by large scale convection. Thus, even though the size of super-Earth is the same, different interior evolution and activities are probable, which results in different orbital evolution as a feedback.

Coupling of global and local activities are very complicated not only by the numerical but physical reasons. Tidal theory can be coupled to the orbital theory by the spherical shell structure via Love number. If we cannot use the global Love number, we have to consider the first principle of energy conservation or stress field. In that case, we cannot use analytic method, and have to calculate each area constructing grid space. For the Galilean satellites, tidal dissipation in non-spherical shell ice are performed by A et al. (2014). This effort is very complicated even only for the tidal dissipation, and thus is a wonderful work. Whether these method can be applied to thermal-orbital evolution is uncertain. At least, complicated process increases more than the work by A et al. (2014). Thus, interaction between global and local activities can be the challenging work for future study.

7 Conclusion

7.1 Conclusions of each topic

7.1.1 Non-equilibrium tidal heating for the stability of a subsurface ocean

Enceladus shows strong evidence that the magnitude of heating is not in steady state. We conducted coupled calculations assuming a Burgers rheology and ammonia content in the H_2O shell. The heating state of Enceladus depends on parameters such as viscosity, core size and the Q-value of Saturn. We analyzed the heating state by using a broad range of different parameter sets. If the Q-value of Saturn is 18,000-23,000 and the core size is less than 161 km, episodic heating modes, in which heating rate and ice thickness change cyclically, are induced for some rheological parameter ranges.

In the episodic heating state, tidal heating rates oscillate up to 1.5 GW. Thus, we cannot explain the anomalous heat flux by our coupled calculation. The minimum value of eccentricity is 0.0045, which is consistent with the observed Enceladus' eccentricity. A major result of our calculation is that ice thickness, heating rate and consequently activity at the surface can change periodically. In our preferred scenario episodes of enhanced tidal heating, which can occur with a period of a few hundred million years, might trigger additional processes near the surface by providing the right amount of "background heating" in the ice shell. Evidence for enhanced heating rates in the past can be found at different locations on Enceladus, also at high latitudes. The current activity at the south pole might be an indirect consequence of episodic heat pulses. Although a global subsurface ocean cannot be ruled out completely, the observed present surface state has been interpreted as a consequence of a localized partial ocean. This partial ocean may thus be a result from relatively recent episodic ice thickness (i.e., ocean thickness) changes.

In our calculations, ocean thickness is a few kilo meters at most, which is smaller than the observational implication ($\sim$10 km). Temperature of Enceladus' jet is higher than the

eutectic point of ammonia-ice. New observational results imply that core size and density are different from the convectional models. Thus, another heat process such as serpentinization may be induced, which can be additional heat if any. The state of Enceladus core can be the important future work for the activity and stability of a subsurface ocean.

7.1.2 Possibility of the compositional diapirism and future mission for Ceres

To explore the possibility that compositional diapirism is the origin of the dark spots and water vapor emission in the mid-latitude regions of Ceres, we performed numerical calculations on the crust stability and rising diapir. If the rock density in the crust is 2700 kg m^{-3}, the upper limit of the critical temperature under which the crust is stable for a few billion years is around 180 K. In the case that the density of the rock is nearer that of Vesta (3440 kg m^{-3}), the long-term critical temperature is lower, at around 160 K. The surface temperature of Ceres is around 180 K in the equatorial region and 170 K in the mid-latitude regions (Bland, 2013). Thus, at mid-latitude, the crust can be stable if the rock is relatively low density. By contrast, in the equatorial region, the crust subsides regardless of the rock density.

Assuming that the crust is stable and that a perturbation is generated, the generated diapir reaching the surface is dependent on the surface temperature because the viscosity contrast is controlled by the temperature distribution. When the surface temperature is around 170 K, the diapir can reach the surface. The time taken to reach the surface depends on the amplitude of the initial perturbation and is inversely proportional to the crustal thickness. If a relatively large perturbation is generated, the diapir can reach the surface even when the crust is just 10-20 km thick, which is highly likely according to thermal history calculations (Castillo-Rogez and McCord, 2010). If the surface temperature is low at 150 K, the diapir cannot reach the surface within the age of the solar system even when the crustal thickness is large ($\sim$60 km). We conclude that a diapir-induced

morphology cannot appear in the polar regions, which is one reason that dark spots and vapor emission are observed only at mid-latitude. These calculations show that diapirism is a possible origin of the observed dark spots of Ceres, alongside the cryovolcanism hypothesis. When the Dawn mission observes the surface of Ceres, morphologies generated by compositional diapirism like on Triton may be observed (Schenk and Jackson, 1993).

If the ice in the crust and diapir contains impurities, its melting point will be lower, which in turn may induce vapor emission. However, in our calculations, a sufficient temperature change is not induced due to the low thermal Rayleigh number and the large time scale associated with diapirism. Therefore, we could not show that the diapir melts the ice; however, as an alternative mechanism for the vapor emission, sublimation has been suggested (Küppers et al., 2014). If new pure ice is pushed to the surface by the diapir, this is a valid explanation for the localized vapor emission.

As mentioned in Section 3.2, one caveat to our argument is that we did not consider exogenic effects on the crust stability. Castillo-Rogez and McCord (2010) pointed out that impacts will likely affect the gravitational stability of the crust. Many impacts could destroy the crust of Ceres. However, if the crust is relatively thick, it might be preserved. In addition, the subsidence of the crust by impacts might occur not at a global level but at a local level. All of these questions will be answered by future observations.

Due to the lack of precise observations, we cannot say with certainty whether the dark spots are formed through cryovolcanism, diapirism or another mechanism. We can expect that the Dawn probe can elucidate the surface and internal states of Ceres.

7.1.3 Importance of coupling calculation for exoplanets

Through thermal and orbital coupled calculations, it was found that two types of evolution are probable for Martian-sized planets in the habitable zones of M stars. One type is the runaway cooling state in which the radiated heat flux is larger than the tidal heating,

decreasing the mantle temperature through positive feedback. As a result of the cooling, convection in the mantle is reduced and the planet becomes rigid. The other type of evolution is the hot state. In a hot state, tidal heating exceeds the radiated heat flux and runaway heating occurs. However, melt in the mantle reduces the tidal heating by decreasing the viscosity and shear modulus, and an equilibrium state is reached. The eccentricity and orbital distance of hot state planets do not change significantly due to the large Q value caused by the melt. Thus, the planet in hot state can stay the habitable zone for more than a few billion years. In the equilibrium state, the heat flux is in the range suitable for habitability (Barnes et al., 2009). We performed the calculations and by changing many parameters, found that those that have the most significant effect on the evolution are the mass of the star and the initial value of the eccentricity. If the mass of the star is less than $0.2M_{\odot}$ and the initial eccentricity is more than 0.2, the planet should be in a hot state (Fig. 23). A hot state planet contains melt in the mantle; thus, a magnetic field may be induced. An intrinsic magnetic field, however, is unlikely to occur because the mantle temperature is large and sufficient heat is not transported from the core.

Among extrasolar planets, super-Earths in particular are considered for habitability. In the case of a super-Earth, our simple structural model is not valid and the effects of pressure are likely large (Wagner et al., 2012). We must also consider the phase of the core because the core may be solidified by the large pressure. However, our simple coupled calculations provide the first step towards these more complicated and accurate analyses of extrasolar planets.

7.1.4 Possibility of delamination at super-Earths

By applying a simple Earth-based model, we analyzed the delamination process in super-Earths for the first time. The pressure dependent rheology, viscosity, thermal expansion and thermal diffusivity decrease the Rayleigh numbers of planets with large mass even

though they have higher gravity, which reduces the vigorousness of the convection in the Moho area. In our calculations, for a planet of $5M_{\oplus}$, delamination occurs due to the density contrast between the mantle lithosphere and asthenosphere. However, the delaminated area is narrow ($\sim$100 km) and a large temperature gradient is not induced while the Moho temperature rises sufficiently and around 200 km of delamination in width occurs for a $1M_{\oplus}$ planet. In our geometric and rheological model, the delamination process can transfer more heat than the conduction in the lithosphere if the thermal Rayleigh number is significantly larger than 10^5. Thus, delamination is unlikely to transfer large quantities of heat if the mantle lithosphere is around 100 km in thickness and planet's mass is greater than $5M_{\oplus}$.

In terms of plate tectonics and mantle dynamics, the activity found in large planets strongly depends on the calculation model used (Stamenković and Breuer, 2014). This is also true for the delamination process. For example, if we consider pressure independent rheologies, the viscosity largely decreases in large super-Earths because the adiabatic interior temperature becomes high due to the increase in gravity. The geometry of the numerical calculation (2D or 3D, and scale ratio) may also affect the results.

In this work, we applied the Earth model to planets with large mass. However, it is highly probable that extrasolar planets have different heat sources to the Earth. If the planet orbits near the central star, it will likely have strong tidal heating due to the gravitational interaction with the star like the Jovian satellite Io (Segatz et al., 1988). Because strong tidal heating can melt large parts of interior structures, other structural models should be considered for future works concerning magma ocean interiors, for example. If the mantle contains melts, the viscosity is far lower (Moore, 2003), which results in vigorous convection even in large planets. Thus, for super-Earths, the delamination process is an important activity, so further, more detailed research is required that includes other

types of rheology and internal structure models.

7.2 For the understanding of our environment

In this thesis, we saw the individual problems on Enceladus, Ceres and exoplanets. For such icy bodies and extrasolar planets, ideas and theories derived from Earth science are essential because the Earth is the most studied planet. Regardless of its uniqueness such as plate tectonics and surface ocean (atmosphere), the Earth is the most familiar environment to us. Maybe, the next should be the Moon. This work mainly discuss the topic outside of our environment and did not directly discuss the two bodies. However, coupled calculation or tidal heating in this work can be applied to the thermal evolution of the Moon. The Moon is also a synchronously rotating body, and thus coupled calculation can be possible. Tidal evolution of the Moon is the major topic for its evolution. Compared with Enceladus and exoplanets, we have a lot of observational data by some probes of the Moon, which is available to give a constraint in tidal evolution.

As mentioned in introduction, extrasolar terrestrial planets can be compared directly to the Earth's environment. Plate tectonics controversy at heavy planets has been mentioned in Section 5.2. Although this controversy is chaotic now, it contributes to the understanding of the plate tectonics. Tectonic activity may occur at icy bodies. Katternhorn and Prockter (2014) point out that appearance of new surface of Europa is compensated by the subduction of the surface ice. Europa has young surface which appeared in the recent past. Expansion of Europa is implausible (Kattenhorn and Prockter, 2014). Thus, if new surface appeared, old surface should be removed. However, surface feature which shows removal has not been found. Kattenhorn and Prockter (2014) suggest band morphology is the subduction area. Mobile surface is also suggested at Enceladus (Barr, 2008). By the future observations, icy bodies may be able to join the plate tectonics controversy.

Acknowledgement

I thank K. Kurita, H. Hussmann and F. Sohl for helpful discussions and advices. F. Nimmo gave me useful comments for the tidal heating of Enceladus. This work is supported by JSPS research fellowship.

References

A, G., Wahr, J., Zhong, S., 2014. The effects of laterally varying icy shell structure on the tidal response of Ganymede and Europa. J. Geophys. Res. 119, 659-678.

Acuña, et al., 1999. Global Distribution of Crustal Magnetization Discovered by the Mars Global Surveyor MAG/ER Experiment. Science, 284, 790-793

A'Hearn, M. F., Feldman. P. D., 1992. Water vaporization of Ceres. Icarus 98, 54-60.

Alterman, Z., Jarosch, H., Pekeris, C., 1959. Oscillations of the Earth. Proc. R. Soc. London A 252, 80-95.

Arakawa, M., Maeno, N., 1994. Effective viscosity of partially melted ice in the ammonia-water system. Geophys. Res. Lett. 21, 1515-1518.

Barnes, R., Jackson, B., Greenberg, R., Raymond, S. N., 2009. Tidal limits to planetary habitability. Astrophys J. 700, L30.

Barnes, R., Raymond, S. N., Jackson, B., Greenberg, R., 2008. Tides and the Evolution of Planetary Habitability. Astrobiology 8, 557-568.

Barnes, et al., 2010. CoRoT-7b: super-Earth or super-Io? Astrophys. J. Lett. 709, L95.

Barr, A. C., 2008. Mobile lid convection beneath Enceladus' south polar terrain. J. Geophys. Res. 113, E7.

Barr, A. C., McKinnon, W. B., 2007. Convection in Enceladus' ice shell: Conditions for initiation. Geophys. Res. Lett. 34, L09292, doi: 10.1029/2006GL028799.

Běhounková, M., Tobie, G., Choblet, G., Čadek, O., 2012. Tidally-induced melting events as the origin of south-pole activity on Enceladus. Icarus 219, 655-664.

Běhounková, M., Tobie, G., Choblet, G., Čadek, O., 2013. Impact of tidal heating on the onset of convection in Enceladus's ice shell. Icarus 226, 898-904.

Besserer, J., Nimmo, F., Roberts, J. H., Pappalardo, R. T., 2013. Convection-driven compaction as a possible origin of Enceladus's long wavelength topography. J. Geophys. Res. 118, 908-915.

Bills, B. G., Nimmo, F., 2011. Forced obliquities and moments of inertia of Ceres and Vesta. Icarus 213, 406-509.

Biot, M.A., 1954. Theory of stress-strain relations in anisotropic viscoelasticity and relaxation phenomena. J. Appl. Phys. 25, 1385-1391.

Bird, P., 1978. Initiation of intracontinental subduction in the Himalaya. J. Geophys. Res. 83, 4975-4987.

Bird, P., 1979. Continental delamination and the Colorado Plateau. J. Geophys. Res. 84, 7561-7571.

Bland, M. T., 2013. predicted crater morphologies on Ceres: Probing internal structure and evolution. Icarus 226, 510-521.

Bland, M. T., Beyer, R. A., Showman, A. P., 2007. Unstable extension of Enceladus' lithosphere. Icarus 192, 92-105.

Bland, M. T., Showman, A. P., Tobie G., 2009. The orbital-thermal evolution and global expansion of Ganymede. Icarus 200, 207-221.

Bland, M. T., Singer, K. N., McKinnon, W. B., Schenk, P. M., 2012. Enceladus' extreme heat flux as revealed by its relaxed craters. Geophys. Res. Lett. 39, L17204, doi:10.1029/2012GL052736.

Breuer, D., Spohn, T., 2006., Viscosity of the Martian mantle and its initial temperature: Constraints from crust formation history and the evolution of the magnetic field. Planet. Space Sci., 54, 153-169.

Brown, R. H., Kirk, R. L., Johnson, T. V., Soderblom, L. A., 1990. Energy Sources for Triton's Geyser-Like Plumes. Science 250, 431-435.

Carry, B., Dumas, C., Fulchignoni, M., Merline, W. J., Berthier, J., Hestroffer, D., Fusco, T., Tamblyn, P., 2008. Near-infrared mapping and physical properties of the dwarf-planet Ceres. Astron. Astrophys. 478, 235-244.

Castillo-Rogez, J. C., 2011. Ceres-Neither a pours nor salty ball. Icarus 215, 599-602.

Castillo-Rogez, J., Efroimsky, M., Lainey, V., 2011. The tidal history of Iapetus: Spin dynamics in the light of a refined dissipation model. J. Geophys. Res. 116, E09008, doi:10.1029/2010JE003664.

Castillo-Rogez, J. C., McCord, T. B., 2010. Ceres' evolution and present state constrained by shape data. Icarus 205, 443-459.

Castillo-Rogez, J. C., Schmidt, B. E., 2010. Geophysical evolution of the Themis family parent body. Geophys. Res. Lett. 37, L10202.

Chan, J. P., Giauque, W. F., 1964. The Entropy of NH_3 $2H_2O$. Heat Capacity from 15 to 300°K. J. Phys. Chem. 68, 3053-3057.

Chandrasekhar, S., 1961. Hydrodynamic and Hydromagnetic Stability. Dover, Mineola, New York.

Chen, E. M. A., Nimmo, F., 2011. Obliquity tides do not significantly heat Enceladus. Icarus 214, 779-781.

Chen, E. M. A., Nimmo, F., Glatzmaier, G. A., 2014. Tidal heating in icy satellite oceans. Icarus 229, 11-30.

Collins, G. C., Goodman, J. C., 2007. Enceladus' south polar sea. Icarus 189, 72-82.

Collins, G. C., Head III, J. W., Pappalardo, R. T., Spaun, N. A., 2000. Evaluation of models for the formation of chaotic terrain of Europa. J. Geophys. Res. 105, 1709-1716.

Cook, J.C., Desch, S.J., Roush, T.L., Trujillo, C.A., Geballe, T.R., 2007. Near-infrared spectroscopy of Charon: Possible evidence for cryovolcanism on Kuiper Belt bjects. Astrophys. J. 663, 1406?1419.

Crawford, G. D., Stevenson, D. J., 1988. Gas-driven water volcanism and the resurfacing of Europa. Icarus 73, 66-79.

Czechowski, L., 2014. Some remarks on the early evolution of Enceladus. Planet. Space Sci., in press.

De La Chapelle, S., Milsch, H., Castelnau, O., Duval, P., 1999. Compressive creep of ice containing a liquid intergranular phase: Rate-controlling processes in the dislocation creep regime. Geophys. Res. Lett. 26, 251-254.

Durham, W. B., Kirby, S. H., Stem, L. A., 1992. Effects of dispersed particulates on the rheology of water ice at planetary conditions. J. Geophys. Res. 97, 20883-20897.

Durham, W. B., Kirby, S. H., Stern, L. A., 1993. Flow of Ices in the Ammonia-Water System. J. Geophys. Res. 98, 17667-17682.

Elkins-Tanton, L.T., 2005. Continental magmatism caused by lithospheric delamination.

In: Foulger, G.R., Natland, J.H., Presnall, D.C., Anderson, D.L. (Eds.), Plates, Plumes, and Paradigms. Geol. Soc. Am. Spec. Pap., vol. 388, pp. 449-462.

Fagents, S. A., 2003. Considerations for effusive cryovolcanism on Europa: The post-Galileo perspective. J. Geophys. Res. 108, E12.

Fanale, F. P., Salvail J. R., 1989. The water regime of Asteroid (1) Ceres. Icarus 82, 97-110.

Figueredo, P. H., Chuang, F. C., Rathbun, J., Kirk, R. L., Greeley R., 2002. Geology and origin of Europa's Mitten feature (Murias Chaos). J. Geophys. Res. 107, E5.

Fischer, H. J., Spohn, T. 1990. Thermal-orbital histories of viscoelastic models of Io (J1). Icarus 83, 39-65.

Foley, B. J., Bercovici, D., Landuyt, W., 2012. The conditions for plate tectonics on super-Earths: Inferences from convection models with damage. Earth Planet. Sci. Lett. 331-332, 281-290.

Fuse, C. R., S. G. Alexander, N. P. Abel, T. Wu, and G. Newstadt (2007), Obliquity Evolution of Ceres and Vesta, DPS meeting, Vol. 39, p.515.

Gaeman, J., Hier-Majumder, S., Roberts, J. H., 2012. Sustainability of a subsurface ocean within Triton's interior. Icarus 220, 339-347.

Gavrilov, S. V., Zharkov, V. N., 1977. Love Number of the Giant Planet. Icarus 32, 443-449.

Gessmann, C. K., Wood, B. J. 2002. Potassium in the Earth's core? Earth Planet. Sci. Lett., 200, 63-78.

Giese, B., Cassini Imaging Team, 2010. The topography of Enceladus. In: European Planetary Science Congress 2010, p. 675.

Giese, B., Wagner, R., Hussmann, H., Neukum, G., Perry, J., Helfenstein, P., Thomas, P., 2008. Enceladus: An estimate of heat flux and lithospheric thickness from flexurally supported topography. Geophys. Res. Lett. 35, L24204, doi:10.1029/2008GL036149.

Göğüs, O. H., Pysklywec R. N., 2008 a. Mantle lithosphere delamination driving plateau uplift and synconvergent extension in eastern Anatolia. Geology 36, 723-726.

Göğüs, O. H., Pysklywec R. N., 2008 b. Near-surface diagnostics of dripping or delaminating lithosphere. J. Geophys. Res. 113, B11404.

Goldreich. P., Soter, S. 1966. Q in the solar systemIcarus, 5, 375-389.

Goldsby, D. L., Kohlstedt, D. L., 2001. Superplastic decoration of ice: Experimental observations. J. Geophys. Res. 106, 11017.

Gorda, S. Y., Svechnikov, M. A. 1999. Empirical L-M, R-M, and M-T_{eff} relations for main-sequence stars: Components of close binary systems and low-mass stars. Astronomy Reports 43, 521-525.

Greeley, R., et al., 2000. Geologic mapping of Europa. J. Geophys. Res. 105, 22559-22578.

Green, D. H., Cooper, R. F., 1993. Dilatational Anelasticity in Partial Melts: Viscosity, Attenuation, and Velocity Dispersion. J. Geophys. Res. 98, 19807-19817.

Grott, M., Breuer, D., 2008 a. The evolution of the martian elastic lithosphere and implications for crustal and mantle rheology. Icarus 193, 503-515.

Grott, M., Breuer, D. 2008 b. Constraints on the radiogenic heat production rate in the Martian interior from viscous relaxation of crustal thickness variations. Geophys. Res. Lett. 35, L05201

Hall, P. S., Kincaid, C., 2001. Diapiric flow at subduction zones: A recipe for rapid transport. Science 292, 2472-2475.

Han, L., Showman, A. P., 2005. Thermo-compositional convection in Europa's icy shell with salinity. Geophys. Res. Lett. 32, L20201.

Hand, K. P., Khurana, K. K., Chyba, C. F., 2011. Joule heating of the south polar terrain on Enceladus. J. Geophys. Res. 116, E04010.

Hansen, V. L., 2003. Venus diapirs: Thermal or compositional?. Geol. Soc. Am.Bull. 115, 1040-1052.

Hedman, M. M., Gosmeyer, C. M., Nicholson, P. D., Sotin, C., Brown, R. H., Clark, R. N., Baines, K. H., Buratti, B. J., Showalter, M. R., 2013. An observed correlation between plume activity and tidal stresses on Enceladus. Nature 500,182?184.

Henning, W. G., O'Connell, R. J., Sasselov, D. D., 2009. Tidally heated terrestrial exoplanets: viscoelastic response models. Astrophys. J. 707, 1000.

Hillier, J., Squyres, S. W., 1991. Thermal stress tectonics on the satellites of Saturn and Uranus. J. Geophys. Res. 96, 15665-15674.

Howett, C., Spencer, J., Pearl, J., Segura, M., 2011. High heat flow from Enceladus' south polar region measured using 10–600 cm^{-1} Cassini/CIRS data. J. Geophys. Res. 116, E03003, doi:10.1029/2010JE003718.

Hsu, H. W., Postberg, F., Kempf, S., Trieloff, M., Burton, M., Roy, M., ⋯ Srama, R., 2011. Stream particles as the probe of the dust-plasma-magnetosphere interaction at Saturn. J. Geophys. Res 116(9).

Hussmann, H., Sohl, F., Spohn, T., 2006. Subsurface oceans and deep interiors of medium-sized outer planet satellites and large trans-neptunian objects. Icarus 185, 258-273.

Hussmann, H., Spohn, T., 2004. Thermal-orbital evolution of Io and Europa. Icarus 171, 391-410.

Hussmann, H., Spohn, T., Wieczerkowski, K., 2002. Thermal Equilibrium States of Europa's Ice Shell: Implications for Internal Ocean Thickness and Surface Heat Flow. Icarus 156, 143-151.

Iess, L., Stevenson, D. J., Parisi, M., Hemingway, D., Jacobson, R .A., Lunine, J. I., Nimmo, F., Armstrong, J. W., Asmar, S. W., Ducci, M., Tortora, P., 2014. The gravity field and interior structure of Enceladus. Science 344,78?80.

Jackson, B., Barnes, R., Greenberg, R., 2008. Tidal heating of terrestrial extrasolar planets and implications for their habitability. MNRAS 391, 237-245.

Jackson, I., Fitz Gerald, J. D., Faul, U. H., Tan, B. H.. 2002. Grain-size-sensitive seismic wave attenuation in polycrystalline olivine. J. Geophys. Res. 107, B12

Joshi, M. M., Haberle, R. M., Reynolds, R. T., 1997. Simulations of the Atmospheres of Synchronously Rotating Terrestrial Planets Orbiting M Dwarfs: Conditions for Atmospheric Collapse and the Implications for Habitability. Icarus 129, 450-465.

Karato, S., 2011. Rheological structure of the mantle of a super-Earths: Some insights from mineral physics. Icarus 212, 14-23.

Karato, S., 2014. Some remarks on the models of plate tectonics on terrestrial planets: From the view-point of mineral physics. Tectonophysics 631, 4-13.

Kargel, J. S.. Croft, S. K., Lunine, J. I., Lewis, J. S., 1991. Rheological properties of ammonia-water liquids and crystal-liquid slurries: Planetological applications. Icarus 89, 93-112.

Kasting, J. F., Catling, D., 2003. Evolution of a habitable planet. Annu. Rev. Astron. Astrophys. 41, 429-63.

Kasting, J. F., Harman, C. E., 2013. Inner edge of the habitable zone. Nature 504, 221-223.

Kasting, J. F., Whitmire, D. P., Reynolds, R. T., 1993. Habitable zones around main sequence stars. Icarus 101, 108-128.

Kattenhorn, S. A., Prockter, L. M., 2014. Evidence for subduction in the ice shell of Europa. Nature geosci. 7, 762-767.

Kaula, W.M., 1964. Tidal dissipation by solid friction and the resulting orbital evolution. Rev. Geophys. 2, 661-685.

Khurana, K. K., Jia, X., Kivelson, M. G., Nimmo, F., Schubert, G., Russell, C. T., 2011. Evidence of a Global Magma Ocean in Io ' s Interior. Science 332, 1186-1189.

King, T. V. V., Clark, R. N., Calvin, W. M., Sherman, D. M., Brown, R. H., 1992. Evidence for ammonium-bearing minerals on Ceres. Science 255, 1551-1553.

Kite, E. S., Manga, M., Gaidos, E., 2009. Geodynamic and rate of vocalism on massive Earth-like planets. Astrophys, J. 700, 1732-1749.

Kivelson, M. G., Khurana, K. K., Russel, C. T., Volwerk, M., Walker, R. J., Zimmer, C., 2000. Galileo Magnetometer Measurements: A Stronger Case for a Subsurface Ocean at Europa. Science 289, 1340-1343.

Kopparapu, et al. 2013. Habitable zones around main-sequence stars: new estimates. Astrophys. J. 765, 131.

Korenaga, J., 2010. On the likelihood of plate tectonics on super-Earths: Does size matter? Astrophys. J. Lett. 725, L43-L46.

Küppers, M., et al., 2014. Localized sources of water vapor on the dwarf planet (1) Ceres. Nature 505, 525-527.

Lainey, V. et al., 2012. Strong tidal dissipation in Saturn and constraints on Enceladus ' thermal state from astrometry. Astrophys. J., 752.

Lebofsky, L. A., 1978. Asteroid 1 Ceres- Evidence for water of hydration. Mon. Not. R. Astron. 182, 17-21.

Leconte, J., Forget, F., Charnay, B., Wordsworth, R., Pottier, A., 2013. Increased insolation threshold for runaway greenhouse processes on Earth-like planets. Nature 504, 268?71.

Léger, et al. 2009. Transiting exoplanets from the CoRoT space mission VIII. CoRoT-7b: the first super-Earth with measured radius. Astronomy. Astrophys. 506, 287-302.

Léger, et al. 2011. The extreme physical properties of the CoRoT-7b super-Earth. Icarus 213, 1-11.

Li, J.-Y, McFadden, L. A., Parker, J. W., Young, E. E ., Stern, S. A., Thomas, P. C., Russell, C. T., Sykes, M.V., 2006. Photometric analysis of 1 Ceres and surface mapping from HST observations. Icarus 182, 143-160.

Lorenz, R. D., Shandera, S. E., Physical property of ammonia-rich ice: Application to Titan. Geophys. Res. Lett. 28, 215-218.

Lopes, R. M. C., et al., 2007. Cryovolcanic features on Titan's surface as revealed by the Cassini Titan Radar Mapper. Icarus 186, 395-412.

Malamud, U., Prialnic, D., 2013. Modeling serpentinization: Applied to the early evolution of Enceladus and Mimas. Icarsu 225, 763-774.

Matson, D. L., Castillo, J. C., Lunine, J., Johnson, T. V., 2007. Enceladus ' plume: Compositional evidence for a hot interior. Icarus 187, 569?573.

Matson, D. L., Castillo-Rogez, J. C., Davies, A. G., Johnson, T. V., 2012. Enceladus: A hypothesis for bringing both heat and chemicals to the surface. Icarus 221, 53-62.

Matsuyama, I., 2014. Tidal dissipation in the oceans of icy satellites. Icarus 242, 11-18.

Mayor, M., Queloz, D., 1995. A Jupiter-mass companion to a solar-type star. Nature 378, 355-359.

McCarthy, C., Castillo-Rogez, J. C., 2013. Planetary Ices Attenuation Properties. In: Gudipati, M. S., Castillo-Rogez, J. C. (Eds.), The Science of Solar System Ices, Springer, New York, pp. 183-226.

McCord, T. B., Sotin, C., 2005. Ceres: Evolution and current state. J. Geophys. Res. 110, E05009.

McEwen, A. S., et al., 2000. Galileo at Io: Resuts from high-resolution imaging. Science 288,1193-1198.

McKay, C. P., Anbar, A. D., Porco, C., Tsou, P., 2014. Follow the plume: The habitability of Enceladus. Astrobiology 14, 352-355.

McKinnon, W. B., 2008. Could Ceres be a refugee from the Kuiper belt?, In: Asteroids, Comets, Meteors Conf., #8389.

McKinnon, W. B., 2012. Where did Ceres accrete?, In: Asteroids, Comets, Meteors Conf. #6475.

McKinnon, W. B., 2013. The shape of Enceladus as explained by an irregular core: Implications for gravity, libration, and survival of its subsurface ocean. J. Geophys. Res. 118, 1775-1788.

Meyer, J., Wisdom, J., 2007. Tidal heating in Enceladus. Icarus 188, 535-539.

Meyer, J., Wisdom, J., 2008. Episodic volcanism on Enceladus: Application of the Ojakangas–Stevenson model. Icarus 198, 178-180.

Michaut, C., Manga, M., 2014. Domes, pits and small chaos on Europa produced by water sills. J. Geophys. Res. 119, 550-573.

Milliken, R. E., Rivkin, A. S., 2009. Brucite and carbonate assemblages from altered olivin-rich materials on Ceres. Nat. Geosci. 2, 258-261.

Mitri, G., Showman, A. P., 2008. Thermal convection in ice-I shells of Titan and Enceladus. Icarus 193, 387-396.

Miyagoshi, T., Tachinami, C., Kameyama, M., Ogawa, M., 2014. On the vigor of mantle convection in super-Earths. Astrophys. J. Lett. 780:L8.

Moore, W. B., 2001. The Thermal State of Io. Icarus 154, 548-550.

Moore, W. B., 2003. Tidal heating and convection in Io. J. Geophys. Res., 108, E8.

Moore, W. B., Webb, A. A. G., 2013. Heat-pipe Earth. Nature 501, 501-505.

Morency, C., Doin, M. -P., 2004. Numerical simulation of the mantle lithosphere delamination. J. Geophys. Res. 109, B03410.

Muirhead, et al., 2012. Characterizing the cool KOIs. III. KOI 961: a small star with large proper motion and three small planets. Astrophys. J 747, 144

Murray, C. D., Dermott, S. F., 1999, Solar System Dynamics (New York: Cambridge Univ. Press).

Nagel, K., Breuer, D., Spohn, T., 2004. A model for the interior structure, evolution, and differentiation of Callisto. Icarus 169, 402-412.

Nimmo, F., Porco, C., Mitchell, C., 2014. Tidally modulated eruptions on Enceladus: Cassini ISS observations and models. Astronomical. J. 148, 46.

Nimmo, F., Spencer, J. R., 2014. Powering Triton's recent geological activity by obliquity tides: Implications for Pluto geology. in press.

Nimmo, F., Spencer, J. R., Pappalardo, R. T., Mullen., M. E., 2007. Shear heating as the origin of the plumes and heat flux on Enceladus. Nature 447, 289-291.

Nimmo, F., Stevenson, D. J., 2000. Influence of early plate tectonics on the thermal evolution and magnetic field of Mars. J. Geophys. Res. 105, 11969-11979.

Noack, L., Breuer, D., 2014. Plate tectonics on rocky exoplanets: Influence of initial conditions and mantle rheology. Planetary and Space Science, 98, 41-49.

Ojakangas, G. W., Stevenson, D. J., 1986. Episodic volcanism of tidally heated satellites with application to Io. Icarus 66, 341-358.

Ojakangas, G. W., Stevenson, D. J., 1989. Thermal state of an ice shell on Europa. Icarus 81, 220-241.

O'Neill, C., Lenardic, A., 2007. Geological consequences of super-sized Earths. Geophys. Res. Lett. 34, L19204.

O ' Neill, C., Nimmo, F., 2011. The role of episodic overturn in generating the surface geology and heat flow on Enceladus. Nature Geosci 3, 88 - 91.

O'Rourke, J. G., Korenaga, J., 2012. Terrestrial planet evolution in the stagnant-lid regime: Size effects and the formation of self-destabilizing crust. Icarus 221, 1043-1060.

Paige, D. A., Bachman, J. E., Keegan, K. D., 1994. Thermal and albedo mapping of the polar regions of Mars using Viking thermal mapper observations: 1. North polar region. J. Geophys. Res. 99, 25959-25991.

Pappalardo, R. T., Barr, A. C., 2004. The origin of domes on Europa: The role of thermally induced compositional diapirism. Geophys. Res. Lett. 31, L01701.

Pappalardo, R. T., et al., 1998., Geological evidence for solid-state convection in Europa's ice shell. Nature 391, 365-368.

Parker, J. W., Stern, S. A., Thomas, P. C., Festou, M. C., Merline, W. J., Young, E. F., Binzel, R. P., Lebofsky, L. A., 2002. Analysis of the first disk-resolved images of Ceres from ultraviolet observation with the *Hubble Space Telescope*. Astrophys. J. 123, 549-557.

Porco, C., and 24 colleagues, 2006. Cassini observes the active south pole of Enceladus. Science 311, 1393-1401.

Porco, C., DiNimo, D., Nimmo, F., 2014. How the geysers, tidal stresses, and thermal emission across the South Polar Terrain of Enceladus are related. Astronomical. J. 148, 45.

Postberg, F., Hsu, H-W., Sekine, Y., 2014. Enceladus as a hydrothermal water world. EGU General Assemby Vol. 16, 14561.

Postberg, F., Kempf, S., Schmidt, J., Brilliantov, N., Beinsen, A., Abel, B., Buck, U., Srama, R., 2009. Sodium salts in E-ring ice grains from an ocean below the surface of Enceladus. Nature 459, 1098-1101.

Postberg, F., Schmidt, J., Hillier, J., Kempf, S., Srama, R., 2011. A salt-water reservoir as the source of a compositionally stratified plume on Enceladus. Nature 474, 620-622.

Rambaux, N., Castillo-Rogez, J., Williams, J., Karatekin, O., 2010. Librational response of Enceladus. Geophys. Res. Lett. 37, L04202, doi:10.1029/2009GL041465.

Rathbun, J. A., Musser Jr., G. S., Squyres, S. W., 1998. Ice diapers on Europa: Implication for liquid water. Geophys. Res. Lett. 25, 4157-4160.

Reeh, N., Christensen, E., Meyer, C., Olesen, O., 2003. Tidal bending of glaciers: a linear viscoelastic approach. Annals of Glaciology 37, 83-89.

Reese, C. C., Solomatov, V. S., Baumgardner, J. R., Yang, W. -S., 1999 b. Stagnant lid convection in a spherical shell. Phys. Earth Planet. Inter. 116, 1-7.

Reese, C. C., Solomatov, V. S., Moresi, L. N., 1999 a. Non-Newtonian Stagnant Lid Convection and Magmatic Resur facing on Venus. Icarus 139, 67-80.

Riley, J., Hoppa, G. V., Greenberg, R., Tufts, B. R., Geissler, P., 2000. Distribution of chaotic terrain on Europa. J. Geophys. Res. 105, 22599-22615.

Rivkin, A. S., Volquardsen, E. L., Clark, B. E., 2006. The surface composition of Ceres: discovery of carbonates and iron-rich clays. Icarus 185, 563-567.

Rivkin, A. S., et al., 2011. The surface composition of Ceres. Space Sci. Rev. 163, 95-116.

Roberts, J., Nimmo, F., 2008. Tidal heating and the long-term stability of a subsurface ocean on Enceladus. Icarus 194, 675-689.

Robuchon, G., Choblet, G., Tobie, G., Čadek, O., Sotin, C., Grasset, O., 2010. Coupling of thermal evolution and despinning of early Iapetus. Icarus 207, 959-971.

Rosenberg, C. L., Handy, M. R., 2005. Experimental deformation of partially melted granite revisited: implications for the continental crust. J. metamorphic Geol. 23, 19-28.

Roth et al., 2014. Transient Water Vapor at Europa ' s South Pole. Science 343, 171-174.

Rousselot, P., Jehin, E., Manfroid, J., Mousis, O., Dumas, C., Carry, B., Marboeuf, U., Zucconi, J. M., 2011. A search for water vaporization on Ceres. Astron. J. 142. 1-6.

Rubin, M. E., Desch, S. J., Neveu, M., 2014. The effect of Rayleigh-Taylor instabilities on the thickness of undifferentiated crust on Kuiper Belt Objects. Icarus 236, 122-135.

Rudman, M., 1992. Two-phase natural convection: implications for crystal settling in magma chambers. Phys. Earth Planet. inter. 72, 153-172.

Russell, C. T., et al., 2012. Dawn at Vesta: Testing the protoplanetary paradigm. Science 336, 684-686.

Sabadini, R., Vermeersen, B., 2004. Global Dynamics of the Earth: Applications of Normal Mode Relaxation Theory to Solid-Earth Geophysics. Kluwer Academic Publishers, Dordrecht.

Scalo, et al., 2007. M Stars as Targets for Terrestrial Exoplanet Searches And Biosignature Detection. Astrobiology 7, 85-166.

Schenk, P., Jackson, M. P. A., 1993. Diapirism on Triton: A record of crustal layering and instability. Geology 21, 299-302.

Schmidt, B. E., Blankenship, D. D., Patterson, G. W., Schenk, P. M., 2011. Active formation of 'chaos terrain' over shallow subsurface water on Europa. Nature 479, 502-505.

Schott, B., Schmeling, H., 1998. Delamination and detachment of a lithospheric root. Tectonophysics 296, 225-247.

Schott, B., Yuen, D. A., Schmeling, H., 2000. The significance of shear heating in continental delamination. Phys. Earth Planet. Inter. 118, 273-290.

Schubert, S., Anderson, J. D., Travis, B. J., Palguta, J., 2007. Enceladus: Present internal structure and differentiation by early and long-term radiogenic heating. Icarus 188, 345-355.

Segatz, M., Spohn, T., Ross, M. N., Schubert, G., 1988. Tidal dissipation, surface heat flow, and figure of viscoelastic models of Io. Icarus 75, 187-206.

Sekine, Y., et al., 2014. experimental evidence for high-temperature water-rock interactions in a chondritic core of Enceladus. Lunar and Planetary Science Conference, 1714.

Selsis, et al., 2007. Habitable planets around the star Gliese 581? Astronomy. Astrophys. 476, 1373-1378.

Shapiro, R., Schulze-Makuch, D., 2009. The Search for Alien Life in Our Solar System: Strategies and Priorities. Astrobiology 9, 335-343.

Shoji, D., Hussmann, H., Kurita, K., Sohl, F., 2013. Ice rheology and tidal heating of Enceladus. Icarus 226, 10-19.

Shoji, D., Hussmann, H., Sohl, F., Kurita, K., 2012. Possibility of oscillatory tidal heating of Enceladus. In 2012 AGU Fall Meeting Abstract P33A-1918.

Shoji, D., Hussmann, H., Sohl, F., K, Kurita., 2014. Non-steady state tidal heating of Enceladus. Icarus 235, 75-85.

Shoji, D., Kurita, K., 2014 a. Thermal-orbital coupled tidal heating and habitability of Martian-sized extrasolar planets around M stars. Astrophys. J. 789:3.

Shoji, D., Kurita, K., 2014 b. Compositional diapirism as the origin of the low albedo terrain and vaporization at mid-latitude on Ceres. J. Geophys. Res. 119.

Shoji, D., Kurita, K., 2015. Delamination in super-Earths extrapolated from the Earth model. Planet. Space Sci. in press.

Showman, A. P., Han, L., 2004. Numerical simulations of convection in Europa's ice shell: Implications for surface features. J. Geophys. Res. 109, E1.

Showman, A. P., Han, L., 2005. Effects of plasticity on convection in an ice shell: Implications for Europa. Icarus 177, 425-437.

Showman, A. P., Han, L., Hubbard, W. B., 2013. The effect of an asymmetric core on convection in Enceladus' ice shell: Implications for south polar tectonics and heat flux. Geophys. Res. Lett. 40, 5610-5614.

Smrekar, S. E., Stofan, E. R., 1997. Corona formation and heat loss on Venus by coupled upwelling and delamination. Science, 277, 1289-1294.

Soderblom, L. A., et al., 1990. Triton's geyser-like plumes: Discovery and basic characterization. Science 250, 410-415.

Solomatov, V. S., 1995. Scaling of temperature - and stress - dependent viscosity convection. Phys. Fluids 7, 266-274.

Solomatov, V. S., Moresi, L. -N., 2000. Scaling of time-dependent stagnant lid convection: Application to small-scale convection on Earth and other terrestrial planets. J. Geophys. Res. 105, 21795-21817.

Sotin, C., et al., 2005. Release of volatiles from a possible cryovolcano from near-infrared imaging of Titan. Nature 435, 786-789.

Spencer, J. R., Howett, C. J., Verbiscer, A., Hurford, T. A., Segura, M., Spencer, D. C., 2013. Enceladus Heat Flow from High Spatial Resolution Thermal Emission Observations. EPSC Abstracts, vol. 8, EPSC2013-840-1.

Spencer, J., Barr, A., Esposito, L., Helfenstein, P., Ingersoll, A., Jaumann, R., McKay, C., Nimmo, F., Waite, J., 2009. Enceladus: An active cryovolcanic satellite. In: Dougherty, M. K., Esposito, L. W., Krimigis, S. M. (Eds.), Saturn from Cassini-Huygens, Springer, New York, pp. 683-724.

Spencer, J. R., Nimmo, F., 2013. Enceladus: An active ice world in the Saturn system. Annual Review of Earth and Planetary Sciences 41, 693-717.

Spencer, J., Pearl, J., Segura, M., Flasar, F., Mamoutkine, A., Romani, P., Buratti, B.,

Hendrix, A., Spilker, L., Lopes, R., 2006. Cassini encounters Enceladus: Background and the discovery of a south polar hot spot. Science 311, 1401-1405.

Stamenković, V., Breuer, D., 2014. The tectonic model of rocky planets: Part 1- Driving factors, Models & parameters. Icarus 234, 174-193.

Stamenković, V., Breuer, D., Spohn, T., 2011. Thermal and transport properties of mantle rock at high pressure: Applications to super-Earths. Icarus 216, 572-569.

Stegman, D. R., Freeman, J., May, D. A., 2009. Origin of ice diapirism, true polar wander, subsurface ocean, and tiger stripes of Enceladus driven by compositional convection. Icarus, 202, 669-680.

Stein, C., Lowman, J. P., Hansen, U., 2013. The influence of mantle internal heating on lithospheric mobility: Implications for super-Earths. Earth Planet. Sci. Lett. 361, 448-459.

Tackley, P. J., Ammann, M., Brodholt, J. P., Dobson, D. P., Valencia, D., 2013. Mantle dynamics in super-Earths: Post-perovskite rheology and self-regulation of viscosity. Icarus 225, 50-61.

Takahashi, E., 1990. Speculations on the Archaean mantle: missing link between komatiite and depleted garnet peridotite. J. Geophys. Res. 95, 15941-15954.

Takeuchi, H., Saito, M., 1972. Seismic surfaces waves. In: Bolt, B.A. (Ed.), Methods in Computational Physics, vol. 1. Academic Press, New York, pp. 217-295.

Thomas, P. C., Parker, J. Wm., McFadden, L. A., Russell, C. T., Stern, S. A., Sykes, M. V., Young, E. F., 2005. Differentiation of the asteroid Ceres as revealed by its shape. Nature 437, 224-226.

Tobie, G., Grasset, O., Lunine, J. I., Mocquet, A., Sotin, C., 2005 a. Titan's internal structure inferred from a coupled thermal-orbital model. Icarus 175, 496-502.

Tobie, G., Mocquet, A., Sotin, C., 2005 b. Tidal dissipation within large icy satellites: Applications to Europa and Titan. Icarus 177, 534-549.

Tobie, G., Čadek, O., Sotin, C., 2008. Solid tidal friction above a liquid water reservoir as the origin of the south pole hotspot on Enceladus. Icarus 196, 642-652.

Torquato, S., Truskett, T. M., Debenedetti, P. G., 2000. Is Random Close Packing of Spheres Well Defined?. Phys. Rev. Lett. 84, 2464-2467.

Tyler, R. H., 2009. Ocean tides heat Enceladus. Geophys. Res. Lett. 36, L15205.

Tyler, R., 2009. Tidal dynamical considerations constrain the state of an ocean on Enceladus. Icarus 211, 770-779.

Tyler, R., 2014. Comparative estimates of the heat generated by ocean tides on icy satellites in the outer Solar System. Icarus 243-358-385.

Valencia, D., O'Connell, R. J., Sasselov, D., 2006. Internal structure of massive terrestrial planets. Icarus 181, 545-554.

Valencia, D., O'Connell, R.J., Sasselov, D.D., 2007. Inevitability of plate tectonics on super-Earths. Astrophys. J. 670, L45-L48.

Valera, J. L., Negredo, A. M., Jiménez-Munt, I., 2011. Deep and near-surface consequences of root removal by asymmetric continental delamination. Tectonophysics 502, 257-265.

Vance, S., Harnmeijer, J., Kimura, J., Hussmann, H., Demartin, B., Brown, J. M., Hydrothermal system in small ocean planets. Astrobiology 7, 987-1005.

van Heck, H. J., Tackley, P. J., 2011. Plate tectonics on super-Earths: Equally or more likely than on Earth. Earth Planet. Sci. Lett. 310, 252-261.

Wagner, F. W., Sohl, F., Hussmann, H., Grott, M., Rauer H., 2011. Interior structure models of solid exoplanets using material laws in the infinite pressure limit. Icarus 214, 366-376.

Wagner, F. W., Tosi, N., Sohl, F., Rauer, H., Spohn, T., 2012. Rocky super-Earth interiors Structure and internal dynamics of CoRoT-7b and Kepler-10b. Astron. Astrophys, A103.

Waite Jr., J.H.and 15 Colleagues, 2009. Liquid water on Enceladus from observations of ammonia and 40Ar in the plume. Nature 460, 487-490.

Yang, J., Cowan, N. B., Abbot, D. S., 2013. Stabilizing Cloud Feedback Dramatically Expands the Habitable Zone of Tidally Locked Planets. Astrophys. J. 771, L45.

Zhang, K., Nimmo, F., 2009. Recent orbital evolution and the internal structure of Enceladus and Dione. Icarus 204, 597-609.

Zolotov, N. Y., 2009. On the composition and differentiation of Ceres. Icarus 204, 183-193.